Flow field analyses within a Regenerative Flow Pump: The Power of Periodic Dynamics

Zur Erlangung des akademischen Grades

Doktor der Ingenieurwissenschaften

der Fakultät für Maschinenbau

Karlsruher Institut für Technologie (KIT)

genehmigte

Dissertation

von

Dipl.-Ing. Philipp Mattern

Tag der mündlichen Prüfung: 01.04.2016

Hauptreferent: Prof. Dr.-Ing. Martin Gabi

Korreferent: Prof. Dr.-Ing. Martin Böhle

Hiermit erkläre ich, dass ich die vorliegende Arbeit unter der Betreuung von Prof. Dr.-Ing. M. Gabi und Dr.-Ing. J. Kriegseis selbstständig angefertigt und keine anderen als die angegebenen Quellen und Hilfsmittel benutzt, sowie die wörtlich und inhaltlich übernommenen Stellen als solche kenntlich gemacht und die Satzung des KIT zur Sicherung guter wissenschaftlicher Praxis in der jeweils gültigen Fassung beachtet habe.

September 13, 2016, Philipp Mattern

Abstract

The present work is a summary of the experimental results of the DFG Project “Numerical and Experimental Investigations of the instationary flow phenomena in a Side Channel Pump” under grant No. 585385; Reference: GA 718/5-1. Its purpose is to serve as data base for numerical validation, as well as experimental reference. In addition it proposes a new way of analyzing relative flow fields of fluid machinery by making use of a triple decomposition of arbitrary flow information.

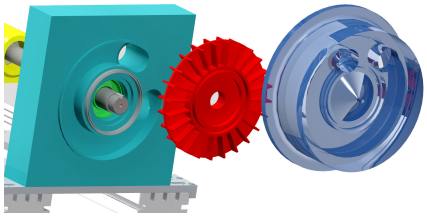

(a) CAD draft

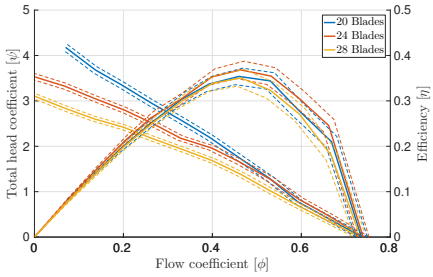

(b) Characteristic Curves

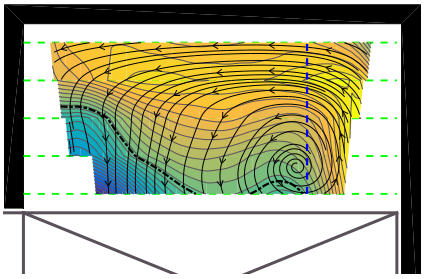

(c) Exemplary radial flow field

The study covers the design and integration of a special purpose-built side channel pump (see (a)), which is also referred to as regenerative flow pump (RFP), into a specific test rig. Common integral operational data (such as: torque, pressure, etc.) were carried out to determine the key figures of the machine. The dimensionless characteristic curves (total head / efficiency coefficient vs. flow coefficient) were identified thoroughly for three impellers with different numbers of blades within the same casing (see (b)). The analysis covers a full uncertainty, as well as error propagation estimation to ensure significance and reproducibility of the data. An extensive Time Resolved Stereo Particle Image Velocimetry (TR-SPIV) measurement campaign was realized to examine the flow development within the side channel of the machine. It includes comprehensive analyses of all three velocity components of the flow fields for six different operating points (OPs) along the characteristic curve for a plane $2mm$ above the impeller (2D-3C). Flow field information was simultaneously obtained within the developed region of the flow, covering 20% of the total working space. In addition, to further illustrate the complete development of the flow, a total of five planes along the axial extend of the side channel are explained exemplary for a single OP. Finally, they are combined using phase angle information to enable a complete 3-dimensional 3-component (3D-3C) evaluation of the flow distribution (see (c)). Results are presented starting with a rather common time-averaging approach to understand general flow field development. Afterwards the discussion is taken a step further by using phase-averaging to uncover first dynamics within the flow field. Ultimately, the concept of triple decomposed flow field information is used and proposed as a new approach to understand relative motions induced by the impeller of fluid machinery in form of ”Frozen periodic dynamics”.

Kurzfassung

Die vorliegende Arbeit ist eine Zusammenfassung der im Rahmen des DFG Projektes "Numerische und experimentelle Untersuchungen der instationären Strömungsphänomene in einer Seitenkanalmaschine" (AOBJ: 585385; GZ: GA 718/5-1) enstandenen experimentellen Ergebnisse. Weiterhin wird ein neuer Ansatz zum besseren Verständnis der relativen Laufradströmung in Strömungsmaschinen unter Zuhilfenahme der "Triple Decomposition" aufgezeigt.

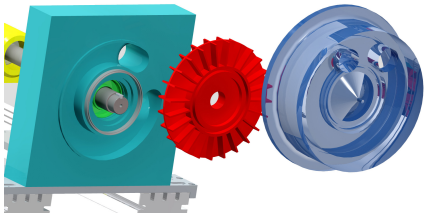

(a) Explosionszeichnung

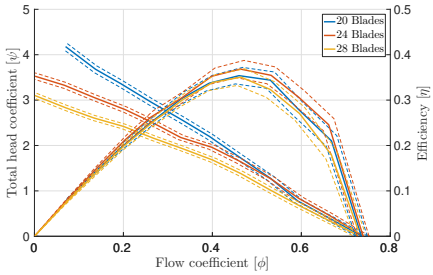

(b) Kennlinien

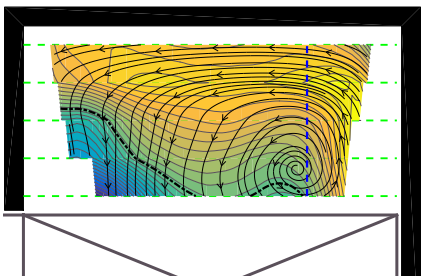

(c) Radiales Geschwindigkeitsfeld

Die Arbeit erläutert die realisierte Maschine (siehe (a)), sowie den kompletten zugehörigen Versuchsstand. Die Ermittlung der beiden wichtigsten Kennlinien (Druckzahl / Wirkungsgrad über Lieferzahl) für drei verschiedene Laufräder mit unterschiedlicher Schaufelzahl wird diskutiert(siehe (b)). Dies geschieht besonders in Hinsicht auf Messgenauigkeit und Fehlerfortpflanzung um Reproduzierbarkeit zu gewährleisten. Weiterhin wird die umfangreiche zeitaufgelöste Stereo Particle Image Velocimetry (TR-SPIV) Messkampagne im Seitenkanal der Maschine erörtert. Dies beinhaltet vor allem die Analyse der Geschwindigkeitsfelder aller drei Komponenten in einer Ebene $2mm$ über dem Laufrad für 6 verschiedene Betriebspunkte entlang der Kennlinie (2D-3C). Die Feldmessungen wurden im Bereich der entwickelten Strömung durchgeführt und erfassen 20 % des gesamten Arbeitsbereichs der Maschine. Um die weitere Entwicklung des Strömungsfeldes zu beschreiben, wurden entlang der axialen Erstreckung des Seitenkanals fünf Messebenen für einen Betriebspunkt erfasst. Diese wurden anschließend mit Hilfe simultan erfasster Drehwinkelpositionen zu einem 3-dimensionalen Geschwindigkeitsfeld mit allen drei Raumkomponenten (3D-3C) zusammengesetzt (siehe (c)). Die Beschreibung der Strömung wird von zeitgemittelten bis hin zu phasengemittelten Ergebnissen entwickelt. Abschließend wird erläutert wie mit Hilfe der "Triple Decomposition" von Geschwindigkeitsinformationen die durch das Laufrad hervorgerufene Relativbewegung der Strömung verdeutlicht werden kann. Es wird gezeigt, wie hierdurch die Ursache-Wirkungs-Beziehung zwischen Laufrad und Strömung in Strömungsmaschinen durch diese "Frozen periodic dynamics" Darstellung besser verstanden werden kann.

Contents

Abstract **i**

1 Introduction **2**

2 Theoretical Fundamentals **4**

2.1 Basics 4

2.2 Past Contributions 6

2.3 Working principle 7

3 Experiment and Methods **12**

3.1 Hydraulic System 12

3.1.1 Design of the generic RFP 12

3.1.2 Test Rig and Auxiliary Systems 17

3.2 PIV: Experimental Procedure 19

3.2.1 Setup 19

3.2.2 Postprocessing 21

3.3 Integral Operational Data Measurement 24

4 Data Validation **26**

4.1 Integral Values 26

4.2 Measurement system coupling 31

5 Results: Integral operational data **34**

5.1 Performance Characteristics 34

5.1.1 Total head coefficient Ψ and efficiency η 35

5.1.2 Impeller comparison 37

6 Results: PIV - Time averaged $\overline{\text{TA}}$ **38**

6.1 Mean Flow Fields $\overline{c_i}(\theta, r, z)$ 39

6.2 Radial Profiles 42

6.3 Circumferential Profiles 44

6.4 Standard deviation over magnitude σ/μ 45

6.5 Statistical significance 46

6.6 Plane-to-plane comparison of the mean flow fields 47

7 Results: PIV - Phase average $\langle$PA$\rangle$ **51**

7.1 Statistical significance 51

7.2 Phase Averaged Flow Fields $\langle c_i \rangle(\theta, r, z, pa)$ 52

7.3 Radial Profiles 55

7.4 Circumferential Profiles 56

7.5 Plane-to-plane comparison 57

8 Results: PIV - Combined Approach: Periodic Dynamic $\widetilde{\text{PD}}$ **60**

8.1 Periodic Dynamic Flow Fields $\widetilde{c}_i(\theta, r, z, t_{pa})$ 61

8.2 Radial Profiles 64

8.3 Circumferential Velocity Profiles 65

8.4 Plane-to-plane comparison 66

8.5 Frozen Periodic Dynamic Flow Field Interpretation 68

9 Concluding Remarks **70**

Nomenclature **78**

List of Figures **82**

List of Tables **85**

Chapter 1

Introduction

The field of fluid machinery is one of the oldest examples for mankinds efforts to convert energy from fluids to shaft power or vice versa. The first documented utilization goes back to ancient roman and greek times, where it was used for instance in form of water wheels as the major mechanical component in the vitally important irrigation systems ([1]). Since then and throughout time, fluid machinery played a leading role in the development of civilization. Nowadays, with a lot of efforts strongly pointing towards regenerative energy and sustainability, fluid machinery as the leading technology in generating and consuming electrical energy is in focus more than ever. Applications are numerous: Be that huge wind parks in non urban areas, enormous dams with Gigawatts of generated power, or the innumerable every day life applications and appliance, like fans and pumps in cars, buildings and nearly in every slightly complex machine.

As pumps are the single largest user of electricity in the European union, the urge for a higher efficiency of fluid machinery becomes apparent in the European Union's Ecodesign Directive (Directive 2009/125/EC) [2] as a framework for ecodesign requirements for energy-related products. Covering a wide range of product groups in various fields from consumer goods to industrial products, most of them are somewhat connected to fluid machinery. The directive focuses on reducing greenhouse gas emission at low cost by reducing the energy demand of various systems. Regarding fluid machinery, this is realized by setting a reference value for the minimum efficiency of a machine, which has to be met by the manufacturer. Advanced optimization and design strategies are therefore of utmost importance to meet those requirements.

In general, fluid machinery covers a wide range of combinations of pressure head versus volume flow. One specific machine, the regenerative flow pump (RFP), is used for generating high pressure heads at a small flow rate due to their low specific speed. A benefit is their small and simple construct, in addition with their self priming ability and their capability to handle multiphase flow. However, their efficiency is relatively low compared to the more common machines of the radial and axial type (The highest ever reported efficiency of 50 % was given by Crewdson [3]). Consequently, it is absolutely necessary to fully understand the basic working principle of the machine, which is described by the so called "circulation theory", based on the Euler equation for fluid machinery. However, the application of the theory in a detailed design process needs empirical knowledge and experience. Numerical methods support this process, nonetheless for validation detailed experimental data is necessary. This demand is confirmed by multiple authors:

In his work, Quail et al. [4] stated that there is "limited published data and insufficient design guiding criteria to allow more intuitive industrial selection of this pump type". This statement was supported by various others as well: Meakhail and Park [5] remark that "Regenerative flow pumps and compressors have found many applications in industry; however they are the most neglected turbomachines in terms of research. The number of publications existing in the literature is comparatively less than papers dealing with centrifugal and axial turbomachines." In the opinion of Engeda [6], "it is strongly believed that quite a substantial additional pressure and gain in efficiency can be obtained from a good understanding of the exact flow mechanism and associated losses and design changes to minimize the losses." This need for a deeper understanding of the flow was furthermore demanded. Quail et al. [4] concluded, that substantial efficiency and performance improvement would be attained with a better understanding of the flow field in the regenerative pump. In particular, Quail et al. [4] referred to the work of numerous authors ([6–10]). Recently, Böhle and Müller [11] stated, that "the composition of a side channel pump is simple, but the flow inside this machine is very complex and all details have not been understood until now". A specific commonality is the referring to the experiments: Hollenberg and Potter [12] said, that to understand RFP, "the most fruitful approach is therefore from overall performance data on specific units and corresponding flow visualization studies." Quail et al. [13] sums it up : "There is a need for significant developments in instrumentation technology and novel approaches which enable detailed data to be acquired over large regions at higher accuracy, (particularly for flow in the current study), but at a reasonable cost."

To overcome the present shortcomings and to contribute detailed data over large regions, the comprehensive DFG Project "Numerical and Experimental Investigations of the instationary flow phenomena in a Side Channel Pump" under grant No. 585385; Reference: GA 718/5-1 was launched. It is a bilateral project between the Institute of Fluid Mechanics and Fluid Machinery (SAM) of the University of Kaiserslautern and the Institute of Fluid Machinery (FSM) of the Karlsruhe Institute of Technology (KIT).

The present work focuses on the experimental part of the project by using one of the most advanced non-intrusive optical field measurement method to study a RFP within a common pump test rig, both specifically designed for the purpose. The High Speed Stereo Particle Image Velocimetry (HS-SPIV) System at hand allows to examine the unsteady internal flow within the side channel of the RFP by measuring all three velocity components simultaneously for a wide image section completely time resolved at a frequency of 2000 Hz. In addition, more common measurement categories, such as torque, volume flow and pressure are recorded in parallel.

The overall goal of this thesis is to fulfill the requested deeper understanding of the flow within the machine by providing a comprehensive insight into the flow mechanism behind the interaction between impeller and side channel. Focus lies on revealing flow fields within the side channel in a detailed way that has not been documented up until the present day. Ultimately, with the attainable measurement precision of the PIV System at hand, the data being provided shall serve as reference for CFD Calculations as demanded by the multiple authors mentioned above. In parallel, the PIV measurements are supported by common integral value measurement to provide the overall performance data of the specific purpose-built unit.

Chapter 2

Theoretical Fundamentals

As already stated in the introduction, there is an ongoing demand on more comprehensive data on and a deeper understanding of regenerative flow pumps as research in this field was only limited since the first mentioning of this kind of machine. Although recent publications about RFP (and their compressing equivalent, the regenerative flow compressor (RFC)) are not comparable in numbers to the ones for the more common centrifugal fluid machines, research on this kind of machine is still an ongoing challenge. However, all of these valuable contributions even nowadays rely on fundamentals made in the previous century which are nevertheless still up to date. Therefore this chapter aims to explain the theoretical fundamentals on basis of past contributions.

2.1 Basics

An elaboration in which they summarize and illustrate the "Current Status, Design and Performance Trends for the Regenerative Flow Compressors and Pumps" was made by Raheel and Engeda [10]. It serves as a basis for the following "Basics" section to give an introduction to RFP/RFC.

Nomenclature of RFP is versatile in literature and sometimes confusing. They are also known with other names such as (and most commonly used):

- Peripheral pump (if there is also a radial extend of the side channel)
- Side channel pump (the literal translation of the German name for the machine: "Seitenkanalpumpe")
- Turbine pump (Referring to the multiple passes of the fluid through the impeller)
- Drag pump (referring to the interaction between side channel and impeller according to the "Turbulence Theory")
- Traction pump (early publications or in combination with automotive)
- Vortex pump (due to the vortex depending working principle)

With the ability to generate a high head at low flow rates due to a very low specific speed, they share characteristics of positive displacement machines (power directly proportional to head, with maximum power required at shutoff, and a steep head-capacity curve (Quail et al. [13])), while still being associated to kinetic (or more precise: centrifugal) pumps. In addition, as they are "quasi multistage" (because of the multiple interactions between impeller and side channel), they offer much higher heads compared to the more common turbomachines with the same tip speed, while still being a single stage. Other benefits are their small and simple construct (low cost), their self priming ability and their capability to handle multiphase flow. In addition, RFPs are less vulnerable to cavitation, as occurring of such does not lead directly to mechanical failure (Muller [14]). Due to their low pressure gradient, they require lower net positive suction head (NPSH) than centrifugal pumps as well. A comparison of the differences between regenerative and centrifugal pumps adapted from Raheel and Engeda [10] is given in Table 2.1:

Regenerative	**Centrifugal**
Radial and toroidal flow	radial flow
Simple vanes	Complex vanes and volutes
More compact	Larger in size
Better efficiency at low specific speeds	Better efficiency at higher specific speeds
No surge problems / Stable operating range	Surge limit
Closer tolerances for clearance	Higher tolerances

Table 2.1: Comparison of regenerative and centrifugal pumps (adapted from [10]).

RFP/RFC are used in a wide field of operation. Despite their low efficiency, for special cases, their beneficial characteristic is unmatched by other types. The unique combination of robustness, small size and high pressure head makes RFPs especially (but not exclusively) interesting in the following fields:

- chemical, petroleum and nuclear industries
- automotive and aerospace fuel pumping
- booster systems
- water supply
- agriculture industry
- shipping and mining
- foodstuff industry
- regulation of lubrication and filtering

2.2 Past Contributions

An extensive "Overview of the theories to clarify the flow within side channel machines" was given by Grabow [15]. The present section summarizes his work and is extended by recent works.

The RFP originally appeared in literature in the beginning of the 20th century where it was used in the field of urban water supply. First studies on RFP were made in Germany by Ritter [16] and Schmiedchen [17]. They studied empirically the influence of geometric parameters on the performance curve. Based on their work, Engels [18] developed a one-dimensional model to predict specific characteristics, depending on the geometry. However, a drawback was that it relied on experimentally defined coefficients. Nowadays, there are two main theories present.

Turbulence Theory

One is the so called "turbulence theory" (also known as "mixing theory" or "Shear Stress Theory"), which was introduced by Iversen [19]. In his model, the exchange of the impeller momentum is due to turbulent shear stresses. Furthermore, fluid exchange between impeller and side channel is due to a "macroscopic mixing process". The model considers the impeller as a linear motion of a rough surface, dragging the fluid along the side channel due to shear stresses. He states that the shear forces are only due to the gradient between the mean impeller velocity and the (lower) mean side channel velocity. Weinig [20] supported the idea of turbulent shear stresses but stated that a fluid exchange between impeller and side channel takes place. In his model, the exchange was caused by vortices at the blade tips, forcing fluid from the side channel back into the vanes of the impeller. Pfleiderer [21] also supposed a circulation flow, but figured it to be constant for all points of operation. This stood in conflict with the research of Engels [18] who already showed that the circulation flow was not constant along the head-capacity curve. However, all authors neglected the circular flow due to centrifugal forces, which according to Senoo [22, 23] has to be taken into account. He stated, that the fluid is forced into the side channel due to centrifugal forces and transfers the impeller torque through momentum exchange to the fluid. Although he recognizes this circular flow as an important factor for the pressure rise of the machine, he puts the working principle down to the shear stresses as well. To sum up the theory in one sentence (which also explains its different names): Torque is transferred indirectly via *shear stresses*, due to the *turbulent mixing* process of the (primary) "side channel flow" with the "circulation flow".

Circulation Theory

A more direct approach of momentum exchange was already made by Engels [18], who stated that the combination of the primary side channel flow and the circulation flow leads to a rather helical flow interacting between side channel and impeller. Bartels [24] and Lazo and Hopkins [25] and Lutz [26] were able to uncover this helix-shaped development of the flow by various visualization techniques. This led to a further developed model by Wilson et al. [7], the so called "circulation theory" (also known as "Momentum exchange theory", "liquid filament" or "Stream line theory"). Impeller momentum is transferred onto the fluid particles traveling along a spiral path through the machine due to the centrifugal forces acting on them. Within the side channel, the circumferential velocity component reduces, transforming the momentum into

pressure head. The theory was later on refined and adapted to special use by multiple authors ([27–30]).

Summary

A review of the theories was made by Senoo [31] who concluded that both theories are compatible. Grabow [15] gave a detailed overview and discussion of both theories as well, however stating that although the circulation theory neglects drag and shear stress effects, it is widely accepted and gives better results for performance predictions as well as the general geometric configuration of a RFP. It has to be mentioned, that both sources had not yet access to CFD-results, nor modern flow field visualization techniques. Nowadays, with modern techniques being available, the momentum theory is regarded as the more flexible and precise one. Therefore recent approaches focused on improving the momentum theory([5, 9, 32]).

In the field of industrial feasibility, current studies have been made on the performance of RFP in industrial use (Kang et al. [33]), as well as general design considerations for industrial application ([6, 34–36]). Böhle and Müller [11] contributed studies regarding flow analysis on basis of analytic models and CFD. Extensive design studies based on numerical models, partial supported by measurements were carried out by Quail et al. [4, 13] and Quail et al. [37, 38]. Newest contributions to the field of RFP/RFC examine again the influence of blade properties to the characteristic of the machine ([39, 40]).

As a side note it shall be mentioned, that in the German-speaking areas especially the work of Grabow and Surek advanced the research on RFP/RFC. Cross references to various publications of both authors can be found in Grabow [15] and Surek [41]. Besides their contribution to the general theories, both authors had a focus on different machines. Grabow did a lot of research on peripheral pumps ([30, 42–50]). Surek on the other side did a lot of contributions regarding compressors. Particular (but not exclusively) regarding pressure distribution and development within the machine ([41, 51–56]). Another important work was one of his earlier studies on the mass flow through the machine: Based on experimental work he formulated the mass flow balance around the stripper showing its great influence regarding machine characteristic and performance ([57]).

2.3 Working principle

To understand the basic flow mechanism within a RFP, Figure 2.1 is introduced.

It shows in a schematic manner a single stage, single sided RFP. On the left hand side a section through the side channel and the impeller is shown to illustrate the axial structure of the machine. The top down view on the right hand side shows the annular side channel in blue, together with in- and outlet. The main flow direction is marked with a red arrow, while the impeller is rotating with ω (green arrow). The fluid enters the side channel axially from the inlet and is directly forced by the underlying impeller into the rotating direction. The fluid then is accelerated up to point where the flow is considered developed. In that phase, there is a linear pressure rise up to a point, where the influence of the outlet affects the fluid again. It decelerates and leaves the machine at the outlet. The pressure rise and therefore working principle of the machine is caused due to a circular flow, rotating between impeller and side

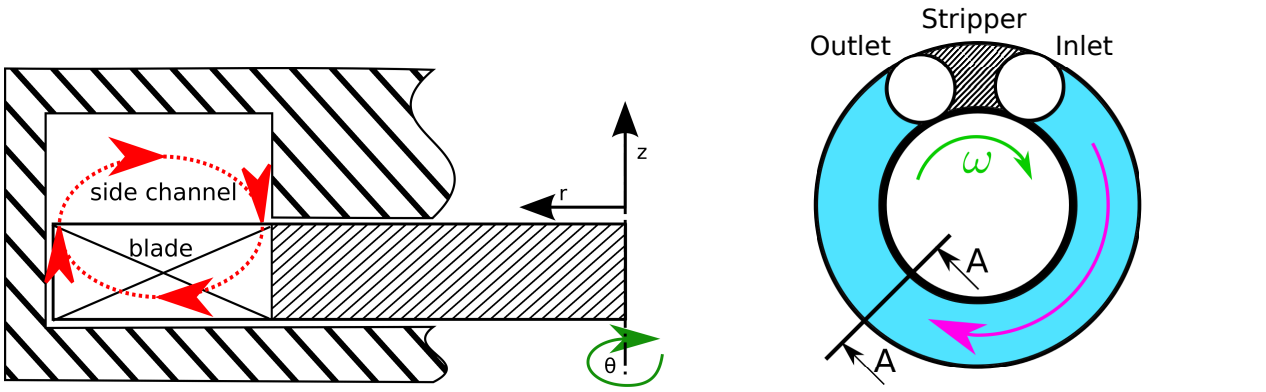

(a) Section A-A (Circulation flow in red) (b) Top down view (Magenta: primary flow)

Figure 2.1: Main flow mechanics in a RFP.

channel. Together with the main flow velocity in rotating direction, this leads to a helical flow along the circumferential extend of the side channel often described as a corkscrew flow (figuratively, a single path line can be abstracted in form of a "mechanical spring"). The number of interactions between impeller and side channel (therefore the circumferential dilatation of the "spring") is strongly depending on the operating point(OP): very few interactions in overload (OL), five to eight circulations near best efficiency point (BEP) (according to Surek [58]) and considerably more in partload (PL).

To understand the flow within fluid machinery, it is common to transfer an absolute velocity ($\vec{c}$) within a earth fixed coordinate system into an impeller fixed coordinate system. The common way to do so is a graphical approach in form of "velocity triangles" as shown with Figure 2.2.

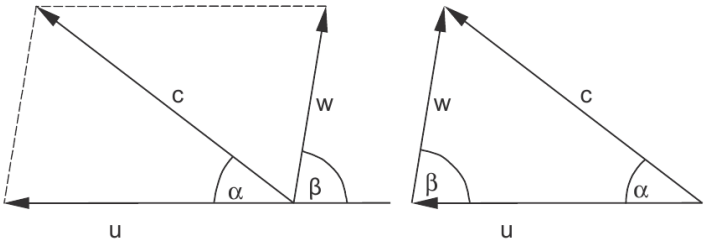

Figure 2.2: "Velocity triangles": the relation between earth fixed and impeller fixed coordinate system (according to [59]).

It shows the vectorial relation between the absolute velocity $\vec{c} = c_i = [c_u, c_r, c_{ax}]$, the local circumferential impeller velocity $\vec{u} = \omega r$, with ω being the angular velocity multiplied by the current radius r, and the relative velocity component $\vec{w} = w_i = [w_u, w_r, w_{ax}]$, together with their corresponding angles. The relation is formulated by

$$\vec{w} = \vec{c} - \vec{u}. \tag{2.1}$$

In common fluid machinery this relation in combination with various assumptions is used to formulate the energy exchange between impeller and fluid. In general this is described with "Euler's pump and turbine equation". In case of RFPs, this has to be adapted.

"Analytical Flow Model" [11]

As previously stated, the momentum theory is nowadays widely accepted. It is commonly described using a 1D model as a first approximation by formulating a momentum balance within the side channel and afterwards concluding the result onto the impeller, ultimately describing the working principle of the machine ([11, 35–37]).The following section is an adaption of the "Analytical Flow Model" section of Böhle and Müller [11], taking the present geometry into account. However, the mathematical model is identical: A small control volume is considered along the circumferential extend of the side channel. The following assumptions are made:

- The flow is steady (Stationary, circumferential velocity within the side channel)
- The fluid is incompressible with no change in density (Water)
- No leakage occurs
- Unlimited number of blades for the impeller
- All processes are adiabatic
- Flow is characterized by a tangential and circularly velocity (defining the primary and circular flow)
- Circumferential pressure gradient is independent of the radius.

A 3D view of the control volume is given with Figure 2.3.

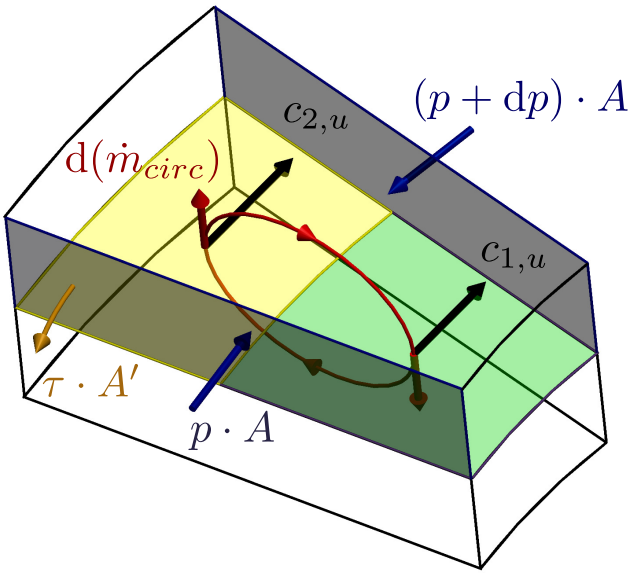

Figure 2.3: Momentum balance for a control volume along the side channel with acting forces (adapted from [11]).

The circulation mass flow $\mathrm{d}(\dot{m}_{circ})$ is drawn in red. It enters the side channel from the impeller at the outer part with a circumferential velocity component $c_{2,u}$ and leaves the side channel into the impeller bearing the circumferential velocity component $c_{1,u}$ (Due to mass conservation, the areas

of the colored exchange interfaces (yellow and green) are assumed to be equal. Therefore, velocity components $c_{1\&2,u}$ are the simplified characteristic mean circumferential velocities according to the conservation of mass between impeller and side channel). As only forces in circumferential direction can contribute to torsional momentum, these are the momentums on the circulating mass flow due to the flow velocity components $c_{1\&2,u}$ and the pressure forces orthogonal to the cross section of the side channel (Gray areas). As they are equal, the pressure rise in between them is $\mathrm{d}p \cdot A$. Flow friction is expressed by the averaged shear stresses τ, acting on A', which is the whole surface of the control volume minus $2 \cdot A$. Now the momentum balance in circumferential direction can be formulated:

$$\mathrm{d}(\dot{m}_{circ}) \cdot c_{1,u} - \mathrm{d}(\dot{m}_{circ}) \cdot c_{2,u} + \mathrm{d}p \cdot A + \tau \cdot A' = 0 \tag{2.2}$$

By neglecting the shear stresses τ, integration in circumferential direction along the side channel yields:

$$\dot{m}_{circ} \cdot (c_{2,u} - c_{1,u}) = \Delta p \cdot A \tag{2.3}$$

As side channel and impeller only interact through a single control surface, due to mass and energy conservation, this is valid for the impeller as well. Therefore the left hand side of the equation now can be interpreted as "Euler's pump and turbine equation", providing the necessary momentum for the pressure rise within the side channel (Right hand side). Reformulating this in terms of the theoretical total head leads to:

$$\Delta H_{theo} = \frac{\Delta p}{g \cdot \rho} = \frac{\dot{m}_{circ}}{g \cdot \rho \cdot A} \cdot (c_{2,u} - c_{1,u}) \tag{2.4}$$

Ultimately, this enables to predict the pressure rise of the machine only according to geometrical parameters and velocities, which can be provided by simulation or experiments.

Flow development / velocity triangles

The one-dimensional circulation theory has been proven to be sufficient for most purposes and is conform with the "Euler's pump and turbine equation" for fluid machinery. Therefore the affinity laws can be used. Being able to do so grants the advantage to easily predict performance of similar pumps once a discrete machine has been examined. It also includes kinematic similarity which enables to use velocity triangles as a mean of describing the flow through the impeller. In case of the more common machines, velocity triangles are normally drawn with respect to the impeller in a 2 dimensional plane. This is to easily visualize absolute and relative velocities to understand occurring phenomena and the interaction between impeller and flow in general as well as the interaction with non-rotating parts of the casing such as guide vanes (e.g. flow separation, shock losses, recirculation). This one-dimensional approach (streamline theory) through a single blade channel and optional guide vanes is sufficient enough, as in common machines flow passes through the impeller only once and is regarded similar for each individual blade channel. In case of RFP, with it being "quasi multistage" this is different. The side channel acts on the circular flow as a "pseudo guide vane", as it directly influences the inlet flow of a subsequent blade channel according to the out flow of the present one. An approach to use a similar way of reducing the three dimensional flow to a two dimensional plane representing the flow in case of a RFP is to combine two meridional cuts through side channel and impeller along θ at distinct radii $r_{2\&1}$. For this approach, any radial velocity component $(c, w, u)_r$ is neglected. This "unrolled" representation is shown in Figure 2.4.

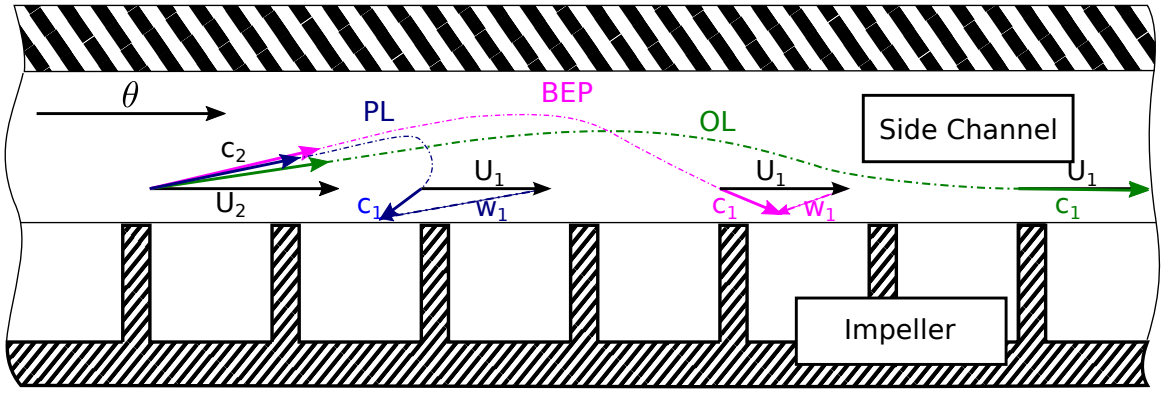

Figure 2.4: Assumed path-lines and velocity triangles for different operating points within the unrolled side channel.

It shows the assumed angular path-lines for different operating points as well as the according velocity triangles (Magnitude as well as angles are based on actual measurements, positions are exemplary chosen at different blades). Index 2 refers to a cut at a big radius (inflow into the side channel), while index 1 refers to the back flow into the impeller near the hub (Note that for common machines one refers to the flow within the blade channel. For RFP however, as shown before, formulating the momentum balance within the side channel is more convenient. Therefore the odd flow direction from 2 to 1). It is visible, that in overload mode there's nearly no interaction with the impeller, while in part load a strong interaction is suggested.

Chapter 3

Experiment and Methods

The following chapter describes the experimental setup, the instrumentation in detail as well as post-processing methods were necessary.

3.1 Hydraulic System

As the project was started from scratch, a generic RFP prototype as well as the supporting test rig had to be designed and built.

3.1.1 Design of the generic RFP

Key challenge regarding the design of the RFP was to find a compromise between measurability and industry-oriented geometrical shape: As the quality of PIV Measurements strongly depends on the optical access to the desired region of interest (therefore the optical path of the key components), focus lies on simple geometric shapes enabling few up to no refraction at all. For reasons of comparability however, the design should be as close to common existing models as possible as well as reasonably sized in general to properly install and operate the equipment. Such common approaches on efficient design of RFPs normally show complex free shaped blades, as well as three dimensional shapes of the side channel. Additionally, due to the nature of their very high pressure heads, all components of the machine are designed in a massive and reinforced way, mostly made of durable materials, such as steel or tough cast aluminum or iron. On the other hand, with PIV being an optical, non-intrusive way to measure flow fields within a machine, it is necessary to have a straight line of sight between the camera-, as well the laser system and the intended measurement plane. Inevitably, at least some components have to be made out of transparent material, which nowadays is solved by using either rather soft acrylic glass or normal, rather brittle glass. In addition, the accuracy of PIV measurements is strongly influenced by optical aberration. To reduce refraction and other disturbing optical phenomena, it is necessary to minimize curved surfaces in the optical path. These requirements stand in direct contrast to each other, as designing a RFP in a flow optimized way would lead to complex three-dimensional structures, therefore leading to distortion. This leads to the necessity of a generic geometry, with the main focus on optical accessibility, yet still fully operating as a RFP. Hands-on experience from earlier studies with the available PIV System gave guidance on optimal setup conditions.

Despite the fact, that normally a PIV System is adapted to the flow situation and not the other way round, it was decided to adapt some geometric machine parameters to the given PIV System, as precise results were of the utmost importance and experience with that very system were existent. In the following, certain machine design characteristics and the reasons for choosing them are presented. To give a general overview, Figure 3.1 shows the resulting generic design. Figure 3.2 shows the sectional view through the machine and directly a distinct difference to more common types: the nonexistent radial extension of the side channel. Therefore each flow side is independent, sealed by the impeller itself. Interaction between the flows is only possible through the small gap between the outer rim of the impeller and the inner side channel wall.

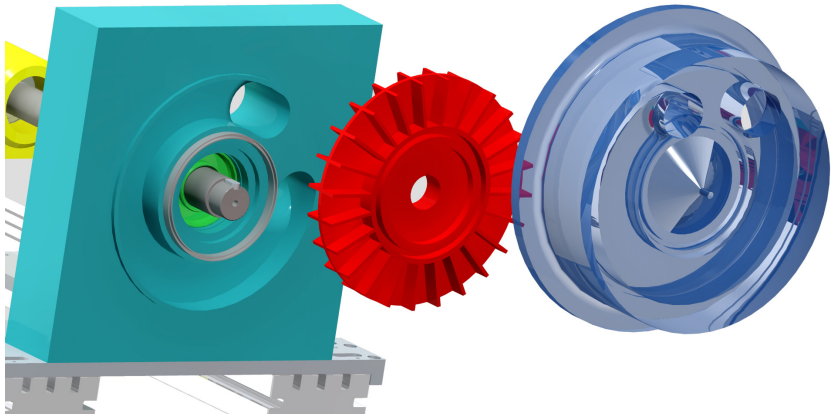

Figure 3.1: Exploded view of the RFP draft.

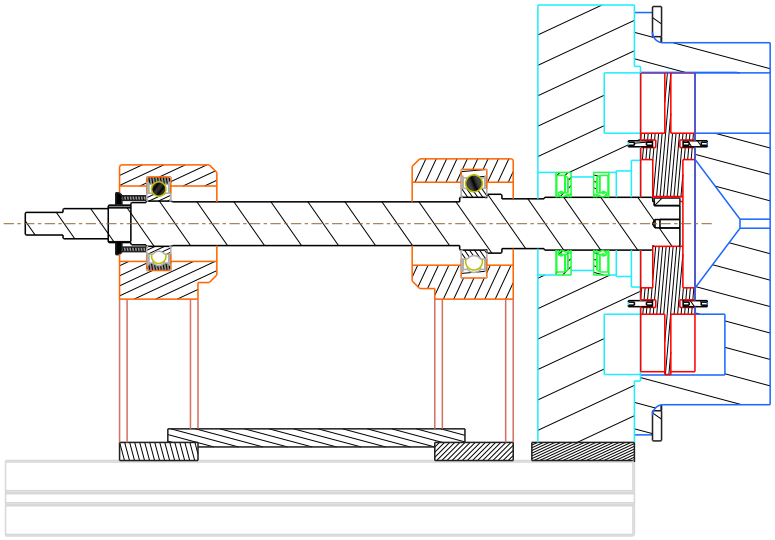

Figure 3.2: Sectional View of the RFP.

Overall Dimensions

For the available PIV System, a region of interest (ROI) with a characteristic length of $8 - 10cm$ offered best results in preliminary studies ([73]). Furthermore, to be able to observe the

development of the flow, the ROI should cover at least three complete blade channels. Since curved surfaces introduce a higher uncertainty for Stereo-PIV measurements, right angles were considered mandatory. Said requirements in addition with a design process according to Surek [41] lead to a rectangular side channel and a corresponding impeller with the geometric dimensions given in table 3.1 and general specifications with table 3.2.

Impeller Diameter	200 mm
Blade Length	40 mm
Blade Width	16 mm
Blade Thickness	3 mm
Cross-section Side Channel	20 x 40 mm
In- and Outlet Diameter	40 mm
Gaps	0.3 mm
Number of Blades	24

Table 3.1: Geometrical dimensions.

Rotational speed	500 [1/min]
Maximum volume flow (single side)	11 [m^3/h]
Maximum pressure rise (single side)	5 [m]
Outer circumferential impeller speed (U)	5.2 [m/s]

Table 3.2: General specifications.

Casing

To equalize axial forces, a symmetric double flow machine was realized. This enables the pump to hydraulically self-center the impeller. Consequently, two side channels on both sides of the impeller are required. Another elementary necessity is the ability to easily disassemble the machine. Main reason for this is the placement of the PIV Target, which has to be installed and removed before every single series of measurement. This was taken into account by separating the casing into two parts. One side channel was milled into a square block of POM (Polyoxymethylen) (Figure 3.3a) which served as basis for the machine itself (in the following referred to as "POM-side") and includes the shaft packing as well. The other side channel was milled into an acrylic hub (Figure 3.3b), referred to as "PIV-side". The hub can be easily detached in whole, granting access to the inner parts of the machine. Unavoidable, doing so requires previous draining of the test rig. The interface between the two casing parts is sealed with a circumferential packing. To align the two parts, the POM side is equipped with a circumferential tongue and the PIV hub with the corresponding circumferential groove. This enables to rotate the hub freely around the axis of rotation, granting optical access to different measurement positions along θ. Due to feasibility and cost, the material of choice regarding the necessary optical access through the

(a) POM Basis with milled side channel, shaft and circumferential labyrinth sealing.

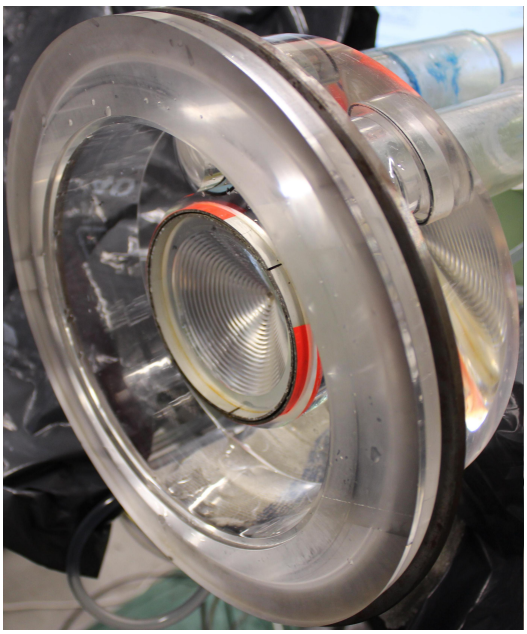

(b) Acrylic hub with labyrinth sealing visible in orange.

Figure 3.3: Basis and hub of the RFP.

hub was Plexiglas. First test showed that fixating the two parts with screw clamps was slightly deforming the hub leading to leakage, as well as rubbing between impeller and hub. This could be compensated by putting an additional steel ring on top of the hub, enabling to distribute the contact pressure between the two casing parts more equally. Both parts are also equipped with a double labyrinth sealing at the inner rim of the side channel in form of bent aluminum bands. In case of the acrylic hub, those bands are additionally pasted with a thin orange foil to minimize the blooming effect of the laser when hitting reflective surfaces. To seal the inlet from the outlet, the side channels do not span continuously along the circumference, but are rather separated by 30° at their smallest distance. This area is called a "stripper". It assures, that for the impeller with 24 blades at least one blade channel with its two associated blades separates in- and outlet all the time. To minimize losses at the transition from in- and outlet into the side channel, the sharp entry edges were rounded with a radius of $10mm$. All gaps within the machine were planned with $0.3mm$, with an assumed manufacturing tolerance of $0.05mm$. Due to constructional limitations it was not possible to align both casing parts perfectly symmetrical. The POM side was turned 53° out of position in direction of θ (as can be seen in Figure 3.3a, the splitter is turned to the right, instead of pointing directly upwards, as it is the case for the PIV side). However, it was assumed that due to the small pressure difference on both sides of the impeller, the very small gap between impeller and side channel and the huge velocity gradient to the opposite (axial) direction into the side channel, this difference can be neglected. The assembled, drained machine in total is given with Figure 3.4a. Main reason for using POM is its matt, black surface. As light scatter is an unavoidable Problem of PIV measurements, non-reflecting surfaces are of great importance to optimize the results. Preliminary studies showed smaller reflections when using POM compared to coated or painted metal. In addition, tolerances could be smaller as no further anti reflection treatment such as coating or painting

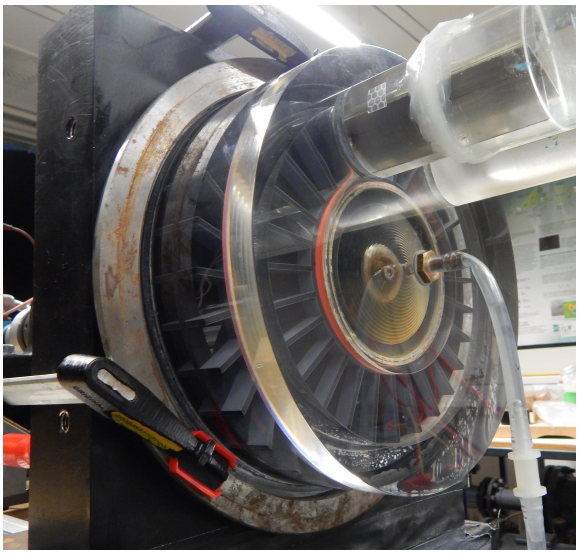

(a) Assembled RFP; drained; Cross-shaped flow straightener visible within the outlet.

(b) Impeller (24 blades) mounted on POM Basis; Circumferential blade offset visible.

Figure 3.4: Detailed assembled views of the RFP.

has to be taken into account. Downside of POM is its relatively high thermal expansion and the very low thermal conductivity compared to a standard housing material like aluminum or steel. In a first version, angular bearings for the RFP shaft were integrated into the POM casing itself. However, testing showed that this lead to temperature problems, as friction heat was unable to dissipate and bearing temperatures reached $70°C - 80°C$ easily, therefore softened the POM casing. In the final version, this was avoided by using an external adjusted tandem-O bearing arrangement outside of the machine. This external bearing prevents temperature problems completely and is also less susceptible to vibration. As a side effect the now obsolete angular bearings could be replaced by two packings, sealing the machine completely even at low rpm.

Impeller

The impeller has a double-flow design as well. Two identical blade patterns are separated by a circular disc with a thickness of $4mm$ as can be seen in Figure 3.4b. Out of geometric simplicity, as well as there are intentions to measure within the blade channel in future projects, a straight radial blade configuration was chosen. As the receiving counterpart to the labyrinth packing from the casing, a circumferential groove of $10mm$ depth and $5mm$ width is milled into the hub at a radius of $50mm$. The first impeller with 24 blades was milled from a solid POM block. Due to a mistake during calibration of the milling machine, the impeller was not completely symmetrical, but had a small rotary shift ($4mm$ or 2.3°) regarding the angular distribution of the blades on both sides of the impeller. The resulting misalignment of the blade positions on each side of the impeller can be seen in Figure 3.4b. Later on, two additional impellers with 20, as well as 28 blades were manufactured. However, as rapid prototyping (RP) methods advanced quickly, those could be 3D-printed out of "FullCure870" (photopolymer resin) from "Objet". As "FullCure870" itself is grayish, with a matt surface finish, reflections were slightly more disturbing as in case of POM, however could still be considered minor. Against previous

assumptions, there were no problems regarding structural durability or surface roughness. Both RP impellers had no misalignment of the blades.

3.1.2 Test Rig and Auxiliary Systems

To analyze the RFP by means of common integral values and to be able to adjust different operating points along the characteristic curve of the machine, the RFP was integrated into a closed-loop test rig. The corresponding hydraulic scheme is presented with Figure 3.5.

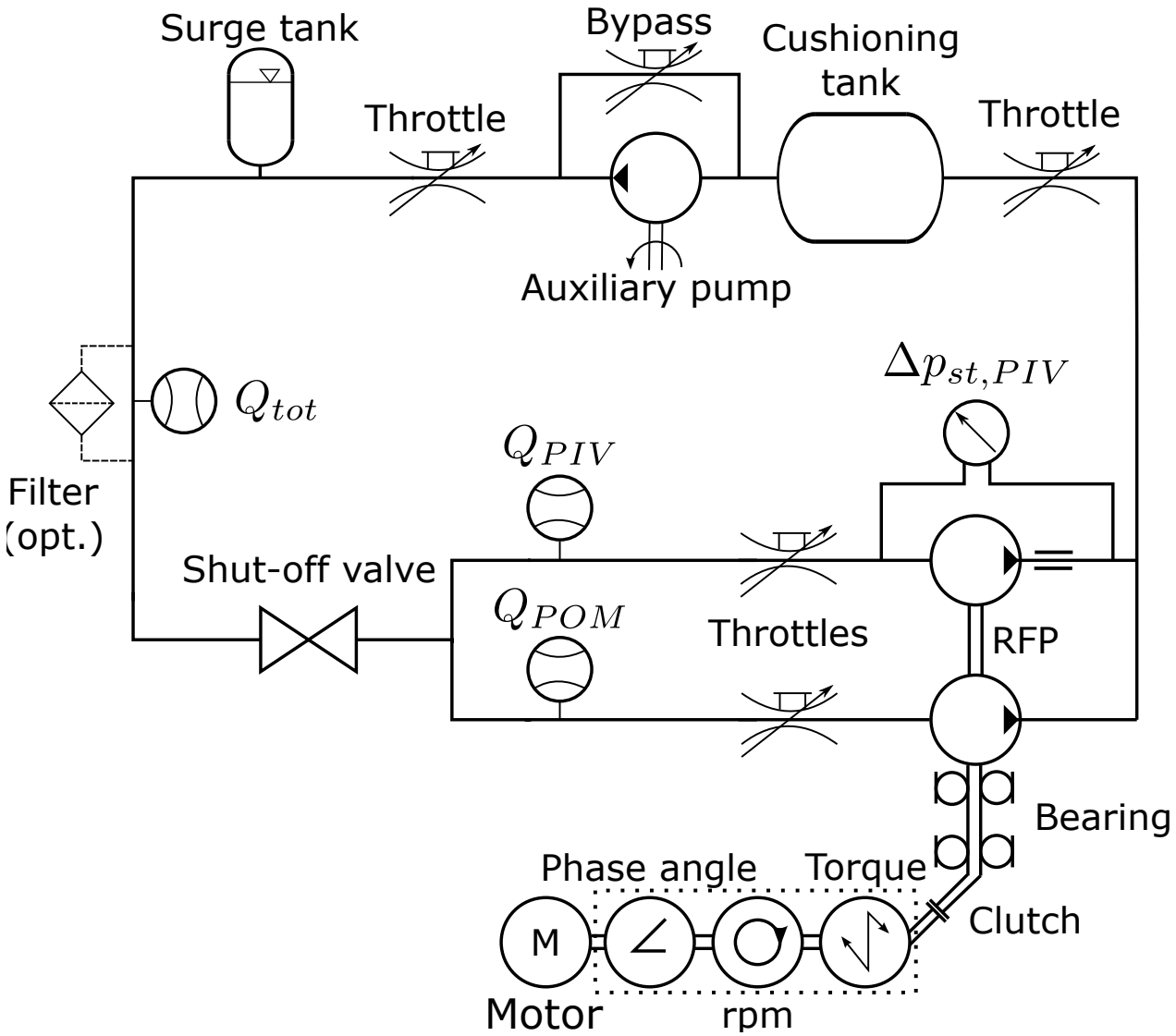

Figure 3.5: Hydraulic scheme of the test rig.

A complete loop cycle following flow direction through the test rig is given in the following starting at the RFP: A power train, consisting of a drive unit and a torque meter is mechanically connected to the RFP shaft via a safety clutch to prevent damage in case of over-operation. The drive unit is controlled via a frequency inverter. As additional information, the torque meter also measures speed and rotation angle (indicated as one unit by dotted lines). The RFP shaft is

bedded in an adjusted tandem-O bearing arrangement outside the machine. The power train in whole is mounted on a rail system with each component bedded on a separate support structure. This enables to align the shaft bit by bit to minimize friction losses within the bearings and seals as well as positioning the impeller within the casing without contact. The two flow sides of the RFP are completely separated regarding their connection to the test rig. The static pressure rise of the PIV-side is measured via wall mounted probes at the in- and outlet of the machine. To illustrate this furthermore, Figure 3.6 is introduced:

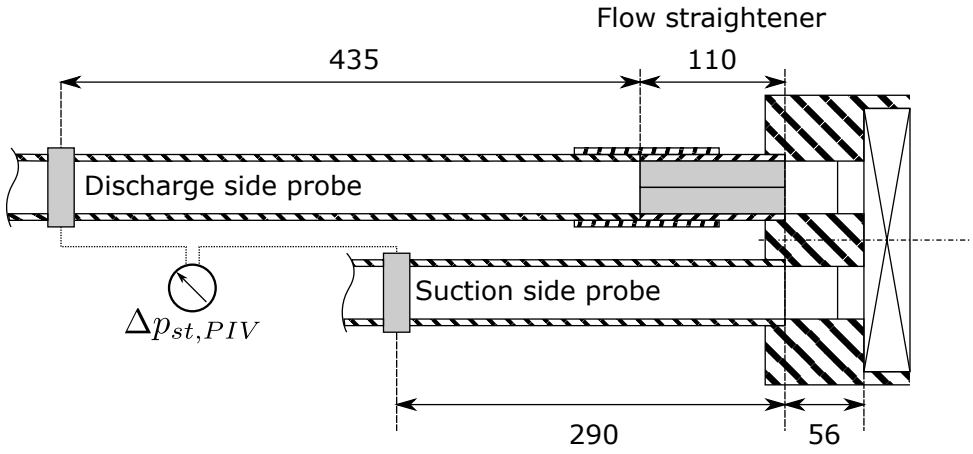

Figure 3.6: Position of the pressure probes in [mm].

Static wall pressure probes designed as a clamp with four equidistant holes to average over the circumference are installed at the marked positions. A cross-shaped flow straightener made of steel with a thickness of $1mm$ and a length of $110mm$ is insert at the discharge side to convert the circumferential component of the flow (The necessity to do so can be seen in Figure 3.7, showing the discharge side of the machine without straightener. Visualization is realized by adding a small amount of air to the flow. The strong circumferential component is clearly visible). To avoid flow disturbance, the total length of the in- as well as outlet zone on the PIV-side is $20 * D_{nom}$, realized by straight acrylic tubes. Afterwards both flows are merged. Via a throttle valve the combined flow enters a cushioning tank. Said throttle valve is used to generate pressure loss to operate the RFP in part load mode. Additionally, the throttle serves as a shut-off valve as well. Together with the second shut-off valve on the suction side of the RFP it isolates the main test rig against the RFP. This enables to drain the RFP for

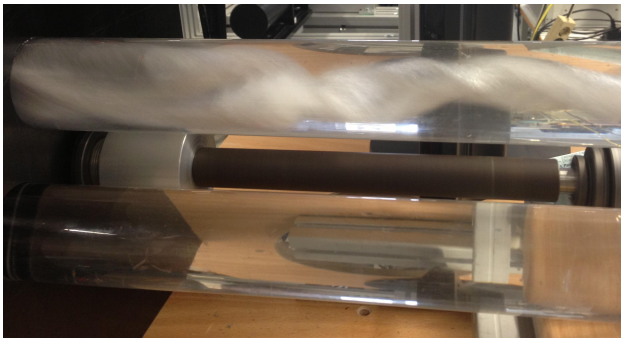

(a) Part load mode.

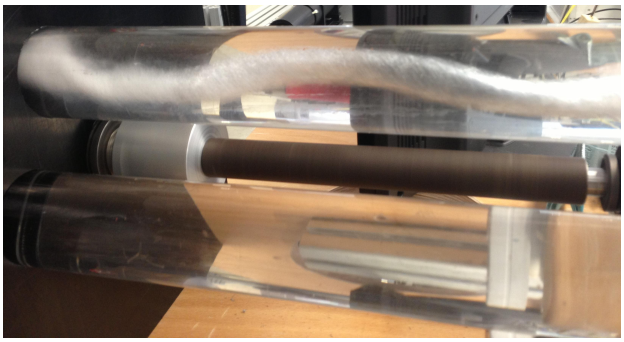

(b) Overload mode.

Figure 3.7: Discharge side swirl flow due to missing straightener, visualized by trapped air.

maintenance or calibration reasons, while the main test rig stays flooded. After the cushioning tank, an auxiliary unit, consisting of a pump with parallel bypass, a throttle valve and a surge tank is installed. This common auxiliary unit in a close loop test rig enables to operate the pump under test in every operating point along the characteristic curve. The surge tank enables to outgas the test rig, as well as to pre-pressurize the test rig in total. During experiments it was determined, that it was more beneficial to regulate pressure losses with the throttle valve before the cushioning tank instead of the throttle valve of the auxiliary unit. This was due to occurring cavitation on the RFP. To measure the total volume flow Q_{tot}, an inductive flow meter with an inlet zone of $10 * D_{Nom}$ and an outlet zone of $5 * D_{Nom}$ is installed after the surge tank. For maintenance purposes, the flow meter can be exchanged with a filter system. This is necessary to get rid of undesired foreign matter such as rust or conglomeration of seeding. During measurement however, the flow meter is installed regular. After the shut-off valve flow is separated into two lines. Although efforts had been made to construct both lines symmetrical to have identical pressure loss, first experiments showed slight differences. To overcome this, both lines are equipped with a throttle valve as well as a vortex flow meter (inlet zone: $15 * D_{Nom}$, outlet zone: $5 * D_{Nom}$). This enables to balance both flows before each measurement.

3.2 PIV: Experimental Procedure

A quite common way to measure velocity distributions is particle image velocimetry (PIV). The biggest advantage of this technique is the ability to gather simultaneous flow field information for a desired region of interest at a wide spread of measurement frequencies (depending on the used system). As this technique nowadays is quite common and widely-used in industrial as well as academic research and in order not to go beyond the scope of this work, the method itself is considered known and only the used parameters will be given (For further information, it shall be referred to the reference book for PIV applications: Raffel et al. [60]).

3.2.1 Setup

Basic PIV Setup specifications are given with Table 3.3.

Laser wavelength	527 nm
Camera resolution	1008*1024 pixel
Frame rate	4000 fps
PIV Measurement Frequency	2000 Hz
Mean seeding particle diameter	20 µm
Stereo viewing angle	65°
Light sheet area	120*55 mm
PIV Snapshots per measurement	2771

Table 3.3: PIV Setup Summary

For flow illumination, a dual oscillator/single head, diode pumped Nd:YLF laser "Darwin Duo" from "Quantronix", was used. Two high speed cameras, "Photron FASTCAM SA4", with a $1008*1024\ pixel$ resolution at $4000 fps$ (Thus leading to a PIV measurement frequency of $2000 Hz$ due to the double frame recording) and the corresponding "Photron FASTCAM Viewer" software were used for recording. The cameras were equipped with two "Canon" $EF\ 85mm\ f/1.8\ USM$ lenses each mounted on Scheimpflug tilt adapters with automated EOS Rings from "ILA GmbH". The crucial timing between the Laser and the cameras was realized using a Synchronizer from "ILA GmbH" as well. Seeding of the fluid was done using $20\mu m$ polyamide Particles. The Stereo PIV System was set up in a standard Forward/Backward scattered configuration, with an angle of 65° and a distance of $277mm$ between both cameras as shown in Figure 3.8a (Reference point for the distances is the assumed optical mean position of the lenses).

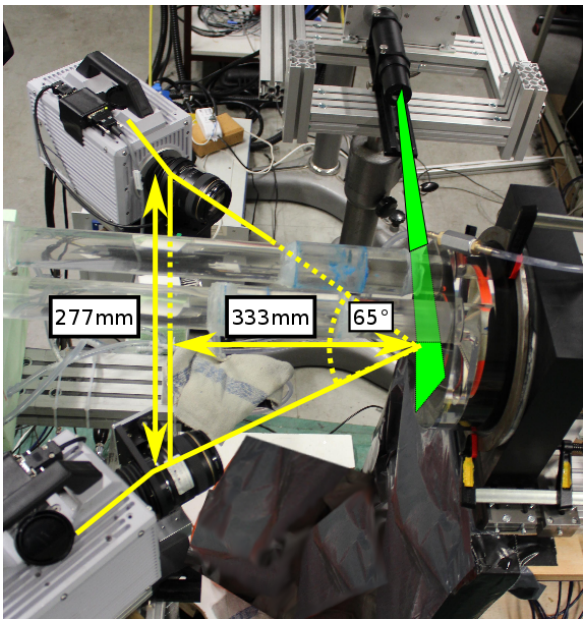

(a) Positions of the HS-SPIV Components.

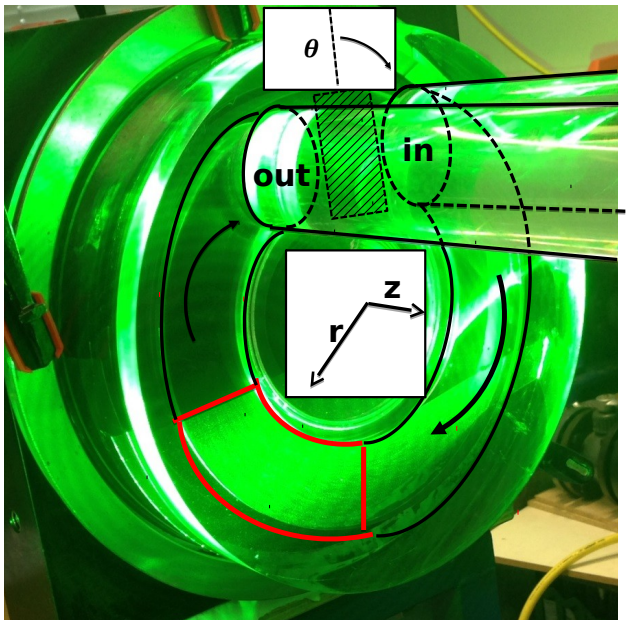

(b) Close up of the acrylic hub. PIV Measurement Area marked in red; Flow direction and coordinate system is indicated.

Figure 3.8: PIV Setup.

The light sheet spans an area of approximately $120 * 55mm$, while the distance to the camera normal is $333mm$. Scheimpflug angle is indicated but not specified, as it was adapted after every calibration. Range was in between $7° - 10°$. Figure 3.8b shows the illuminated hub during measurement. Flow direction through the machine, and the chosen coordinate system are indicated. The fluid enters the machine at the upper right corner and is circularly transported along θ through the side channel covering a total of 270° up to the outlet (This defines the main flow). z defines the axial coordinate, while r and θ are the radial and circumferential coordinates, respectively. Note that in- and outlet are separated by a stripper (hatched area), with its center being used as the origin for the θ coordinate. The rotation axis defines the origin for r, while the axial tip of the blades defines the origin for z. The light sheet of the laser enters the acrylic casing from the left and illuminates the area marked in red. Although the hub itself is indirectly illuminated due to reflections and seems to glow constantly due to the Laser double pulse repetition rate of $2000 Hz$, it was possible to minimize disturbance by means

of masking, both physically by foil and later on in the post-processing process. At its widest point, the measured area covers approximately 70°, starting from $\theta = 190°$ up to $\theta = 260°$, all with respect to the stripper. Within this regime, the flow is considered developed (see Chapter 2), as influences of both, in- and outlet should be minimal.

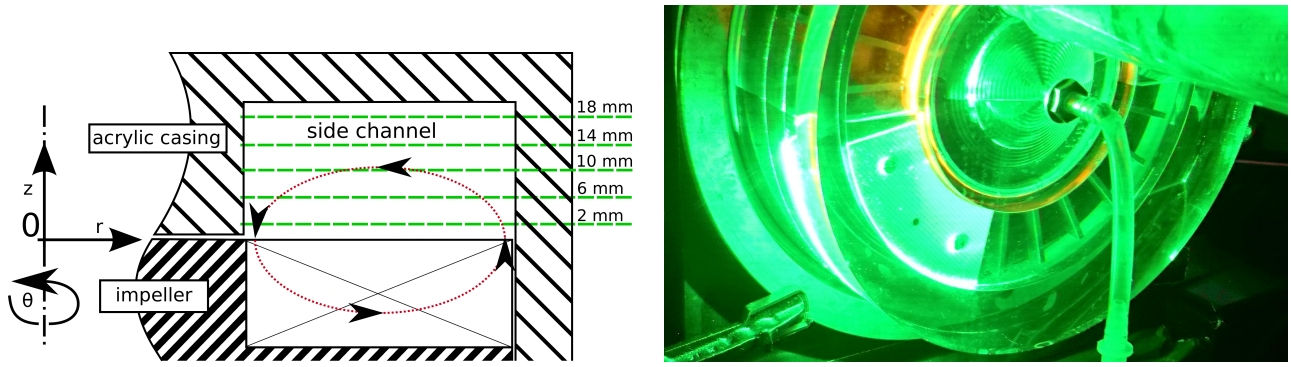

(a) Sectional view through the rotation axes of the machine with indicated measurement planes and circulation flow.

(b) Close up of the mounted calibration target during light sheet alignment for the $4mm$ plane; Partly flooded.

Figure 3.9: Measurement planes and calibration.

To understand the development of the axial flow through the side channel, five planes at different axial positions were measured (indicated together with the circulation flow in Figure 3.9a). As the calibration process of a HS-SPIV system is the most important factor regarding accuracy of the measurement, this was done according to a strict procedure to assure reproducibility: To calibrate the system, a $2mm$ checkered pattern target is mounted onto the impeller with distance of the surface to the blade tip according to the desired measurement plane. Afterwards, the RFP is reassembled, flooded and the light sheet of the laser is adjusted to the target surface to assure position and angle (as can be seen in Figure 3.9b). Cameras are set up accordingly, realigned slightly each time to maximize the resulting ROI. Afterwards the machine is drained again, disassembled and the target is removed. Ultimately, after reassembling again, the whole test rig is flooded and considered fully calibrated. After every series of measurement (One series is defined as the measurement of the same single plane for six different OPs along the characteristic curve, which takes several hours) calibration was done again without readjusting the system to assure position preservation. In case of strong differences between the calibration before and after, the whole measurement series of the current plane had to be rerun, as it could be assumed that the system was moved and therefore the calibration becomes invalid. Although one measurement with 2771 image pairs takes only 1.4 seconds to record, the subsequent transfer of the raw images from the cameras to the computer takes more than 30 minutes, explaining the high temporal expenditure.

3.2.2 Postprocessing

Being an optical measurement technique, PIV is known to produce big amounts of data. As the whole campaign covered three impellers, each measured for six different operating points and five different planes, a total of 90 measurements was done, each consisting of 12 Gigabytes of Raw-data. It becomes obvious that to handle this amount of data, an efficient post-processing

is absolutely necessary. Post-processing itself was split up into two successive steps using two software tools. First the raw image data was converted into gridded flow field information consisting of three- component velocity information for each grid point using a commercial software. Afterwards this flow field data was further process by means of a technical programming language (Neither the configuration of the PIV software, nor the MATLAB code will be described in detail, as this would be beyond the scope of this work. However, important parameters will be pointed out in the following, to provide the necessary information for reproducibility. In-depth information onto this parameters can be found in Raffel et al. [60]).

Flow field conversion

Analysis of the Raw-data was done using "PIVTEC's PIV software bundle Version 3.5.9.1". For each series of measurement a "master" configuration file was generated and afterwards adapted to each measurement by taking OP specific parameters (such as pulse distance or average background) into account. The "master" configuration file was generated according to the following scheme: In a mapping process (using "PIVmap3"), the single- plane calibration images were used to estimate the position of the cameras using an advanced tsai model (Although SPIV calibration accuracy can be increased using a multiple plane calibration, out of reasons of feasibility this was impossible for the project). Based on the model, the raw images can be dewarped. This straightens out the deformed raw images into their real rectangular form. To review the correct alignment, the dewarped calibration images of each camera are overlayed and adapted in transparency and brightness for better readability. The result is a combined image composed of the two dewarped calibration images. Two of those combined images are exemplary shown with Figure 3.10 for the $10mm$ plane. One was taken before, the other one after a series of measurement.

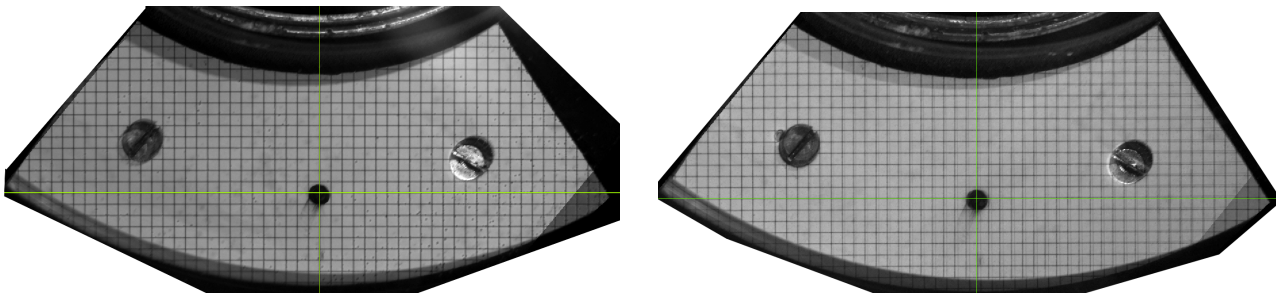

(a) Calibration 1 (Before Measurement). (b) Calibration 2 (After Measurement).

Figure 3.10: Exemplary Overlay of the dewarped calibration images for the measurement series of the $10mm$ plane.

It is visible that for both cases the dewarped checkered pattern from both perspectives within each image align in good agreement. The fact that each image actually is a combined image can be seen by the left screw head. Being slightly above the measurement plane, each camera sees it from the opposite direction. Combination results in a blurry, stretched image of the screw head. Same is true for the right screw head as well, however the effect nearly vanishes, due to the dark shadow while additional strongly reflecting at the same time. Comparing both images enables to evaluate the long term stability (therefore accuracy) of the measurement. As a complete series of measurement with a duration of roughly five hours lies between the two

images and additionally multiple dis- and reassemble cycles of the RFP had been done, the similarity is still within a reasonable deviation (Keep in mind, that the distance between two lines is only $2mm$). The second image seems more blurry; some of the lines appearing twice, especially around the origin and the outer rim. However, the overall agreement between the two grids is considered good enough to state the calibration more or less stable over time. As a second test, the estimated camera position purely generated from the raw images were compared to the physically measured ones. The calibration was considered valid, if both criteria were matched within reasonable margins (Less than 0.5 mm).

Using the obtained mapping, the raw image data is converted to flow fields via "PIVview3C". As the light sheet is aligned manually with the surface of the target, this bears the possibility of adjustment errors. To compensate this, a "disparity correction" is applied. This methods has its limits, therefore the prior adjustment process has to done properly. To suppress steady distortions, the average background image for each camera is subtracted. In addition, masking is applied to regions of questionable or no flow information. The resulting usable image size after dewarping was around $950 * 460px$. With a conversion length of $8.1 - 8.3px/mm$ this results in a flow field area of $115 * 54mm$ with 117 horizontal and 56 vertical nodes. The actual PIV algorithm is set up as a "Multi-grid interrogation" with an initial sampling window of $96 * 96px$ and an overlap of 50% resulting in a final window size of $16 * 16px$. To improve accuracy, a multiple correlation ($3x$) scheme, as well as sub-pixel interpolation is applied. Spacial filtering for each flow field is done by only using a strict dynamic mean test ($2 *$ average velocity $\pm 1 *$ variance). This resulted in an average of around 0.5% invalid vectors per flow field. Nearly all of them could be replaced by their second highest correlation peak. In the present work, pulse distance had to be kept stable at $100\mu s$ for all OPs due to limitations in the early post processing method (This was done as a compromise, as it was known, that a pulse distance adaption would have improved the results. However, later experiments with an adapted pulse distance showed only minor improvement).

Further data processing

To do statistical analysis, as well as to present the results graphically, an extensive frame-work has been programmed using the technical programming language "MATLAB". Basis of this post processing were the result files from the PIVview3C process, providing gridded data. It is known, that PIV is susceptible to errors in case of occurring noise or artifacts. While noise in general can't be specified, artifacts can have multiple sources. Most sources of artifacts, such as blooming effects of agglutinated seeding particles or foreign matter, as well as intensity fluctuation of reflections are covered by the dynamic mean filter explained above. However, some sources had to be specially treated, others are of the more general type. One specific problem is false correlations near walls and as a consequence false gradients to the nearest neighbors. To overcome this, each node was tested against its next neighbors. In case an edge node with a suspicious gradient was detected, it was filtered. In general, this leads to a filtering of all outer border nodes, further minimizing the measured area, but fortifying the measurement certainty. A huge benefit of high speed PIV is the high temporal resolution. This allows additional filtering. As the fluctuation of the observed flow phenomena is not expected to be in the same order of magnitude as the measurement frequency, two different filters were implemented. Either a global mean filter ($2 *$ average velocity $\pm 1.5 *$ standard deviation) or a simple temporal smoothing using a moving average filter were tested on every spacial point of the flow field. However, less

than 0.1 % were filtered and interpolated. As this amount of outliers was negligible, in the end the filter was not used. Yet, this filtering is still considered to be important in case of more noisy data (A more detailed and sophisticated view on the topic of temporal filtering and the corresponding problems can by found in [61]). Ultimately, a total of around 3000 valid nodes, each containing all three velocity components were available for further analyses.

3.3 Integral Operational Data Measurement

To measure the integral operational data of the RFP, common instrumentation has been installed (from here on, said instrumentation is referred to as "Common integral operational data" (COD) measurement). Table 3.4 gives an overview of the used instrumentation, while a connection scheme of the measurement instrumentation is presented with Figure 3.11.

Drive unit	Asynchronous motor; SIEMENS; 1LA7106-4AA10
Torque meter	Contact-less torque sensor; LORENZ; DR-2212-R
Pressure sensor	Differential pressure manometer; Hottinger Baldwin; PD1
Volume flow Q_{Tot}	Inductive flowmeter; Endress+Hauser; Promag 50W
Volume flow $Q_{PIV,POM}$	Vortex flowmeter; Endress+Hauser; Prowirl 77
Data acquisition hardware	Multifunction DAQ; National Instruments; NI-USB-6211
Data acquisition software	Engineering development environment; National Instruments; LabView 2014
Auxiliary pump	Radial Pump; KSB; Etanorm G 065-125 G10

Table 3.4: Measurement and operation instrumentation.

All instruments are connected to a data acquisition (DAQ) hardware (NI-USB-6211) using analog inputs, therefore $\pm 10V$. The flow meters are connected directly, while the rest is connected via according auxiliary converters. Ambient temperature is measured to take density variation into account. As the pressure probe is know to be temperature sensitive, it is enclosed by an isolation box with an additional temperature sensor inside to be able to compensate potential temperature drift of the pressure sensor. To minimize disturbance due to vibrations, the box is decoupled from the test rig. Output of the torque meter consist of two separate signals: nominal torque of $\pm 10Nm$ results in analog $\pm 10V$ signal with the sign according to turning direction. Furthermore the rotation angle is given as a TTL signal with an edge change every single degree. The DAQ hardware is directly connected to a PC running "LabVIEW 2014" from National Instruments. A set of test rig specific programmed "Virtual Instruments" builds the framework for the data logging. For reasons of reproducibility, data was logged in raw voltage values and later on further processed in MATLAB. To be able to capture instationary phenomena, measurement repetition rate was maxed out for every single instrumentation separately. However, only the torque sensor was known to be fast enough to keep up with the 2000 Hz of the PIV System.

Two different measuring task have to be considered. As they differ a lot regarding observation period, sample rates have to be adapted as well: Long term observation is done to measure the characteristic as well as the efficiency curve of the pump using common methods. Every

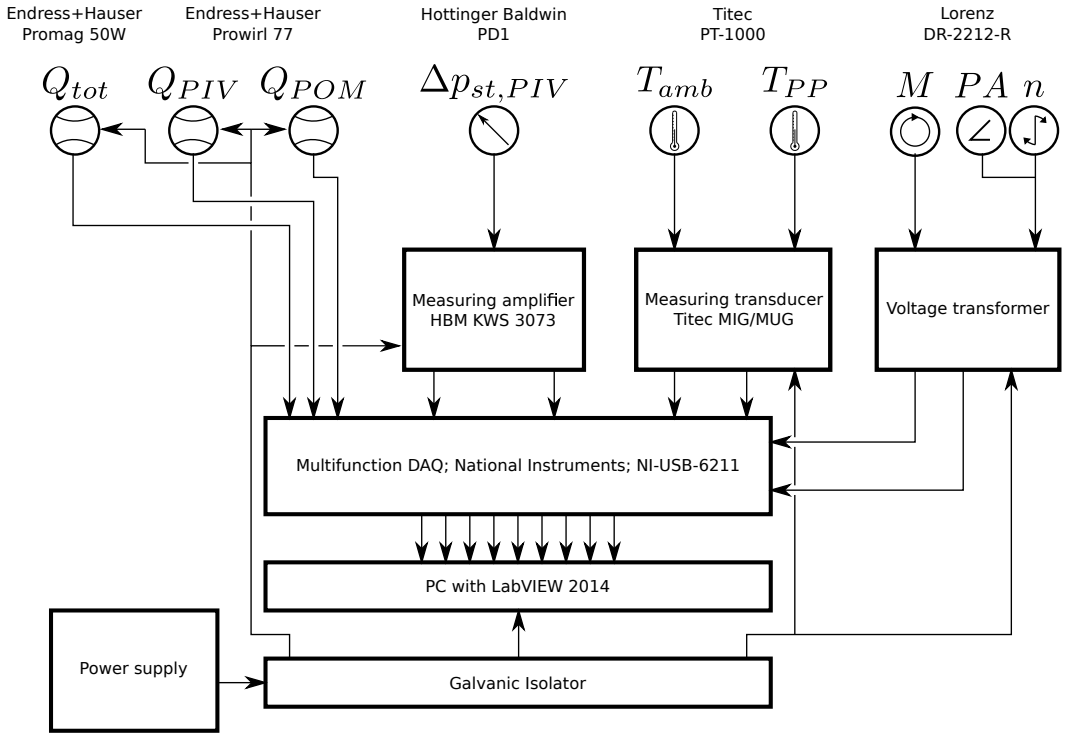

Figure 3.11: Connection scheme of the measurement instrumentation.

operating point is observed for 24 seconds at a sample rate of 1000 Hz to gather statistical significant data. To read out all channels equally, aside from the torque meter, every other sensor system is over-sampled. However, due to internal dampening of the sensors, this has no negative effect on the measurement but gives the great benefit of synchronous data logging on every channel. The second task is to measure during a PIV Measurement series. As the duration of a PIV measurement is only 1.4 seconds, the DAQ has to by adapted. Synchronization of the PIV System and the DAQ System was crucial, therefore an iterative process was necessary. Best results were achieved by splitting the measurement process into two parts: The synchronizer puts the laser system on standby and gives a trigger signal to LabVIEW. Through this, a 4 second "Pre-PIV-Measurement" is initiated with a sample rate of 20.000 Hz to assure magnitude and stability of the current operating point. Afterwards, without gap, a second 20.000 Hz measurement is initiated lasting 4 seconds as well, while triggering the PIV measurement through the synchronizer with precisely one second delay. This way, the summed 8 seconds of measurement assure that the correct operating point was measured, as well as time synchronous common data value to the PIV measurement does exist.

Chapter 4

Data Validation

"A theory is something nobody believes, except the person who made it. An experiment is something everybody believes, except the person who made it." (Albert Einstein)

This well-known quote stands exemplary for one of the biggest problems regarding measurements: Except when broken, sensor systems always generate data; Digital meters show numbers, DAQ measures voltage and PIV results in colorful pictures. If one is aware of this, the most crucial part after gathering the data, is to estimate the accuracy of the measurements. This chapter handles the methods used to validate the data, as well as giving error estimations where possible.

4.1 Integral Values

A detailed description of the common integral value measurement systems, as well as estimations of the error propagation of the used test rig is described in [74].

In general, a measurement result is a statistical distribution of measurement values. A signal observed long enough with a significant amount of data and the assumption of no further influence will show a Gaussian normal distribution. The characteristics of this distribution for N discrete information of x_n can be described with two values:

The **arithmetic mean**, as defined by:

$$\mu = \bar{x} = \frac{1}{N} \sum_{n=1}^{N} x_n \tag{4.1}$$

and the **standard deviation** as defined by:

$$\sigma = \sqrt{\frac{1}{N-1} \sum_{n=1}^{N} (x_n - \bar{x})^2}. \tag{4.2}$$

In technical practice those values are used to express the likelihood of a measured value. A proven method is the "2σ criteria": It states that a value lies within the interval of $\mu \pm 2 * \sigma$ with a confidence level of over 95%. To ensure correctness of these values, an uncertainty estimation has to be made. Measurement uncertainty can be split up in two different categories: statistical and systematic ones (see Gerthsen [62]).

Statistical uncertainty

Statistical uncertainty occurs due to random fluctuation of the measurement instrument as well as due to the experimenter. These uncertainties are uncorrelated with previous measurements and of stochastic nature. As stated above, they are taken into account by σ as all measured signals could be assumed to be Gaussian normal distributed (which will be explained later in this chapter).

Systematic uncertainty

Systematic uncertainties can not be handled according to a scheme. Elimination of these uncertainties is not trivial, but strongly depending on diligence and experience of the experimenter. Error sources which are known and not avoidable by the given means have to be qualitative analyzed and estimated accordingly. To estimate the systematic uncertainty, four sources were identified, with their values given with table 4.1 and which will be explained afterwards. As the total measurement uncertainty is strongly depending on the current OP, no value for a total measurement uncertainty is given, but rather calculated for each OP individually.

Sensor	**Given Error**	**ZPF**	**Temp.-dep.**	**Calib.-error**
Q_{tot}	$0,5$[%] o.r	$10[mV]$	-	-
Q_{PIV}	$0,75$[%] o.r.	$12[mV]$	-	1[%]
Q_{POM}	$0,75$[%] o.r.	$10[mV]$	-	1[%]
Δp	1[%] f.s.	$20[mV]$	$14[mV/K]$	see WCC
M	1[%] f.s.	$10[mV]$	1[%]	1[%]
WCC	-	-	-	Reading error: 0.5[%]
T_{PP} / T_{amb}	-	$20[mV]$	-	-

Table 4.1: Estimated measurement uncertainties.

Given Error (GE)

The measurement error of the instrument according to the manufacturer. "o.r." stands for "of reading" and refers to the current value; therefore is a relative value. "f.s." stands for "full scale" and refers to the maximum measurement range of the sensor, therefore is an absolute value.

Zero point fluctuation (ZPF)

The fluctuation of the electric signal of the unloaded sensor. In a long term observation (100 hours), the zero point fluctuation of each sensor was observed with no observable drift but a Gaussian distribution. The uncertainty for each sensor was therefore stated according to the before mentioned "2σ criteria".

Temperature dependency (Temp.-dep.)

The measurement uncertainty is caused by temperature variation. Due to their functional principle, the signal of the pressure as well as the torque sensor varies according to the ambient

temperature. Fluctuations due to the day and night cycle during the long term observation showed a clear linear dependency for the pressure sensor, which therefore could be formulated and afterwards compensated. The effect for the torque sensor was to small to be statistically significant during the long term observation, therefore the manufacturers uncertainty was used.

Calibration error (Calib.-error)

The most common error in experimental work occurs (as the name suggest) during calibration of a sensor and the appendant auxiliary systems. Therefore calibration of each sensor itself is described in-detail in the following section:

The **inductive volume flow meter** (Q_{tot}) was considered calibrated, as this had been done in a preliminary study on the same test rig and couldn't be repeated with reasonable effort (Therefore no calibration error was assumed and only the given error according to the manufacturer was taken into account). Furthermore, as each **vortex flow meter** (Q_{PIV}&Q_{POM}) was calibrated on basis of the inductive flow meter, no calibration error was assumed as well. However, to ensure that the total volume flow was distributed equally to both lines, the flow through the PIV-side had to be regulated manually on basis of the vortex flow meter (Q_{PIV}) for each OP independently. Although the vortex flow meters showed reasonable quantitative values after calibration, a total uncertainty of 1% was estimated for the volume flow to take the possible unbalance between the lines into account, as the final value for the volume flow through each line was defined as $Q_{tot}/2$ as measured by the inductive flow meter.

The **pressure probe** was calibrated before and after every measurement via a parallel connected water column cascade (WCC) to assure correct values. The cascade provided a maximum total of $4.5m$ of pressure head. Although metering was possible in steps of $0.5mm$, to take personal bias in reading into account, a conservative uncertainty of 0.5% was assumed.

The **torque meter** was calibrated with a $0.5m$ lever arm and corresponding weight in steps of $100g$ leading to a linear dependency. Conversion into torque was done using the gravitation constant of 9.81 m/s^2. Unfortunately, due to the multiple dis- and reassembling in combination with the very small gaps between impeller and casing, it was necessary to slightly realign impeller and shaft before every series of measurement. As this influences the idling torque of the system, a calibration error of 1% was estimated.

The **temperature sensor** was calibrated in a preliminary study as well. Therefore no calibration error was assumed.

Uncertainty propagation

Ultimately, all uncertainties are combined to take error propagation into account. The absolute uncertainty of each combined value (Δy_j) is calculated according to the Gaussian law of error propagation given with equation 4.3.

$$\Delta y_j = \sqrt{\sum_{s_k} \left(\frac{\delta f}{\delta s_k} \right)^2 \sigma_k^2} \tag{4.3}$$

In general, the instantaneous resulting value y_j of a combined parameter j (Total head, volume flow, torque) is a function of multiple measurands (sensor systems) $(s_1, s_2, ...s_k)$. Therefore: $y_j = f(s_1, s_2, ...s_k)$ defines all measurands related to the combined parameter. Functional dependency for the three resulting values of interest are defined as follows:

Volume flow is only a function of the general error, as well as the zero point fluctuation of the sensor itself; no additional influence:

$$y_Q = f\Big((GE + ZPF)_{Sensor}\Big)$$

Total head is a function of all three parameters of the sensor itself. As the pressure sensor has a temperature dependency which is compensated, the influence of the temperature sensor has to be taken into account as well. Last influence is the uncertainty component due to WCC calibration:

$$y_{H_{tot}} = f\Big((GE + ZPF + Temp.{-}dep.)_{Sensor}, (ZPF)_{Temperature}, (Calib.{-}error)_{WCC}\Big)$$

Torque is a function of all influence values of the sensor. Due to the temperature compensation depending on temperature as well:

$$y_M = f\Big((GE + ZPF + Temp.{-}dep. + Calib.{-}error)_{Sensor}, (ZPF)_{Temperature}\Big)$$

Once combined, the two resulting total uncertainties in both directions (i.e. $\Delta y_{H_{tot}} \& \Delta y_Q$) can be shown for each OP individually. To explain how this is done in the upcoming chapter, Figure 4.1 is introduced. It shows the characteristic curve in absolute values for an arbitrary measurement series for the 24 blades impeller at 500 rpm. Measurement time for each OP was 15s with a sample rate of 1000Hz and was triggered when the OP was considered stable. The arithmetic mean of each OP is shown as a blue line, while all measured values pairs are shown as blue dots. The measurement uncertainty for each OP is indicated by a magenta rectangle, with the height being defined by the uncertainty of the ordinate variable (here: $\Delta y_{H_{tot}}$) and the width being the uncertainty of the volume flow. The vector addition of the maximum uncertainties in both directions for each OP (the worst case) are connected by a dotted magenta line. Therefore the physical correct value of each OP lies within the band of the two dotted lines. It can be assumed that this is also the case for any OP in between. There is a visible tendency that the uncertainty in part load is dominated by the influence of the pressure senor, while being more influenced by the volume flow meter in overload. This is due to the relative uncertainty dependency of most sensors: Higher values lead to higher uncertainties. The position of the OPs during a PIV measurement series are marked with red circles. To emphasize the statement that each signal was Gaussian normal distributed, four histograms are given. They show the distribution of the total head, as well as the volume flow for the nearest points (green circles) to the two most extreme OPs of each PIV measurement series (OP1 & OP6). The distribution itself is shown as a bar plot, while the according normal distribution as well as the "2σ criteria" are given in blue. The area of measurement uncertainty is bordered with the two magenta lines and the mean value is given as a black line. As all "2σ criteria" areas are wider than the measurement uncertainties areas, it can be assumed that for both OPs the distribution of the values is related to fluctuation of the fluid.

To sum it up, it can be stated that due to the apparent normal distribution of measurement values for each OP, the OP itself can be expressed by its arithmetic mean value. However, the real physical value lies in between the interval of the uncertainties.

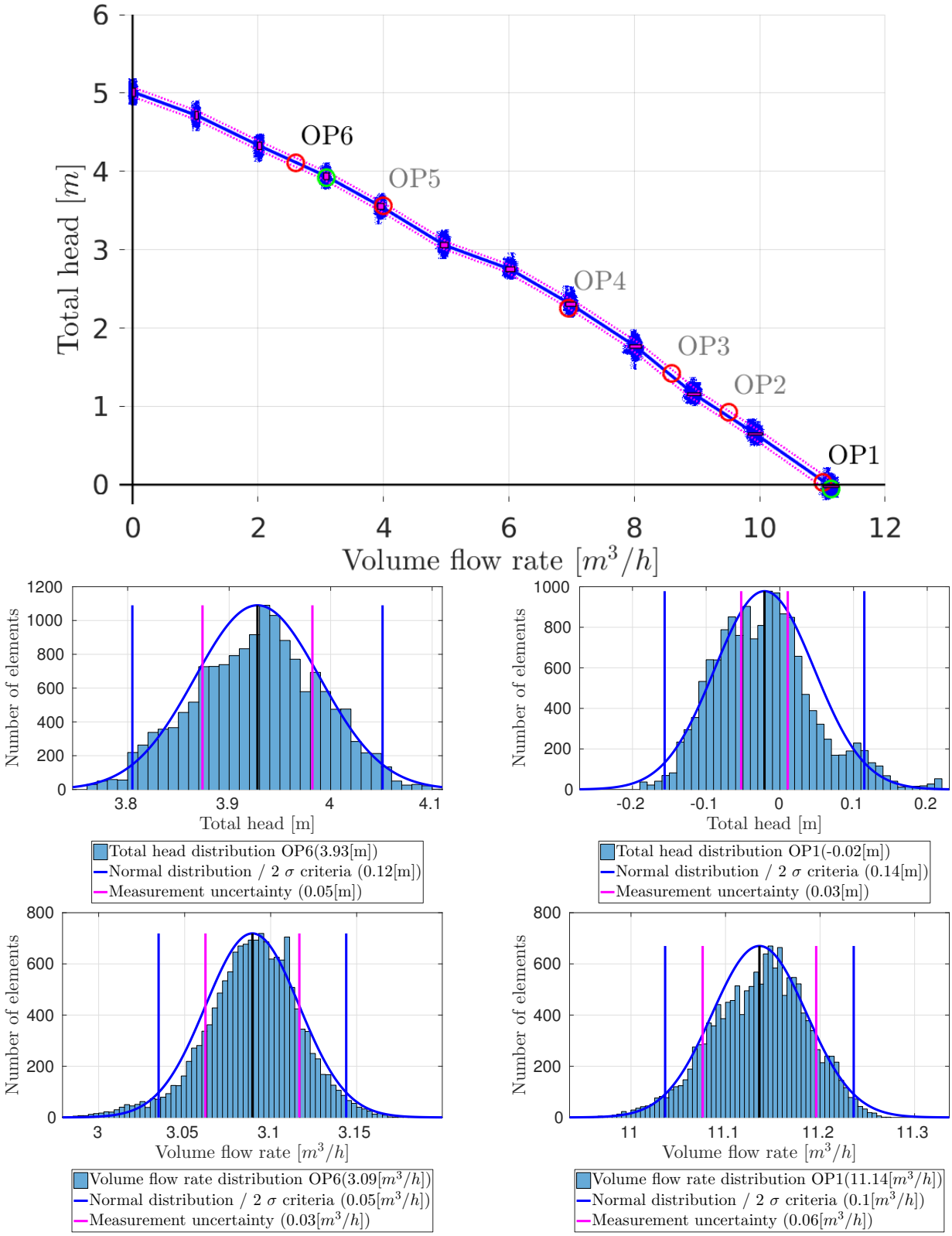

Figure 4.1: Characteristic curve for 24 blades at 500 rpm. Total Head and volume flow rate histograms for the OPs marked with green circles shown below.

4.2 Measurement system coupling

As explained in the previous chapter, high resolution temporal synchronization of two separate measurement systems is not trivial. A special challenge was the allocation of the phase angle to every single PIV Snapshot. The used PIV System, most important the synchronizer from ILA GmbH (which is specially designed to handle such extremely short switching delays with its 5 ns resolution), is very stable regarding frequency fluctuation. Therefore it could be assumed that the measurement frequency was fixed throughout the whole measurement, thus allocating a time-stamp to every PIV Snapshot according to the frequency of 2000 Hz was possible. In case of LABview and its sequential input readout, it was more challenging to allocate multiple signals measured at a high sampling rate to the same time-stamp with the necessary precision. In an iterative design process([75]), which benefited from earlier work ([73]), it was possible to achieve this despite a crucial trigger circuit design disadvantage: only one single pulse started both systems at the same time, while no additional synchronous event happened afterwards. To assure synchronous time-stamps on both systems, it has been proven advantageous to trigger LABview one second before the actual measurement through the synchronizer (Although in theory a "zero-delay" should have been possible as well, reality during experiment showed asynchronous or non-uniform time-stamps as well as missing PIV data). This one second of synchronized "pre-measurement ready state" enables both systems to "even out" separately. In case of the PIV System, this means synchronization of both Laser cavities and the according Q-Switches. In case of LABview this means preallocation of memory and synchronization of readout channels and time-stamp.

Another challenge laid in the mechanism of time-resolved PIV measurement itself: It is triggered only once, then starts recording with a fix measurement frequency and ends when the available data storage of the cameras is full. As continuously recorded data was of the essence, no phase-triggered time-resolved recording was possible. With the PIV measurement frequency of 2000 Hz, the speed of the machine set to 500 rpm and with the impeller having 24 blades, this would results in exactly 10 distinct measured flow fields per blade passage at 10 distinct phase angles. Figure 4.2 clarifies this for the M6 (PL) measurement data for the 2mm plane.

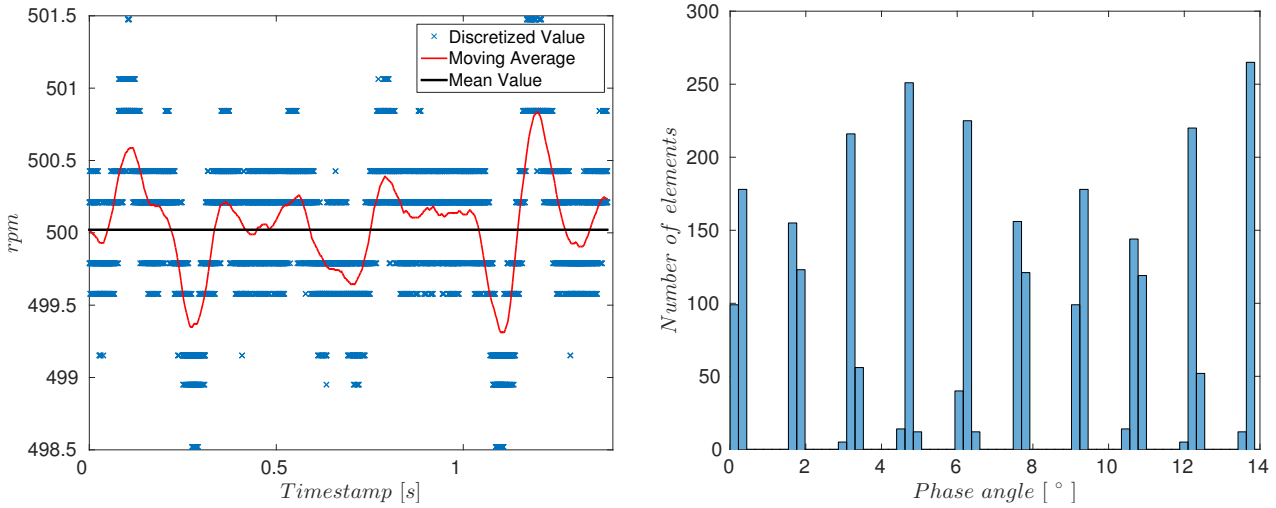

Figure 4.2: Rpm evolution and phase angle distribution for M6 (PL).

On the left hand side, the fluctuation of speed during a measurement is shown. The right hand

side shows the resulting phase angle distribution of every PIV Snapshot. As the average speed during measurement is very close to 500 *rpm* the ratio between blade passing frequency and PIV measurement frequency is in whole numbers, thus resulting only in distinct phase angles with a spread of only around 0.5°. It is obvious to see that a phase averaging is clearly possible.

However, as the frequency converter which was feeding the motor wasn't adapted during a measurement cycle through all OPs, the desired speed of 500 *rpm* was not constant for all OPs. In addition, random disturbances lead to fluctuations of the speed during measurement. Therefore the speed differed about 5 rpm from OL to PL and measurement to measurement. This resulted in different data sets for phase averaging regarding angular position distribution. Figure 4.3 shows the M1 (OL) measurement data for the 2mm plane.

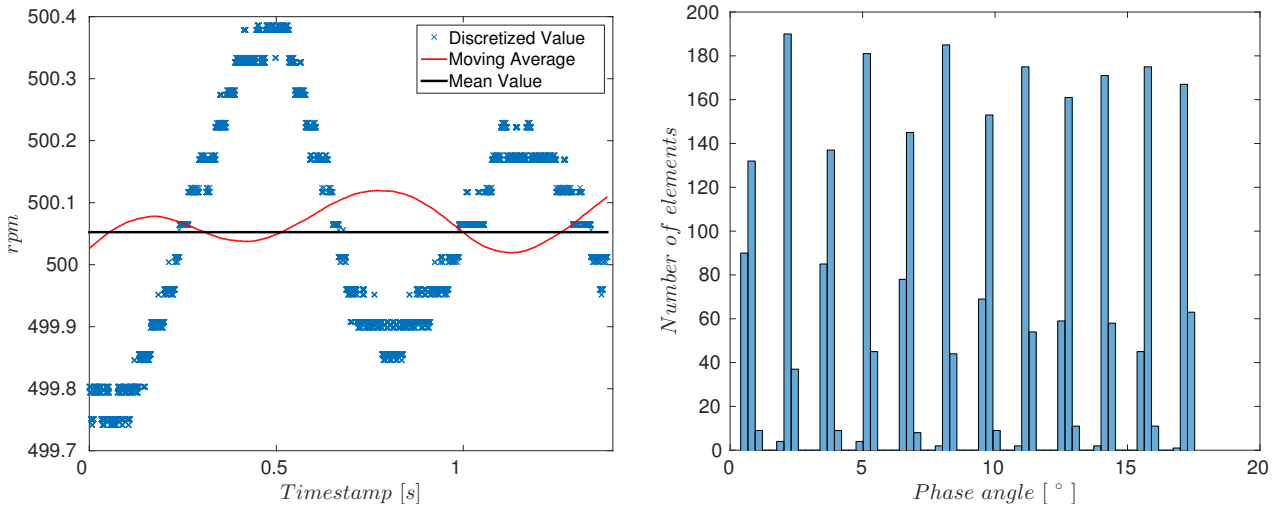

Figure 4.3: Rpm evolution and phase angle distribution for M1 (OL).

Speed is around 495.5 *rpm*, which leads to a phase angle distribution as can be seen in on the right hand side. A distinct allocation is not possible anymore. In this case phase averaging was realized by discretizing all data into 10 phase angle "blocks" similar to the ones for 500 *rpm*. The spread of each phase angle inevitably therefore increased to 1.5°. To verify proper functionality of the trigger system (and the connected proper handling of the aforementioned problems regarding synchronicity of time-stamps) as well as to evaluate the usability of differing phase angle spread the following method was used: All PIV raw data (therefore raw images) of one camera for the first phase angle were combined to a single averaged image. The resulting brightness-adapted average image out of 271 raw images is shown with Figure 4.4 for the aforementioned cases M1 and M6 of the 2mm plane.

Due to phase averaging, the actual position of the blades is clearly visible, while the particles vanish into a mean value. Now a former problem can be used as an advantage: The unwanted, but unavoidable reflection on the pressure side of each blade due to scattering effects of the light sheet (recall that the laser enters from the left) can be used as position information. The calculated position of the suction side of blade "zero" according to the LABview time-stamp is marked as a red line. It is clearly visible that for both cases the calculated, as well as real the position match within a very small margin (less than 0.5°). In addition, the image also reveals the effect of the different phase angle spreads: The small spread of 0.5° in PL results in a very sharp image (recall that the image is combined out of 271 single images), while the spread of 1.5° in OL results in a slightly blurred image. Nonetheless, the images prove that synchronicity

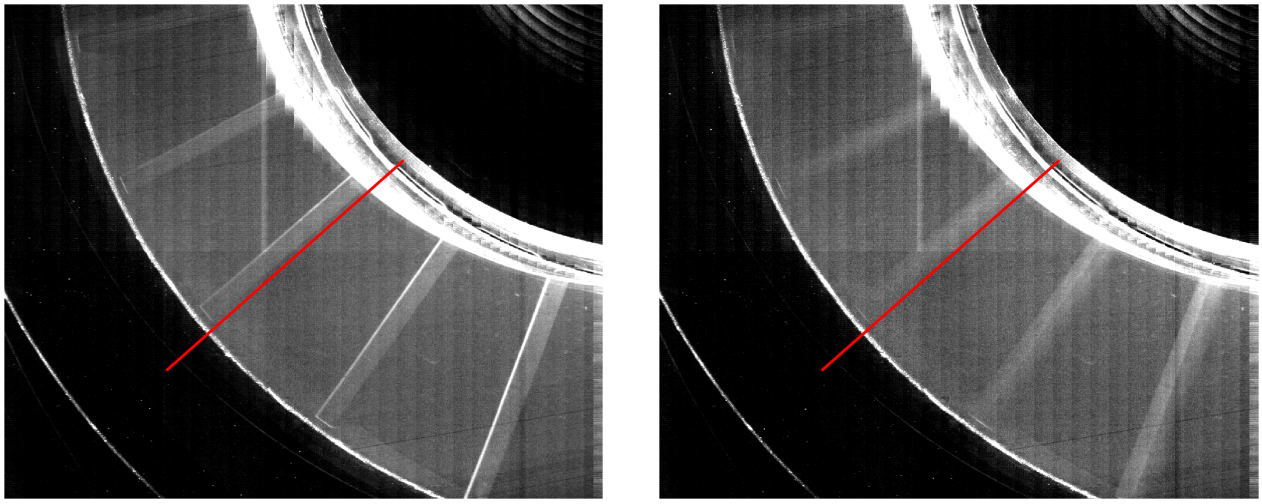

(a) M6: part-load; z=2mm.

(b) M1: overload; z=2mm.

Figure 4.4: Mean phase average raw data for the 2mm plane with clearly visible reflections. Calculated suction side position of the blade indicated by a red line.

of both systems is given, as well as that the different phase angle spreads are small enough to do proper phase averaging within the margins of the given conditions. Validation is only shown for OL and PL, but was done for the remaining OPs accordingly.

Axial limitations: As reflections diminish with increasing axial height of the light sheet, this phase angle verification was only reliable for the 2&6mm plane. For the remaining planes $10 - 18mm$ the blade angle positions can only be adumbrated (compare Figure 4.5). However, as it could be verified for each OP in two planes, it was assumed for the remaining planes as well. Nonetheless it would be theoretically possible that the circumferential starting position of planes $10 - 18mm$ could differ up to 5°. Correctness of proper phase averaging is not affected by this issue.

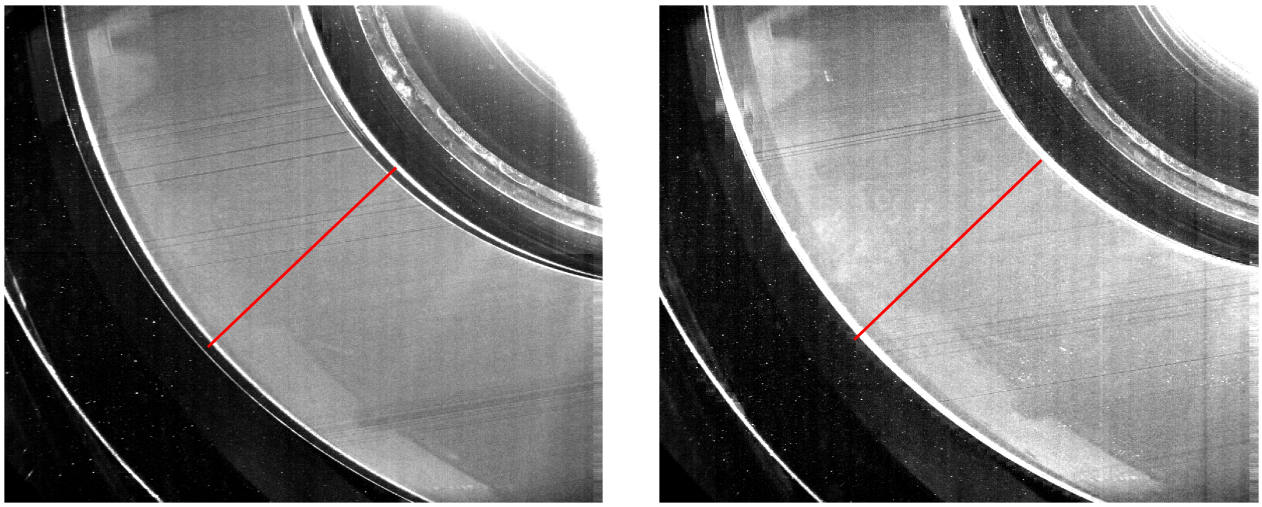

(a) M3; z=14mm.

(b) M3; z=18mm.

Figure 4.5: Mean phase average raw data for OP3 for different planes. Calculated suction side position of the blade indicated by a red line.

Chapter 5

Results: Integral operational data

Although the whole campaign covered three impellers (20,24,28 blades), the enormous time and effort to post process the gathered PIV data made it impossible to consider all three within the scope of this work. Therefore, the later PIV chapter will only focus on the impeller with 24 blades. However, as analyzing the "Common integral operational data" (COD) was done following a standardized scheme, it was possible to consider all three impellers. The following chapter will describe the characteristic curves of the machine, regarding both, total head and efficiency over volume flow rate.

5.1 Performance Characteristics

Up to this point, characteristics of the machine were presented in terms of descriptive dimensionful units such as $[m], [m^3/h]$ or $[Nm]$. This enables to get a first glance on the parameters in game, as well as a first impression of the dimensions in general. In case of fluid machinery however, it is more common to use dimensionless units. This enables to quantitatively compare different machines more easily. This is especially useful in the present case, as all impellers had the same geometrical dimension and were operated within the same test rig and casing as well. Therefore the only difference being the number of blades. The total head H_{tot} as well as the volume flow rate Q are made dimensionless by using characteristics of the impeller and are given by the conventional most common dimensionless terms with Equations 5.1 & 5.2.

Head coefficient:

$$\Psi = \frac{2Y}{u_{imp}^2} = \frac{2gH_{tot}}{\omega^2 r_{imp}^2} = \frac{2gH_{tot}}{(\pi n D_{imp})^2} \tag{5.1}$$

Flow coefficient:

$$\phi = \frac{c_{sc}}{u_{imp}} = \frac{Q}{\pi n D_{imp} A_{sc}} \tag{5.2}$$

- Outer circumferential velocity of the impeller $u_{imp} \approx 5[m/s]$.
- Diameter of the impeller $D_{imp} = 0.2m$.
- Side channel cross section area $A_{sc} = \text{height}_{sc} * \text{width}_{sc} = 0.04m * 0.02m = 0.8^{-3}[m^2]$.

- Rotation speed of the machine $n = 500rpm \hat{\approx} 8.33[1/s]$.

Efficiency is calculated according to equation 5.3.

Efficiency:

$$\eta = \frac{P_{eff}}{P_{Shaft} * 0.5} = \frac{\rho g Q H_{tot}}{\omega M * 0.5} \tag{5.3}$$

The effective hydraulic power ($P_{eff}[W]$) is depending on flow parameters, while shaft power ($P_{shaft}[W]$) depends on the measured torque. It is crucial to understand that all results are given for a single flood (The PIV side). While volume flow, as well as pressure rise are directly measured only for the single PIV flood, this is not the case for torque: It is measured directly at the shaft, therefore in total for both floods. However, as it is assumed that both floods operate equally, torque for a single flood is calculated by multiplying it with 0.5 (See 5.3).

5.1.1 Total head coefficient Ψ and efficiency η

To give an overview regarding reproducibility of the results, the dimensionless total head coefficient Ψ as well as the efficiency η for the "PIV-side" are shown over the flow coefficient ϕ for all three impellers in Figures 5.1 (20 blades), 5.2 (24 blades) and 5.3 (28 blades).

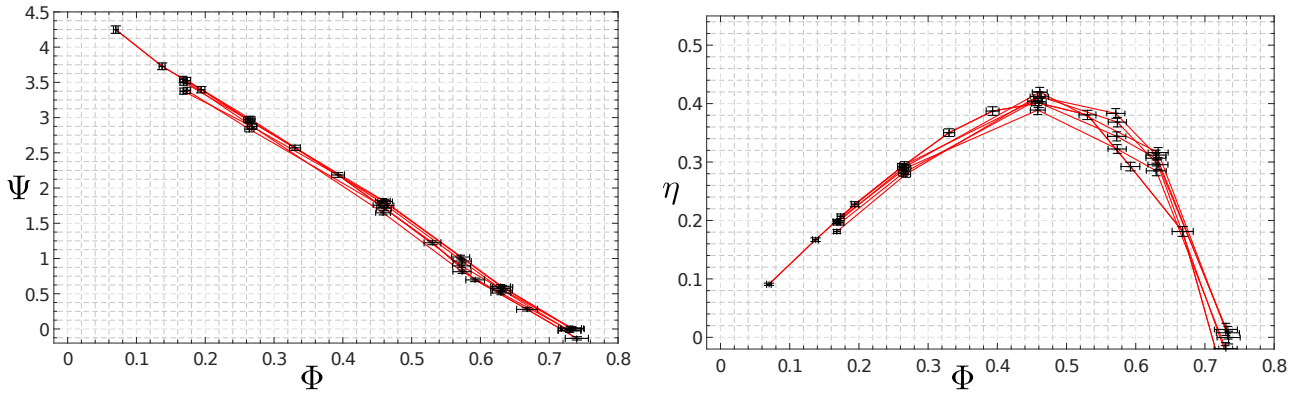

(a) Total head coefficient.

(b) Efficiency.

Figure 5.1: Dimensionless coefficient Impeller 20 blades.

Each figure contains all data from each run done with the specific impeller, thus resulting in an overlay of all the measured characteristic curves. In addition, the uncertainty rectangle for each OP is shown as well (Spreading between $0.16 < \phi < 0.75$). It can be seen, that for the head coefficient the values overlap quite well within the margins of the measurement uncertainty, with only few minor outliers. Therefore the results are considered reproducible. Regarding efficiency, the results are wider spread. This is most probably due to the occasionally necessary realignment of the shaft, which as stated before, can be assumed to be the strongest source of bias in torque measurement. In addition, it is visible that the efficiency uncertainty is homogeneous along the curve. This results from efficiency depending on all measured variables, therefore bearing the highest uncertainty in general, as all uncertainties have to be taken into account according to equation 4.3. It is visible that results are mostly within the uncertainty, with only a few minor outliers as well. An exception is the impeller with 20 blades. Values differ apparently, especially

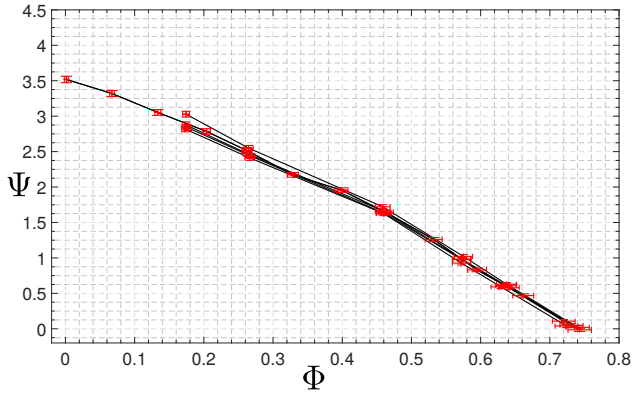

(a) Total head coefficient.

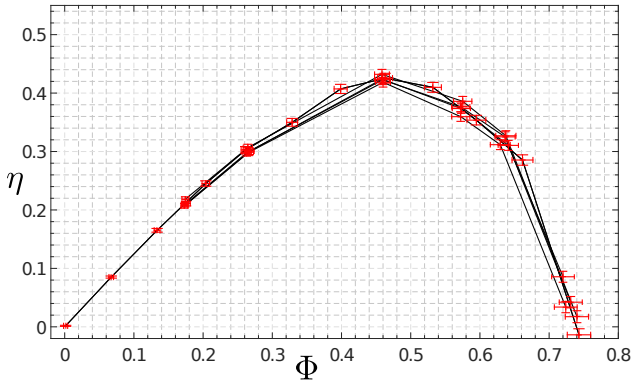

(b) Efficiency.

Figure 5.2: Dimensionless coefficient Impeller 24 blades.

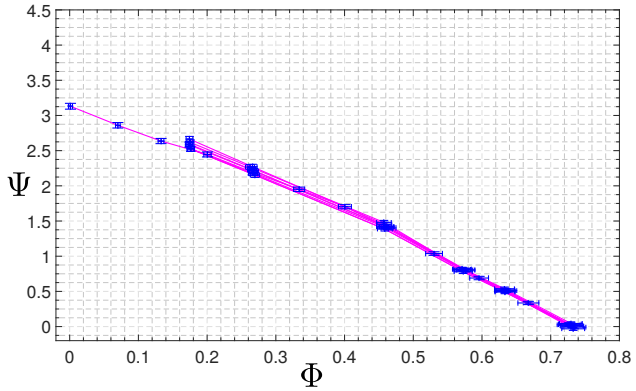

(a) Total head coefficient.

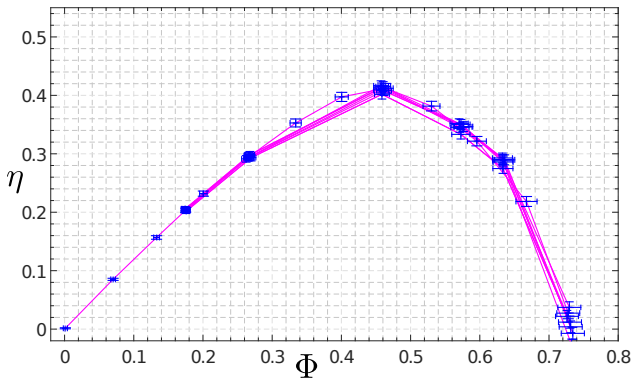

(b) Efficiency

Figure 5.3: Dimensionless coefficient Impeller 28 blades.

right of the BEP in overload. As there was no significant difference in comparison with the other impellers regarding the measurement itself, it is assumed, that the spread has to result from the impeller itself. However, as this work is mainly focusing on the impeller with 24 blades, this is not examined in detail any further and a decent explanation can not be given.

5.1.2 Impeller comparison

To be able to compare the different impellers quantitatively, the average dimensionless characteristic curves (CCs) for the "PIV-side" of all three impellers together with their uncertainties are given with Figure 5.4. In a first approximation, all total head CCs show the steep, quasi

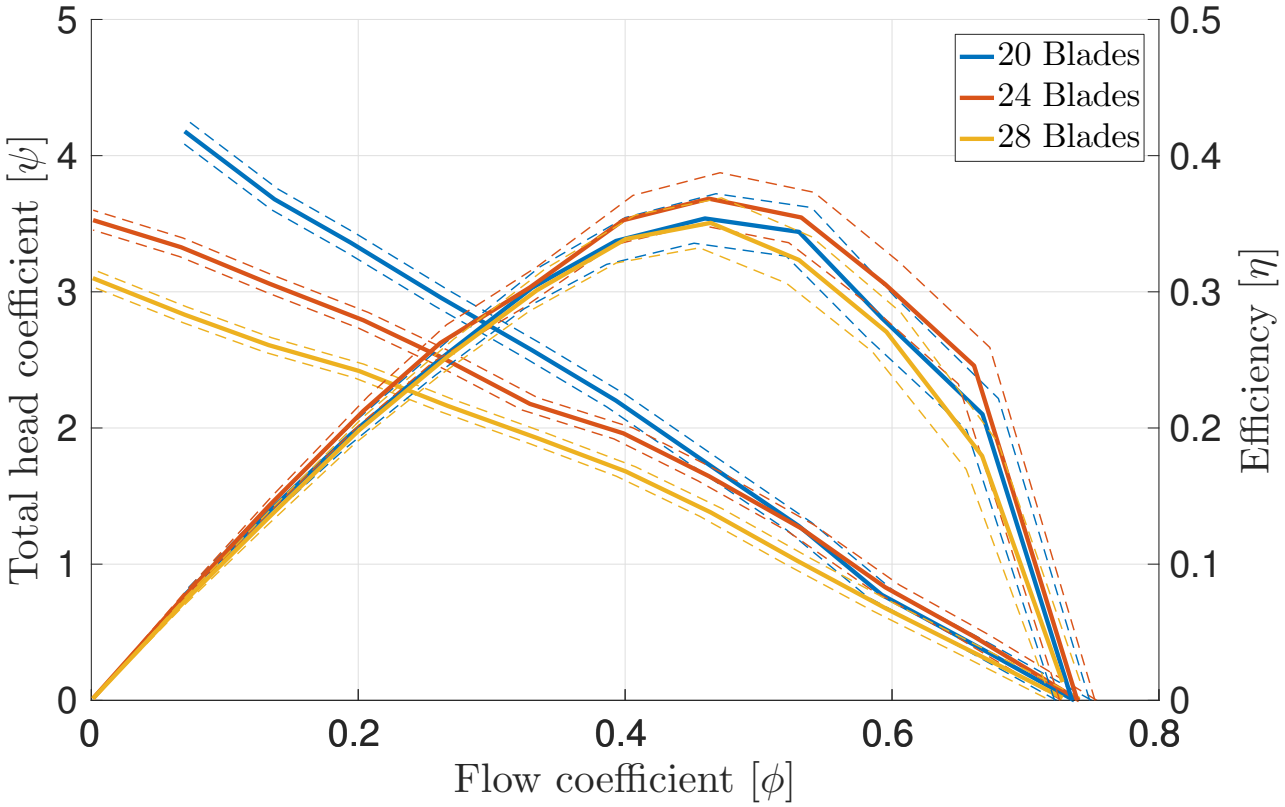

Figure 5.4: Dimensionless characteristic curves (—) of all three impellers with their corresponding uncertainties (- - -).

linear tendency as described in the early publications given in chapter 2. The same is true for the efficiency as well. The ratio between efficiency and flow coefficient is nearly 1 for $\phi < 0.3$ for all impellers and from there on starts to differ. BEP of all three impellers is around $\phi = 0.48$. Although is seems that the impeller with 24 blades has the highest efficiency, this can not be stated in general. Due to the wide measurement uncertainties, it would even be possible for them to be in reversed order. In case of the total head, uncertainties are significantly smaller. It is visible that while being quite similar in high overload mode, they start to differ with $\phi < 0.6$. Around their BEPs, 20 and 28 blades are still quite similar, but then start to differ as well.

Generally spoken: the 20 blades impeller generates the highest head, while the 28 blades impeller the lowest. As the machine was designed for 24 blades (especially regarding the span of the stripper) this is not as expected. However, regarding efficiency, the 24 blades impeller reaches the highest values.

Chapter 6

Results: PIV - Time averaged $\overline{TA}$

The upcoming chapters aim to give a deeper insight into the complex flow behavior within the side channel of the regenerative pump. Starting with common time averaged results, the complexity increases via phase averaged results up to a more advanced approach of combining both. One of the most common approaches in analyzing flow field information is to locally average the given data over time (Time averaging). This gives a first impression on how the flow is developing and therefore a deeper understanding of the occurring flow situation. The campaign consists of six different Operating Points (OPs) ranging from Overload (OL) (OP1) to Partload (PL) (OP6), with the best efficiency point (BEP) being close to OP4. All six OPs were measured for each of the five planes [2,6,10,14,18 mm] (recall Figure 3.9a). As the 2 mm plane is the closest to the impeller, this chapter focuses on said plane for different OPs. Later on, different planes are discussed as well, however only for OP3. Due to uniformity, figures of the flow field are presented similar. It is explained exemplary for Figure 6.1, but applies to all following figures as well:

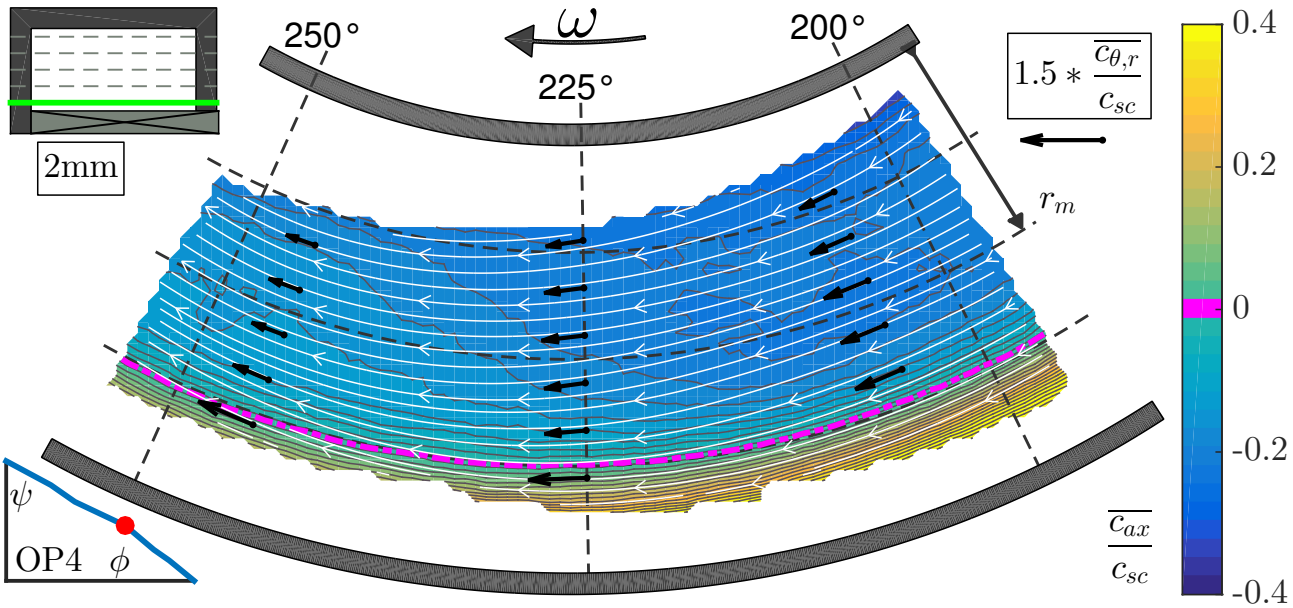

Figure 6.1: Exemplary mean velocity components in the 2mm plane for OP4 (BEP).

Selected Flow information is given as contour plot, with the colorbar indicating the levels. Zero crossing of the contour variable is indicated by a dotted magenta line. On the lower left to the colorbar, the plotted component is given. For comparability, components are normalized by the mean side channel velocity, according to the current volume flow:

$$c_{sc} = \frac{Q}{A_{side\ channel}} \tag{6.1}$$

This mean velocity is linked to the current operating point shown together with the characteristic curve in the left lower corner. In-plane velocity distribution is given by planar streamlines, with an overlying quiver plot to enable quantification (length and corresponding magnitude of a reference vector are given on the upper left side of the colorbar). θ is defined in rotating direction of the impeller (ω), therefore clockwise. The outer limits of the side channel are indicated by thick black arcs. To clarify the positions within the flow field, geometrically characteristic orientation lines along the circumference, as well as the radius are given by dashed gray lines for distinct θ and r. On the upper left, an indicator shows the current plane. This schema applies to all shown vector fields likewise. It is clearly visible that the measured area does not cover the whole side channel. This is a common problem of Stereo-PIV and the corresponding challenging optical access. Due to the complexity of the flow, missing areas are spared instead of extrapolated, as this would be too speculative.

6.1 Mean Flow Fields $\overline{c_i}(\theta, r, z)$

Figures 6.2 and 6.3 show all three time averaged mean velocity components for all six measured Operating Points in the 2 mm plane normalized by the mean side channel velocity c_{sc} (Eq.:6.1). Time-averaged absolute velocity distribution $\overline{c_i}(\theta, r, z)$ (compare eq. 4.1) is calculated according to:

$$\overline{c_i}(\theta, r, z) = \frac{1}{N} \sum_{n=1}^{N} c_i(\theta, r, z, t_n) \tag{6.2}$$

With N being the number of total samples (2771 snapshots) and c_i being the current snapshot composed out of all three velocity components i at time t_n for the local point (θ, r, z).

As OP 1-3 are quite close to each other, the in-plane flow situation is similar regarding direction and magnitude, with the streamlines tending to be less bended in case of higher volume flow. For BEP (OP4), the streamlines are roughly parallel to the side channel walls and nearly have a circular shape. In partload mode however, the flow situation drastically changes, showing a more complex flow field. The circumferential velocity component ($\overline{c_u}$) increases near the outer limit of the side channel, while even showing backflow for small radii. The axial component ($\overline{c_{ax}}$) shows similarities for all OPs, only changing magnitude with increasing pressure head. Remarkable is the position of the outer zero-crossing, which seems to be stable for all OPs. The radial component ($\overline{c_r}$) is very low for OP 1-4, while being quite complex for OP 5&6.

The averaged flow fields provide a good first insight to understand the flow situation in general and its development. It is directly visible that different operating conditions have strong influence on the resulting flow patterns. Showing rather intuitive, mass flow driven, homogeneous ones in OL up to quite complex patterns in PL. It is remarkable to see that in PL mode even back-flow occurs (One has to keep in mind, that the absolute in-plane velocity is drawn; therefore back-flow occurs against the impellers sense of rotation as well as against the direction of the main

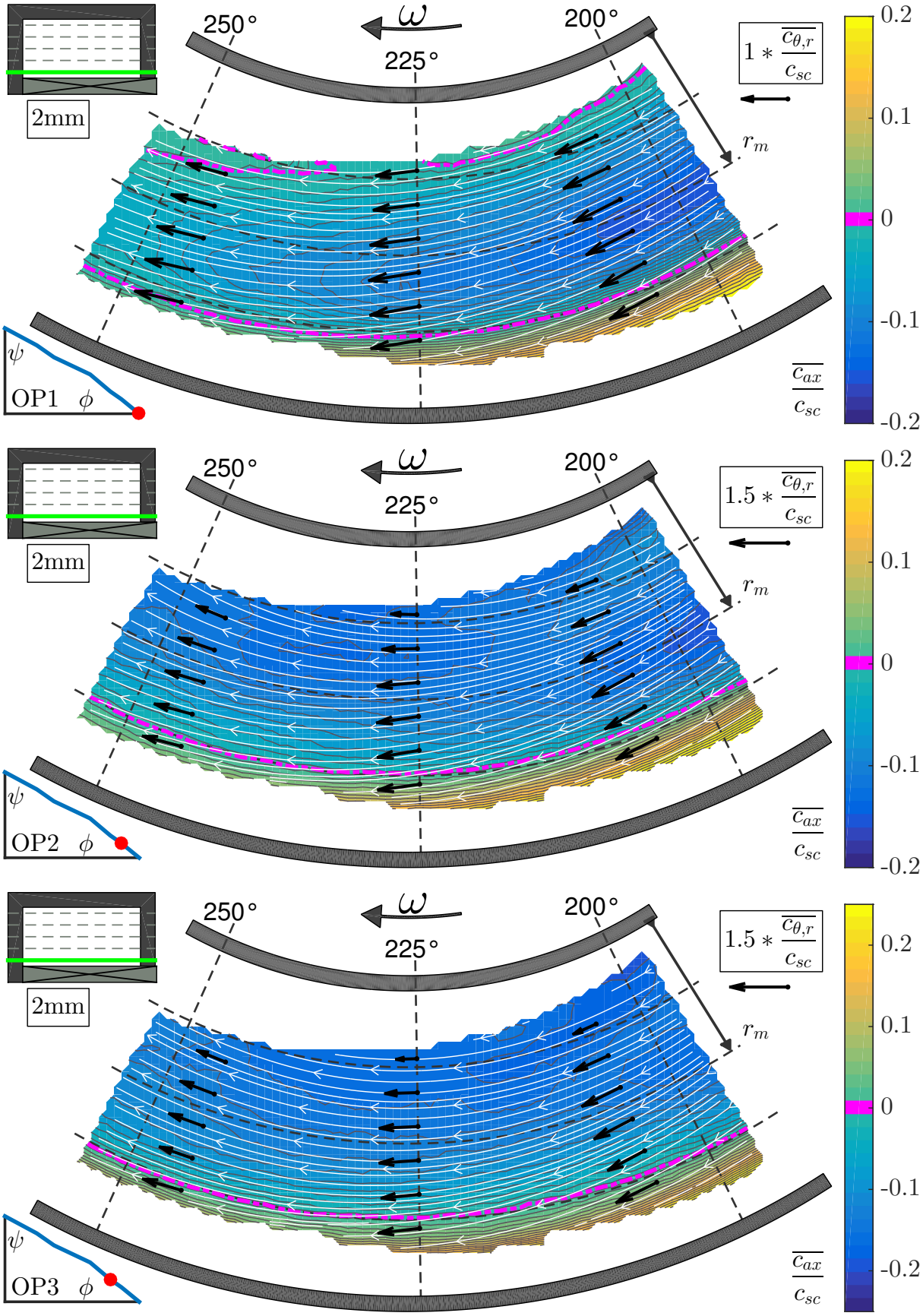

Figure 6.2: $\overline{TA}$ flow fields $\bar{c}(\theta, r, 2mm)$: OP1 to OP3.

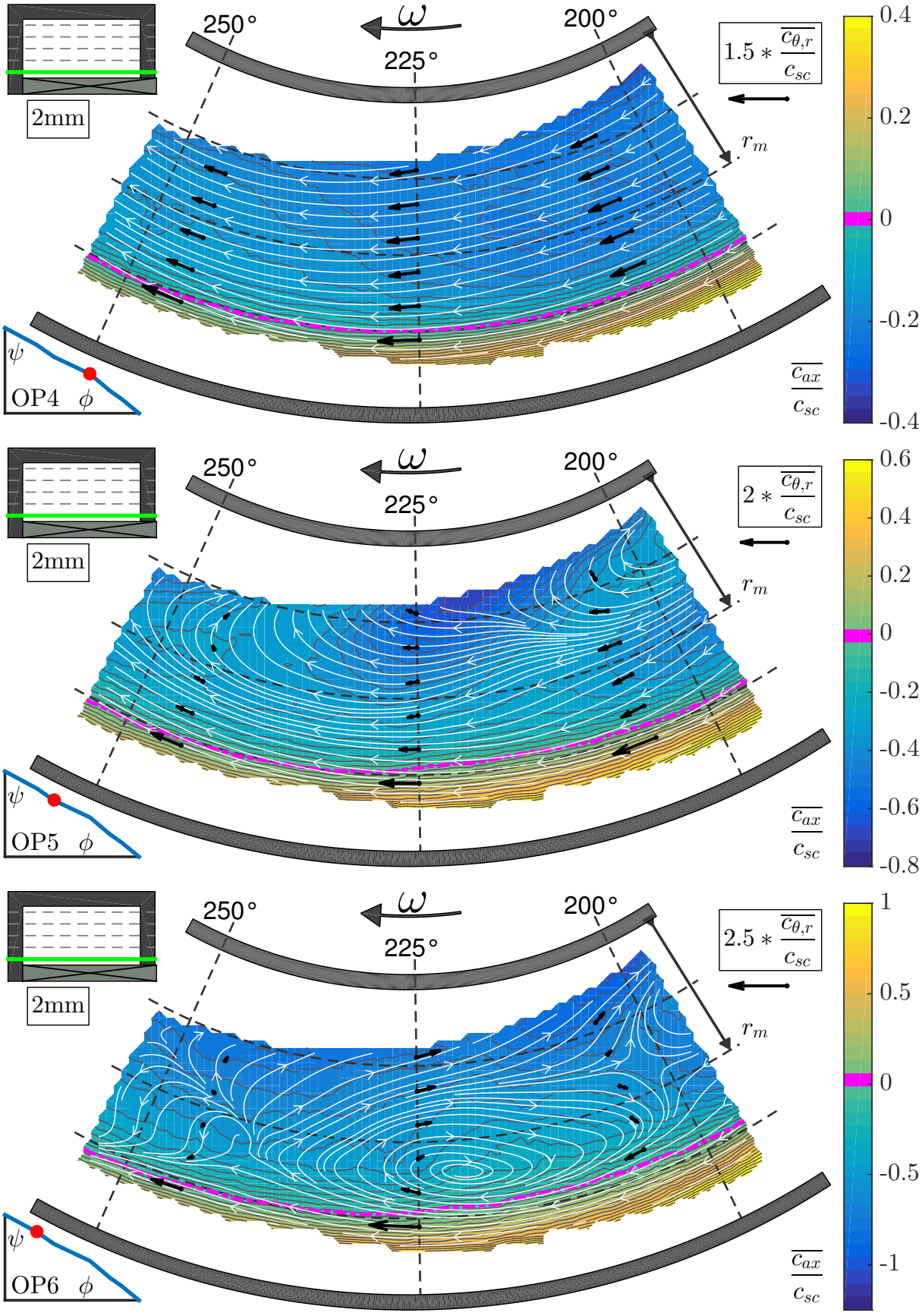

Figure 6.3: $\overline{TA}$ flow fields $\bar{c}(\theta, r, 2mm)$: OP4 to OP6.

flow). The diversity of patterns implicitly indicates the strong influence of the axial interaction between impeller and side channel on the circumferential main flow. However, the complexity of information makes it difficult to analyze distinct differences or compare quantitatively.

6.2 Radial Profiles

To be able to compare quantitatively, splines are extracted along different axes for dedicated positions as indicated in Figure 6.4.

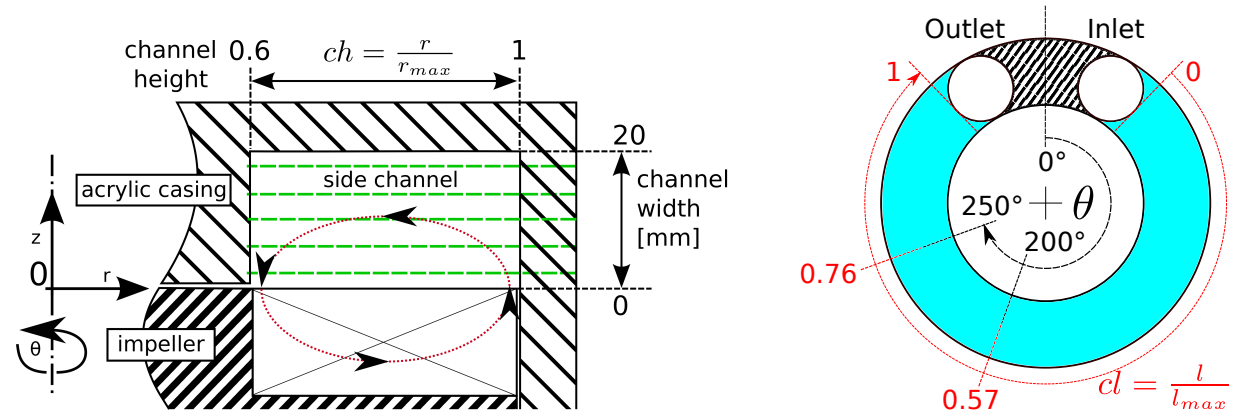

(a) Radial cut with normalized axial measurement planes

(b) Top-down view with indicated circumferential positions

Figure 6.4: Position of the extracted splines

Characteristic length scales are normalized using specific machine dimensions: As can be seen in Figure 6.4a, the radial extent is normalized with the outer impeller radius ($r_{max} = 100mm$), leading to a side channel height between the inner ($r = 60mm$) and outer casing ($r = 100mm$) of $channel\ height : 0.6 < ch < 1$. The circumferential extent is normalized using the side channel length. This leads to a circumferential side channel length of $0 < cl < 1$, as can be seen in Figure 6.4b. The extracted splines are introduced with Figure 6.5.

It shows all three normalized velocity components extracted separately *along the radius* for all six OPs and at two different circumferential positions [$\theta = 200°(cl = 0.57)$ *and* $\theta = 225°(cl = 0.67)$] (compare dashed gray lines in Figure 6.1). Zero-crossing of the ordinate is marked as a dashed red line, the characteristic ratio $c_i/c_{sc} = \pm 1$ as a dashed black line. To be able to easily compare differences between the two circumferential positions θ, scaling for each velocity component is fix. As magnitude differs significantly between the different components, a moderate moving average filter with a width of 5% of the total data length was used to dampen outlier and smooth tendencies for better readability (This applies to all following extracted velocity profiles; the parameter of 5% has been iteratively chosen to prevent strong influence on the drawn conclusions).

Normalized with the mean side channel velocity (c_{sc}), the circumferential velocity components ($\overline{c_u}$) nearly overlap for OPs of high and medium volume flow (OP 1-4) for a wide range of the channel spread ($0.7 < ch < 0.85$). Significant differences are only visible in PL (OP 5&6). In general, $\overline{c_u}/c_{sc}$ stays around 1 for most OPs and a wide range. Therefore c_{sc} as normalization for the main driving force behing the volume flow through the channel (c_u) is reasonable. Starting

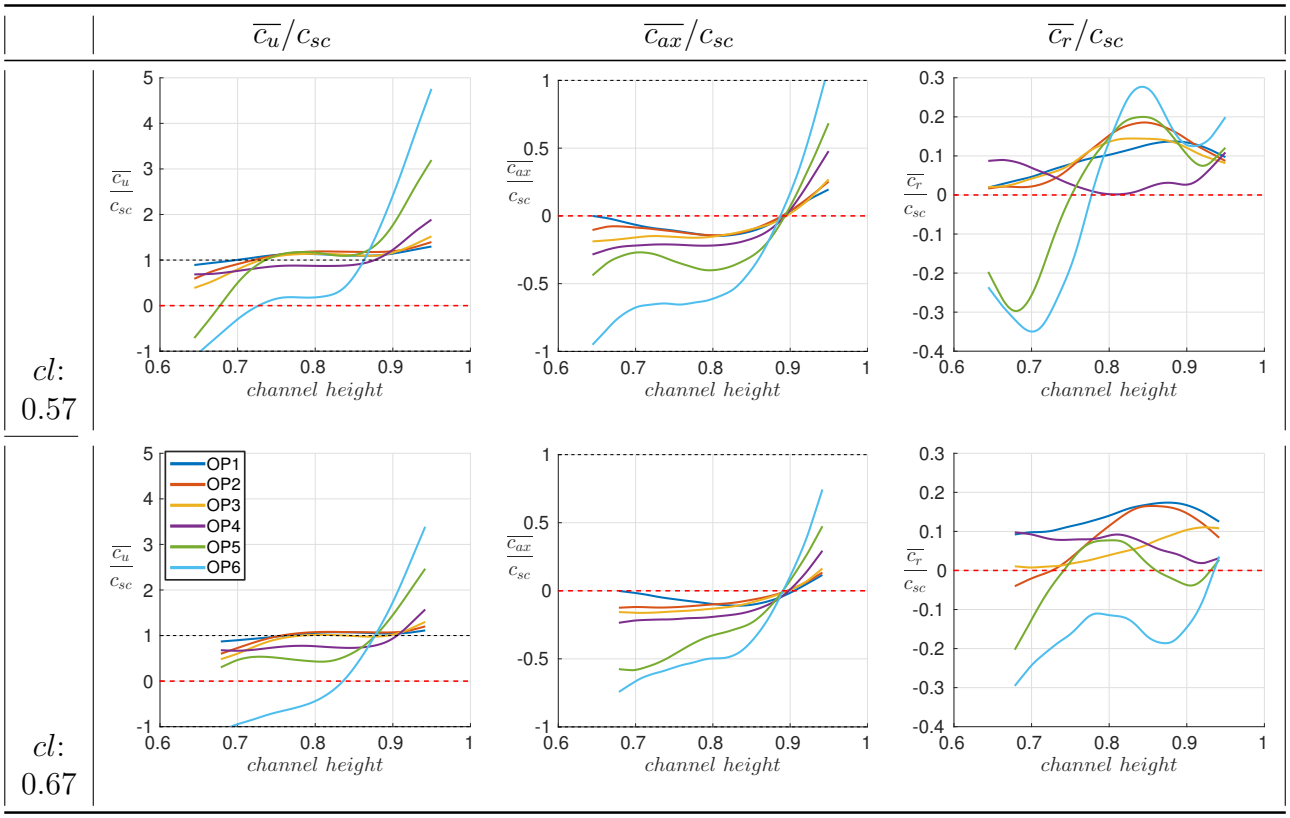

Figure 6.5: Radial profiles for different velocity components at different θ.

with $ch > 0.85$, the influence of the OP becomes clearly visible. The higher the pressure head, the higher the circumferential velocity at the outer rim, with being strictly sorted according to their corresponding volume flow. Although magnitude is nearly one order lower than the one of $\overline{c_u}$, regarding tendency and sequence, the axial velocity profiles look similar to the circumferential ones. Staying quite constant for a wide spread, they increase steeply around $ch = 0.85$ for all OPs. The previous stated stable position of the zero-crossing now becomes more obvious when regarding c_{ax}. As expected, the radial component c_r only plays a minor role, however they are not be neglected completely. For OP 1-4, centrifugal forces are dominating, pushing the fluid outwards against the outer side channel wall (nearly all values are positive) up to a peak around $ch = 0.85$, where they start to decelerating again. This is different for PL (OP 5&6), where negative, or sign-switches are observable for small ($ch < 0.75$). This corresponds to the flow patterns in Figure 6.3, which show back-flow and vortices.

Note: As the machine extends radially, regarding continuity of the circulation mass flow, it would be more convenient (especially for the axial velocity component) to normalize the radial extend with an area proportional to r^2, thus the ratio of inner area to maximum area (A_r/A_{max}). Therefore $ch = 0.8$ would mark the point where the axial flow cross sections on each side are equal. However, as the side channel is rather distant to the rotating axe, differences are small (the point of cross section equilibrium($A_r/A_{max} = 0.5$) is at $ch = 0.82$). For the sake of comprehensibility, it was therefore decided to take the linear normalization.

6.3 Circumferential Profiles

To understand the development of the flow *along the side channel*, all three velocity components are extracted separately along the circumference for all six OPs at two radial positions ($ch = 0.8, 0.9$) as shown in Figure 6.6.

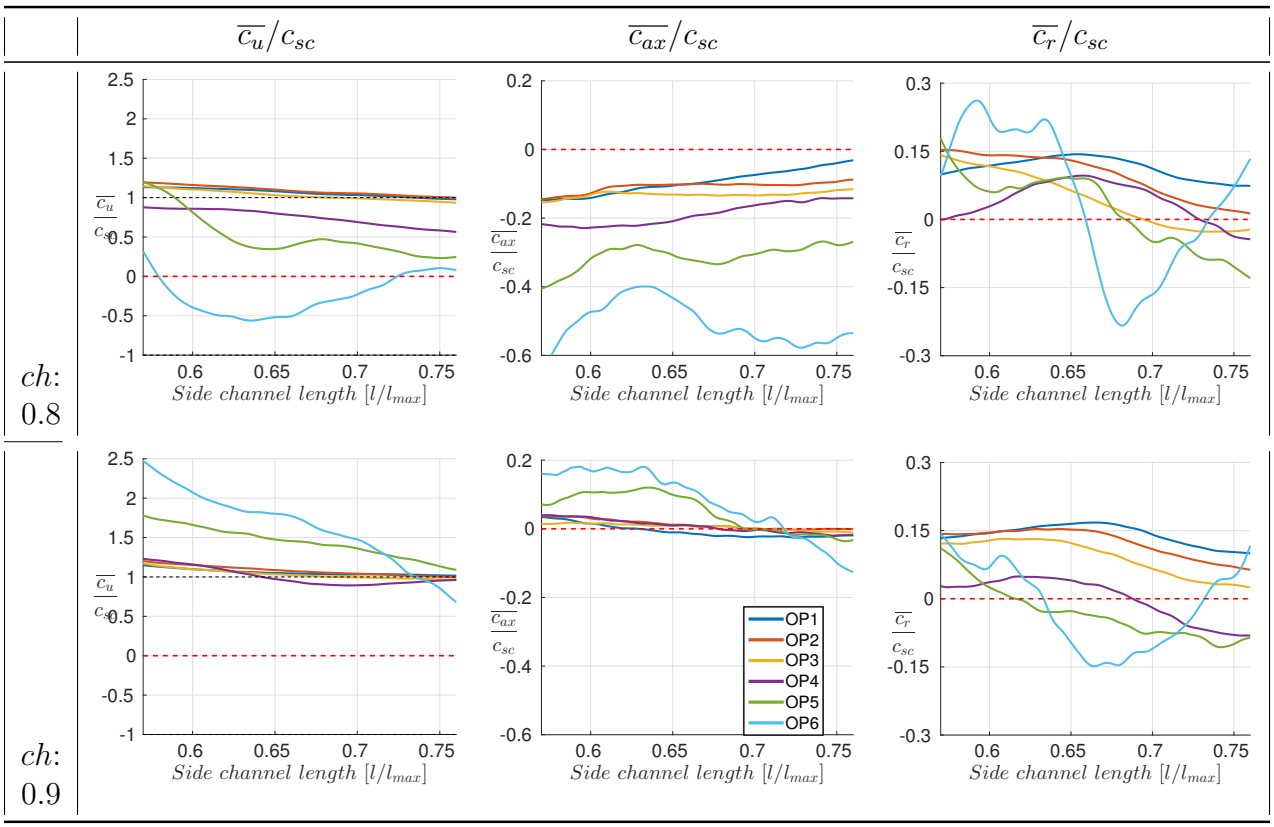

Figure 6.6: Circumferential flow development along the side channel for different radii.

Besides in part load mode, once normalized with c_{sc}, the velocity profiles of $\overline{c_u}$ tend to become similar. All have a slight tendency to decrease along the side channel towards the outlet (in PL with a superimposed fluctuation), while the axial velocities have the reverse tendency (Note again, that the magnitude of $\overline{c_{ax}}$ is nearly one order lower than the one of $\overline{c_u}$ for OPs 1-4, while similar in PL). For smaller radii, the axial component is sorted in monotonic order. For $ch = 0.9$, OPs 1-4 show not only the same trend, but are also around $\overline{c_u}/c_{sc} = 1$, while the corresponding axial component $\overline{c_{ax}}$ is zero. This shows again, that the circumferential velocity is the dominant component and is independent from the OP for medium and high volume flow, In addition it clarifies that normalizing with c_{sc} minimizes OP influences. The behavior in PL is interesting. As will be shown in the upcoming Section 6.4, the flow can be considered converged (observed long enough to be statistically significant). This means, that the observable fluctuation along θ in PL can be considered locally stable. Accordingly for the axial component $\overline{c_{ax}}$ as well. For $ch = 0.8$, there is a constant backflow with no clearly visible trend. For $ch = 0.9$, which is close to the zero-crossing, there is nearly no significant exchange. Magnitude of the radial component c_r is again lower in comparison. Fluctuations in PL are now also visible at the outer radius. In general it can be observed, that for a wide spread of θ , besides in PL, tendencies are similar for all three components.

6.4 Standard deviation over magnitude σ/μ

The ratio $\sigma/\mu\ (\theta, r, z)$ between the local standard deviation $\sigma(\theta, r, z)$ (Eq.:6.3) and the local magnitude $\mu(\theta, r, z) = |\overline{c}|(\theta, r, z)$ is a good indicator to identify the level of fluctuation within a flow field. The local standard deviation (compare eq. 4.2) is defined as:

$$\sigma\ (\theta, r, z) = \sqrt{\frac{1}{N-1}\sum_{n=1}^{N}[c(\theta, r, z, t_n) - \overline{c}(\theta, r, z)]^2} \tag{6.3}$$

With N being the number of total samples (2771 snapshots) and c being the current snapshot composed out of all three velocity components at time t_n for the local point (θ, r, z). $\overline{c}$ is the local time-averaged velocity (compare eq. 6.2).

Divided by the local magnitude μ, this ratio is shown in Figure 6.7 for all six measured Operating Points in the $2mm$ plane (Note the difference in scaling).

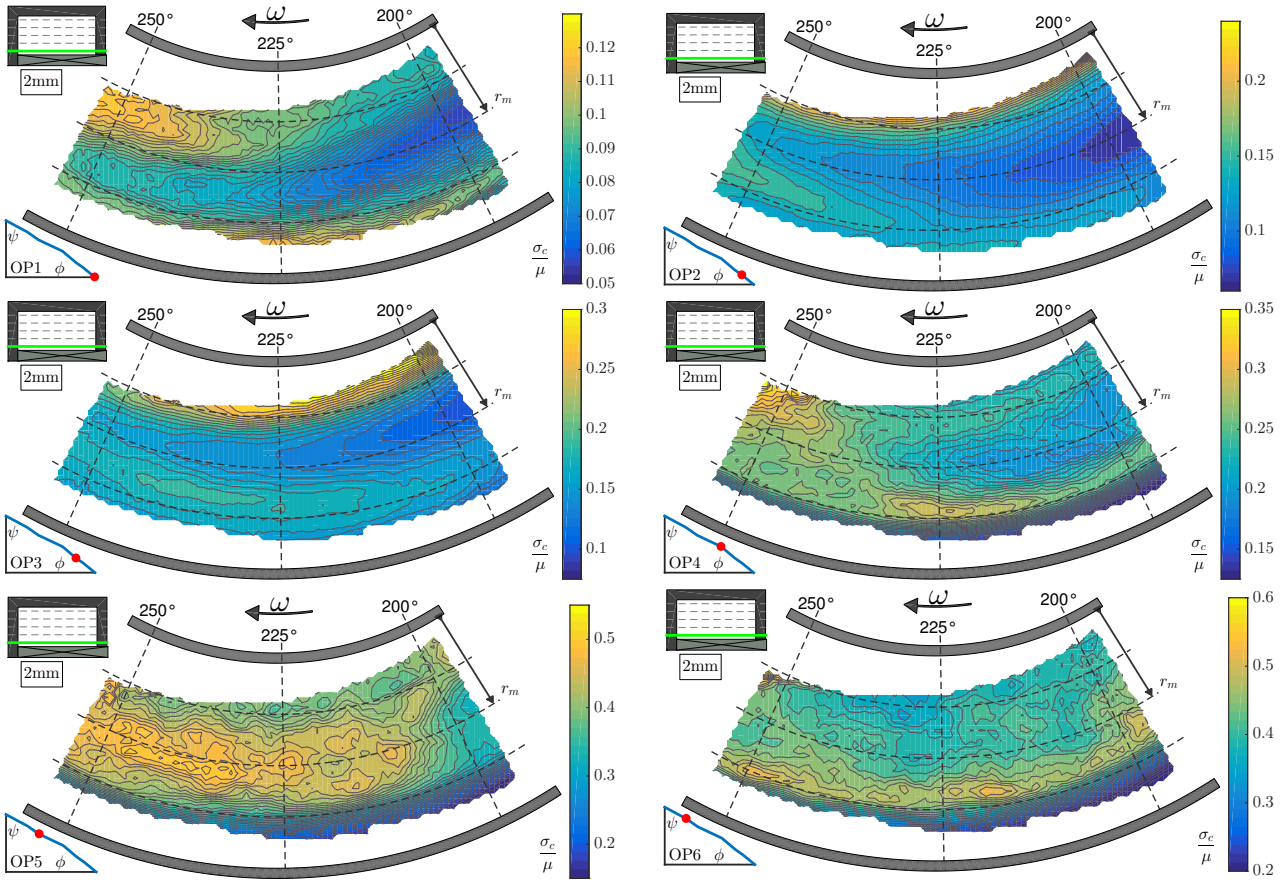

Figure 6.7: Fluctuation level: $\frac{\sigma_c}{\mu}$ OP1 to OP6 for $z = 2mm$.

Regarding magnitude, a tendency is clearly visible: With increasing pressure head, the bandwidth of the ratio is increasing as well (therefore indicating stronger local fluctuations). In general, it can be observed, that for OPs in OL, the ratio is rather strong near the hub, but smaller within the side channel. With increasing pressure head, it becomes stronger within the side channel, but smaller at the outer rim. This is as expected: As could be seen in the previous section (compare Figures 6.5 & 6.6), the dominant component regarding the absolute velocity is

c_u. Therefore the high and stable volume flow through the whole side channel along θ in OL, is the main influence on the ratio. Showing only small fluctuations, but great magnitudes, the ratio is rather low throughout the side channel. Reaching PL, the interaction between impeller and side channel intensifies, while the overall volume flow decreases; the flow is more and more influenced by circulation mass flow. As a result the overall volume flow through the machine has to evade to the area of larger radii, becoming stronger, with higher magnitudes and less fluctuations, leading to the overall smaller ratio.

6.5 Statistical significance

As the flow field is highly dynamic and with a measurement time of only 1.4 s at a frequency of 2000 Hz, it is necessary to assure that all relevant phenomena have been captured without loosing important information. Only then the interpretation of the averaged data is valid. A good estimator to ensure statistical significance, is the convergence of the aforementioned ratio between the local relative standard deviation of the velocity magnitude and local magnitude itself σ/μ (N) as a function of the number of snapshots N.

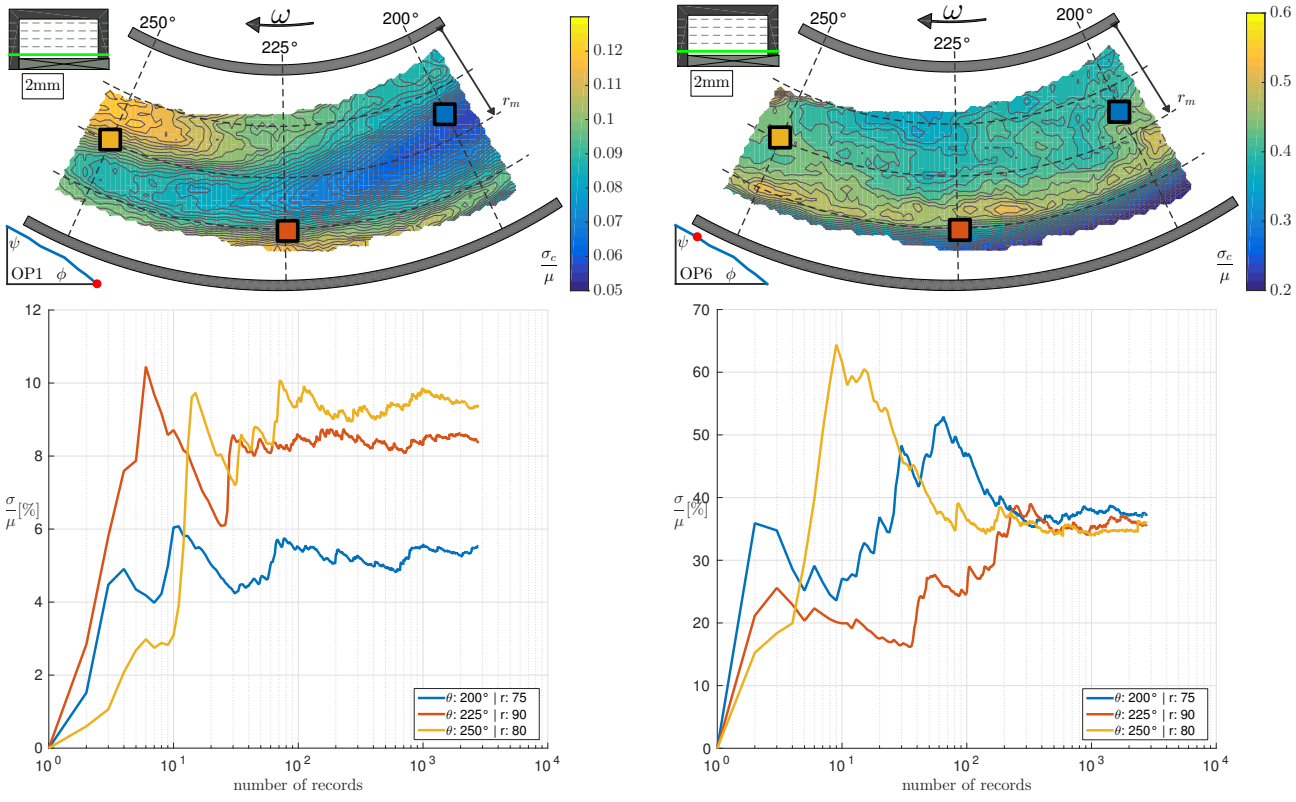

Figure 6.8: Convergence Plots for OP 1&6. Colorcoding as indicated above.

Figure 6.8 shows the resulting convergence plots for three relevant points within the flow field for the two extrem OPs 1&6. Blue: Point near rather low fluctuation. Red: Point near the axial Zero Crossing. Yellow: Point near higher fluctuation. (Note that for reasons of readability, the scale of the contourplot is fitted to each OP itself). To distinguish the differences in between the OPs themself, Figure 6.9 is introduced additionally to show the convergence plots for all OPs at the Zero Crossing and in the Area of High Fluctuation.

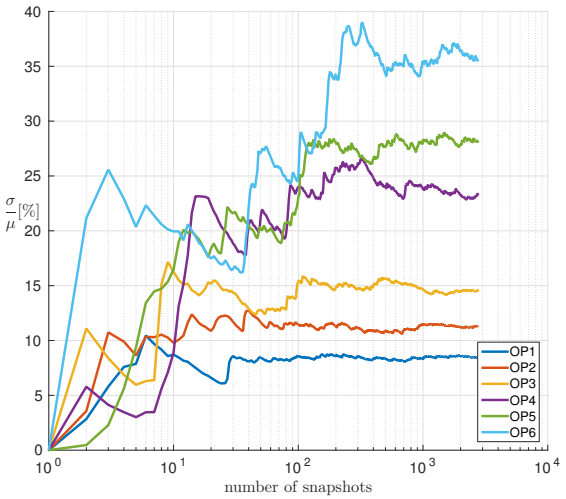

(a) Position of c_{ax} zero crossing at $\theta = 225°$ ( ).

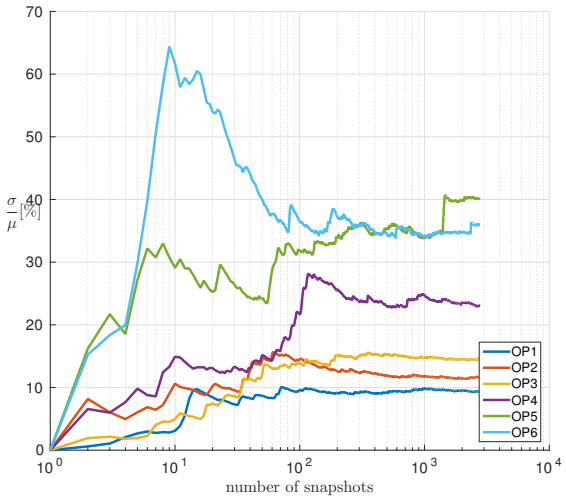

(b) Area of high fluctuation at $\theta = 250°$ ( ).

Figure 6.9: Convergence Plots for different OPs at distinct positions indicated in Figure 6.8.

Overall ratio spreads from around 8% up to 40%, depending on the OP and the local position. It is observable, that in most cases a distinct convergence is achieved after 10^3 Samples (keep in mind, that the abscissa is logarithmic). However, within the area of higher fluctuations, there's a clearly visible step for OP 5 at around N = 1400-1500 and a smaller one for OP 6 around N = 2300 (see Figure 6.9b). In both cases, the step occurred suddenly from an already convergent state and stabilized again very quickly. This could be an indicator for either a periodic, yet very fast state-switching phenomena with a frequency lower than the rather short measurement time would be able to cover, or more likely, a randomly occurring flow phenomenon. Further interpretation would go beyond the scope of this work. Despite the two outlier, all in all it can be stated that albeit the rather short measurement time of only 1.4 s, flow averaging is valid and the observation time was long enough for capturing the relevant phenomena.

6.6 Plane-to-plane comparison of the mean flow fields

As the $2mm$ plane is the most important one regarding the interaction between impeller and side channel, therefore the working principle of the machine, focus of this chapter so far laid on this plane. However, to understand the axial flow development along the height of the side channel, the remaining planes for OP3 are introduced with Figure 6.10.

To compare quantitatively, Figure 6.11 shows the flow development along $cl = 0.67$ as well as $ch = 0.9$. The common line for all profiles ($ch = 0.9,\ cl = 0.67$) is marked as a dashed blue line.

Ultimately, it is possible to combine all planes and therefore being able to clarify the flow within the (r, z)-plane, as well as in the (θ, z)-plane; this is introduced with Figure 6.12 (recall Figure 3.9a in comparison).

Streamlines are composed out of $c_r \& c_{ax}$, while the the contour is showing c_u normalize by c_{sc}. In addition, a dotted black line shows the ratio $c_u/c_{ax} = 1$. The common line $ch = 0.9,\ cl = 0.67$ is marked by a blue dashed line, while the five measurement planes $2 - 18mm$ are indicated in the background by green dashed lines. Now the circulation mass flow through the side channel

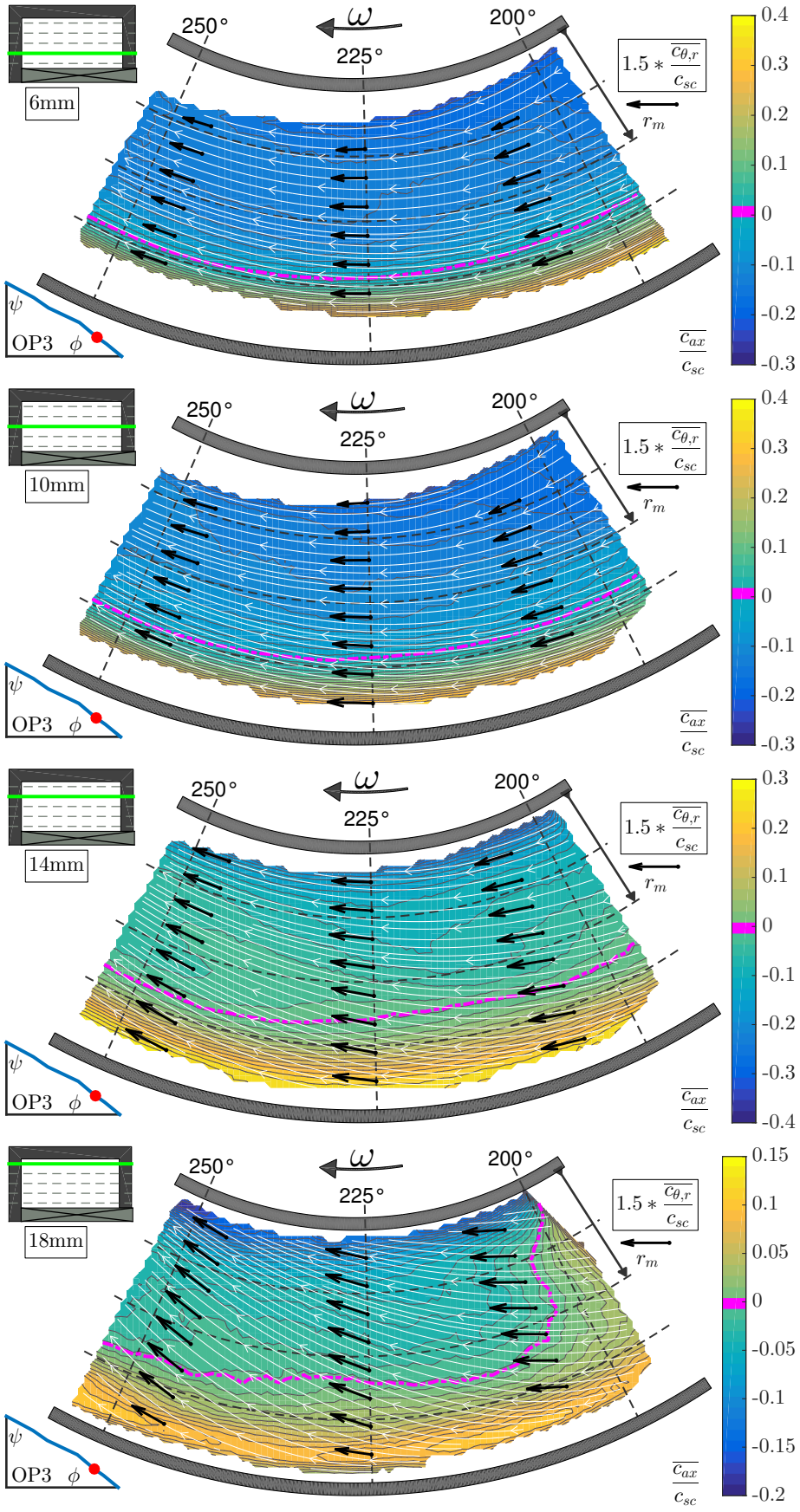

Figure 6.10: Mean flow fields $\overline{c_i}(\theta, r, z)$ for OP3 with $z = 6 - 18mm$.

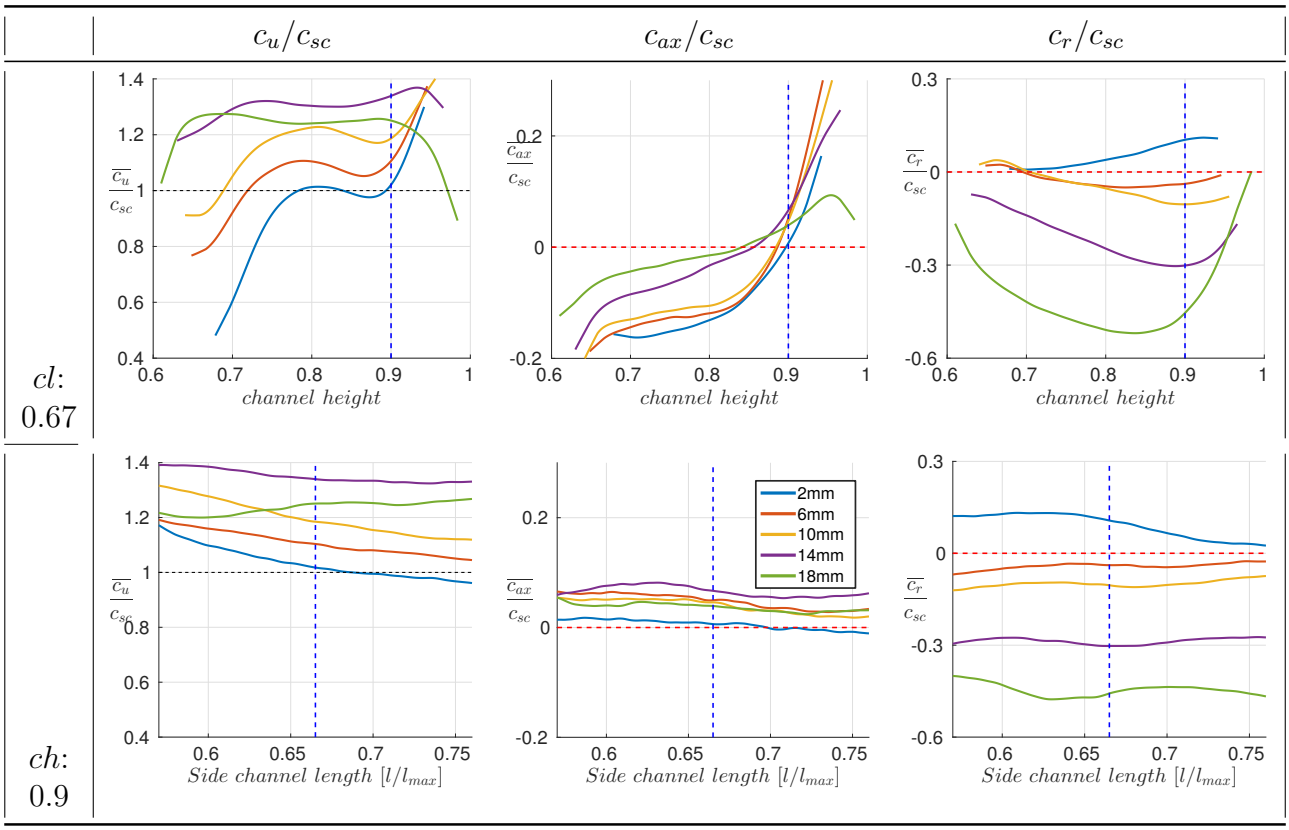

Figure 6.11: Velocity profiles along $cl = 0.67$ as well as $ch = 0.9$. The common line of the profiles, as well as with Figures 6.12 & 6.13 is dashed in blue.

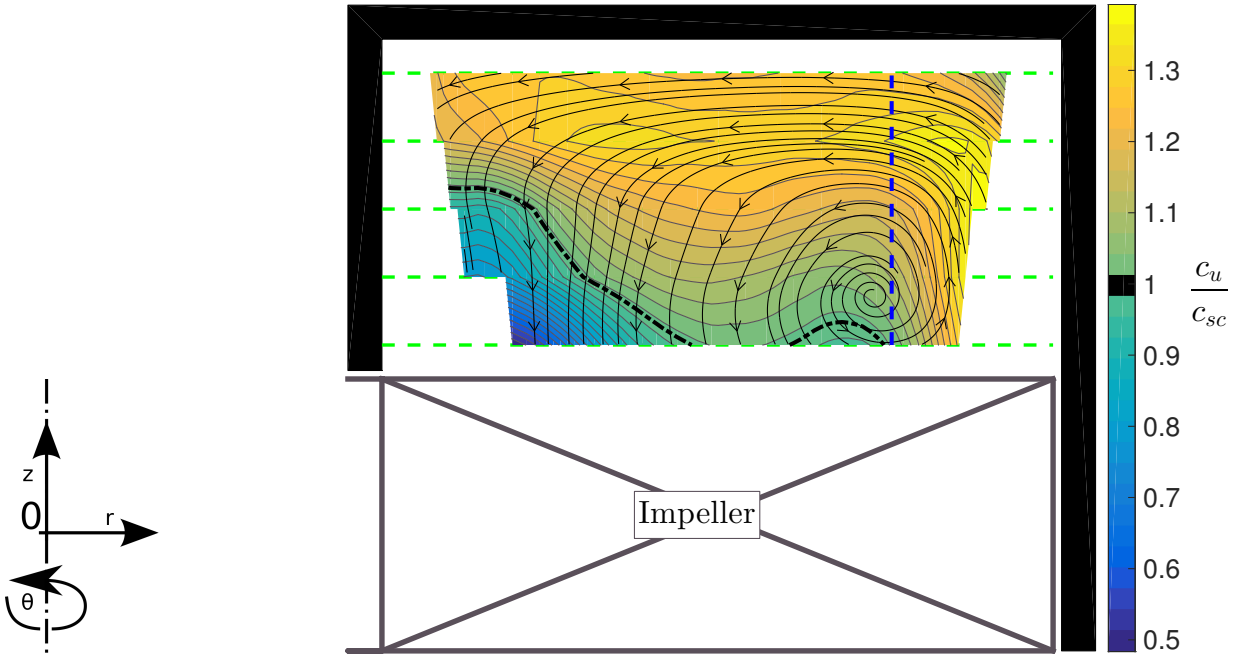

Figure 6.12: (r, z)-plane for $cl = 0.67$; Position of the measurement planes indicated as dashed green lines; The common line with Figure 6.11 & Figure 6.13 is dashed in blue.

can be described in detail: After leaving the impeller at the outer radius (right-hand side of the zero- crossing), the fluid accelerates in axial direction at first (c_{ax}), but decelerates again, when approaching the upper limit of the side channel. The same effect can be observed for the circumferential component (c_u) as well. Due to the upper wall, axial velocity is converted into radial velocity for the necessary back-flow towards the hub. Here the radial component is converted into axial flow again, where it finally enters the impeller again. The helical structure of the flow can be adumbrated by comparing the rather straight streamlines in lower planes compared to the stronger bended ones for higher planes in Figure 6.10.

Note that, the circumferential resolution of the data in the (θ, r)-plane is $1mm$, while being $4mm$ in axial direction (z). Therefore these, as well as all following contour plots within the z-plane are generated by a simple linear interpolation instead of a more sophisticated one, to circumvent false interpretation.

Flow development along θ at $ch = 0.9$ is presented with Figure 6.13 (compare 2.4).

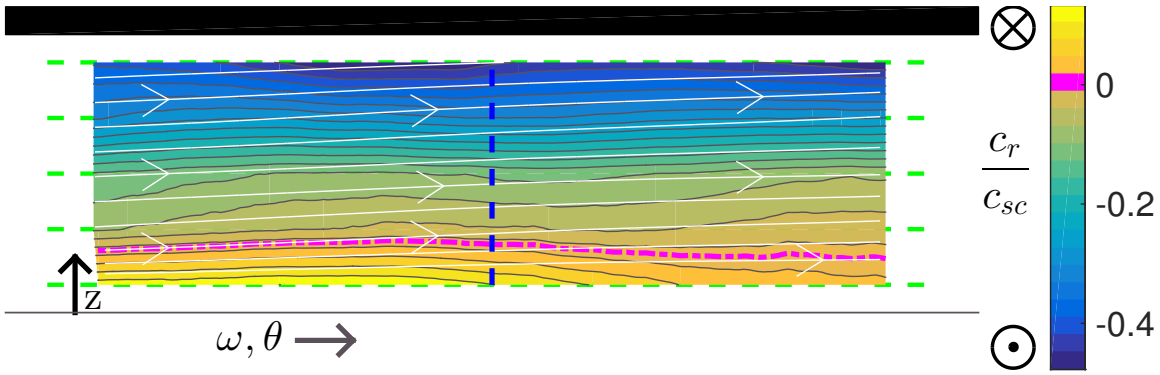

Figure 6.13: (θ, z)-plane for $ch = 0.9$; Position of the measurement planes indicated as dashed green lines; The common line with Figure 6.11 & Figure 6.12 is dashed in blue.

Streamlines visualize c_u&c_{ax}, while the contour represents c_r normalized by c_{sc}. A dashed magenta line shows the zero-crossing, warm colors go into the plane, cool ones towards the observer. Basically two things are visible: While the dominating circumferential component is decreasing in all planes when getting closer to the outlet (besides directly under the casing ($z = 18mm$)), axial and radial velocities are more or less stable. This can be interpreted in such a way that the helical circulation flow remains rather stable (c_u & c_{ax}), while the circumferential component (c_u) works against the pressure gradient of the machine and has to decrease. Therefore the circumferential development of the helical flow structure is not constant along the side channel, but rather shows a compression. This leads to the assumption, that the interaction between side channel and impeller is not constant along the circumference, but depends on θ, therefore the distance from and to in- and outlet.

In conclusion, average flow field analysis already shows that a distinct difference between primary (total volume flow rate through the side channel) and circular flow (circulation volume flow rate) is obviously observable and quantifiable. Clear differences all along the characteristic curve of the machine are visible. However, time-averaging smooths out dynamic phenomena by definition. Therefore, to investigate the interaction between impeller and side channel as the driving force behind momentum exchange furthermore, more advanced approaches have to be pursued.

Chapter 7

Results: PIV - Phase average ⟨PA⟩

As already explained, the SPIV measurements were supported by common integral value acquisition, such as torque and angular measurements. By making use of the angular measurements it is possible to switch from an absolute to a blade related reference frame as for each PIV snapshot of the flow situation exists a recorded angular position. Using this information enables to do a phase averaging for a given impeller position (and therefore blade position). Results are presented in the same manner as in chapter 6.

7.1 Statistical significance

Having such a small pool of data, statistical significance is of great importance. Figure 7.1 shows the convergence plots in the same manner, as for the time averaged case (compare Section 6.5).

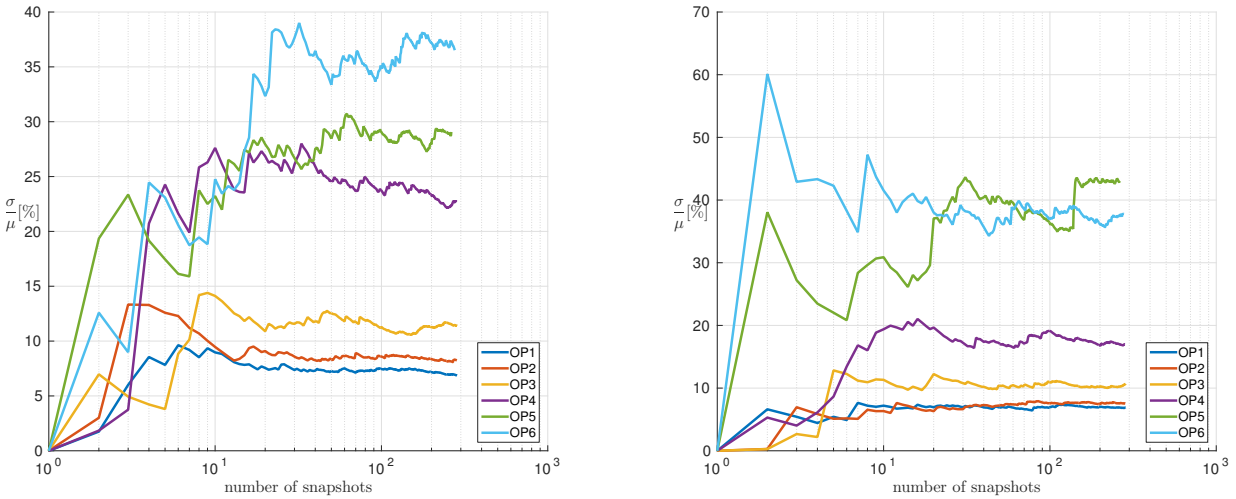

(a) Position of c_{ax} zero crossing at $\theta = 225°$ ( ). (b) Area of high fluctuation at $\theta = 250°$ ( ).

Figure 7.1: Phase Averaged Convergence Plots for different OPs at two destinct positions (compare Figures 6.8 & 6.9).

For both positions, convergence is achieved after only around 40 Samples for OPs 1-4. However, in strong PL convergence is not reached completely, but is regarded as being sufficient enough,

as the gradient is quite small. The difference in the number of necessary snapshots compared to the simple time averaged case in chapter 6 is remarkable. While in the last-mentioned case more than 1000 Samples were necessary to reach a converged state, in case of phase averaging, only 40 Samples are sufficient. This can be explained by the flow characteristic itself: For the simple time averaged case nearly all possible blade angular positions were present over the whole measurement regime. This results in strongly varying flow fields. In case of phase averaging, there's only one distinct blade position. Therefore flow fields are more similar and the ratio should converge significantly faster, as can be observed in the present case. It is remarkable, that the same unusual behavior as in the $\overline{TA}$ case can be observed for OP5 in the area of high fluctuation again: The ratio seems already converged up to 140 samples, when suddenly changing state again. The phenomena occurs at the same time as in the $\overline{TA}$ case, as the measurements were time-resolved, therefore the time stamp of the snapshot in the $\langle PA \rangle$ case is the time stamp of the $\overline{TA}$ case divided by the number of phase angles ($1400/10 = 140$). An in-depth examination would have been beyond the scope of this work, however the reason could be identified as a strong axial vortex being transported circumferentially through the side channel. This behavior wasn't observed again and the data in general considered statistical significant.

7.2 Phase Averaged Flow Fields $\langle c_i \rangle(\theta, r, z, pa)$

Phase averaged results enable to uncover the influence of the impeller. Figures 7.2 & 7.3 show all three phase averaged mean flow fields $\langle c_{u,r,ax} \rangle$ for all six measured OPs in the $2mm$ plane normalized by the mean side channel velocity c_{sc}. Flow fields are presented in the same manner as already described in chapter 6. In addition, the underlying impeller of the current phase is drawn true to scale. The phase averaged mean flow field $\langle c_i \rangle(\theta, r, z, pa)$ is calculated according to:

$$\langle c_i \rangle(\theta, r, z, pa) = \frac{1}{N_{pa}} \sum_{n=1}^{N_{pa}} c_i(\theta, r, z, t_{pa} + n * \frac{1}{BPF}) \tag{7.1}$$

With pa being the desired phase angle out of the previously explained 10 available (here: pa=4 is used, as this shows three complete blade channels). N_{pa} is the total number of available snapshots per phase (~ 270 Samples). c_i is the current snap shot, with t_{pa} being the first occurring time stamp of the chosen phase angle and BPF being the blade passing frequency of 200 Hz.

Similar to the mean flow fields (see chapter 6.1), the in-plane components for OP 1-4 smoothly follow the contour of the side channel, with a difference in curvature according to their volume flow. However, in phase-averaging it can be observed, that with bigger radii and increasing pressure head the smooth curvature starts to become more wave-like. For OP 5&6 the structure of the flow suddenly changes a lot, showing backflow and vortices. The axial component reveals obvious impeller related structures for the first time: Besides in OL (where there is also flow into the side channel near the hub), all OPs show a flow into the side channel only above the mean radius (r_m) with a repeating pattern clearly related to the underlying blades. The zero-crossing itself shows an interesting behavior: If one recalls the time averaged velocity fields of Section 6.1, they showed a similar zero-crossing position for all OPs, suggesting also similar phase averaged behavior. However, it is visible for all OPs, that this is not the case: While for OP 1-3 the zero crossing shows a strong wave-like structure, for OP 4-6 this is smoothed with only very

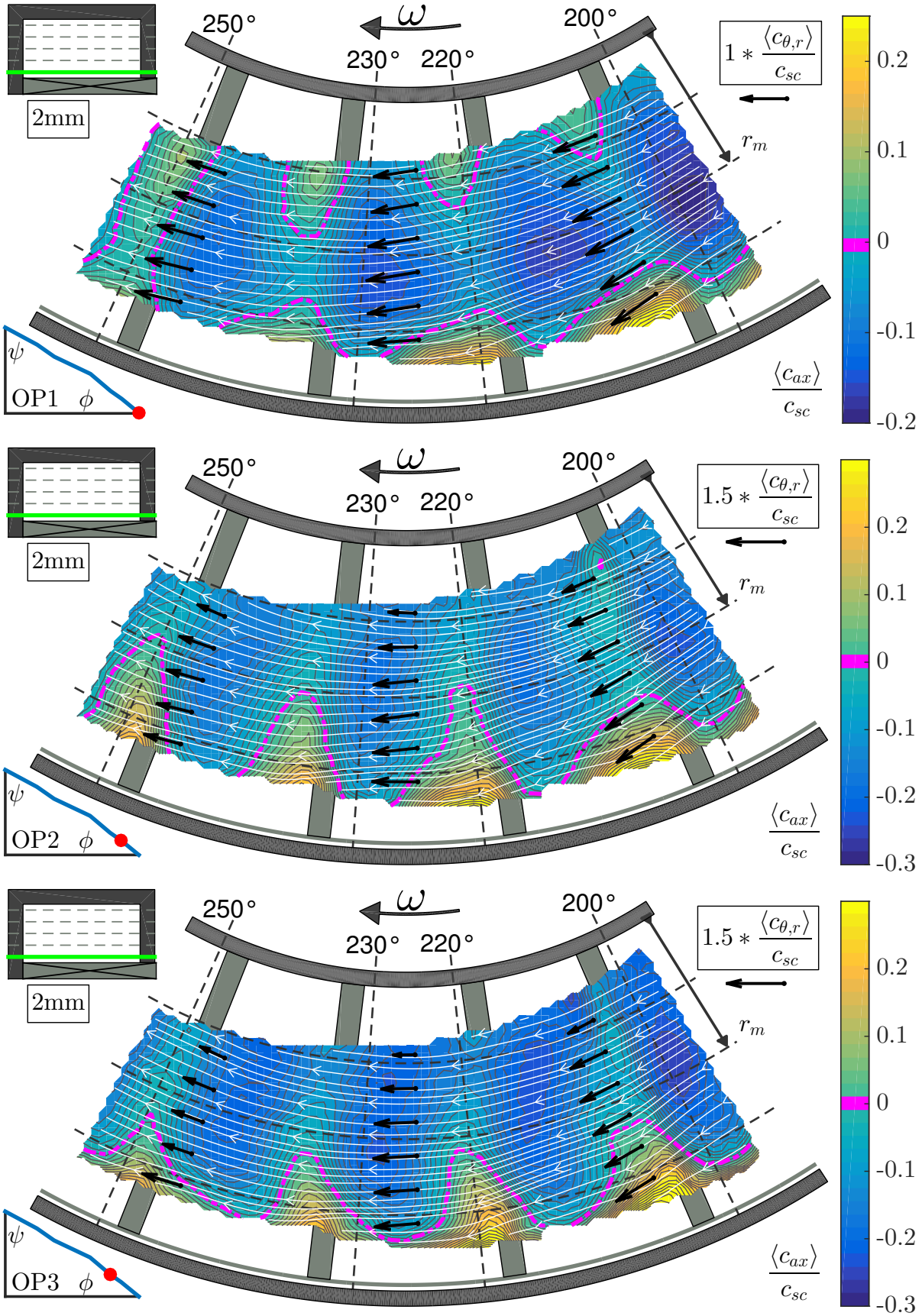

Figure 7.2: Phase averaged mean flow fields $\langle c_i \rangle(\theta, r, 2mm, 4)$: OP1 to OP3.

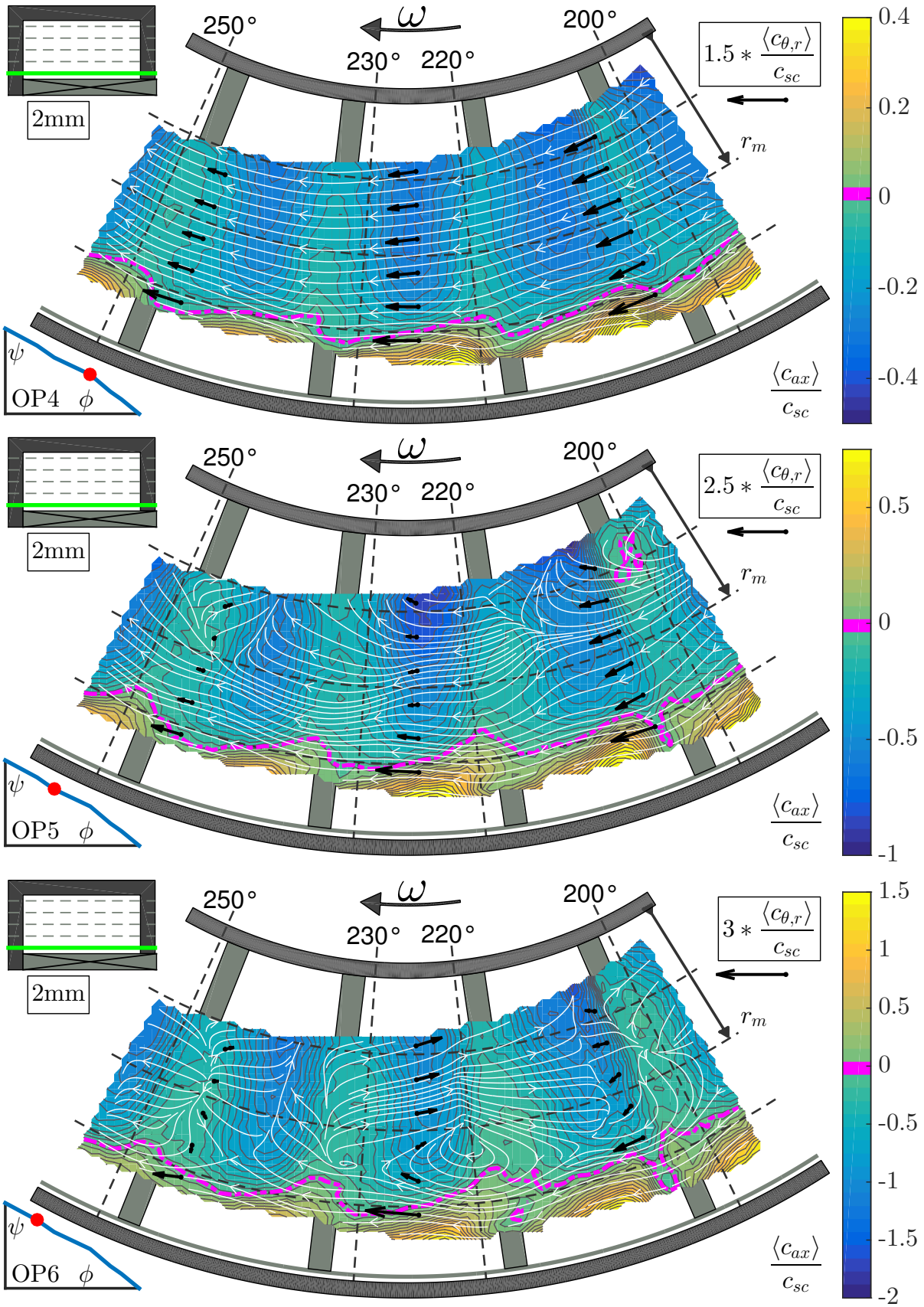

Figure 7.3: Phase averaged mean flow fields $\langle c_i \rangle(\theta, r, 2mm, 4)$: OP4 to OP6.

small fluctuations. It is remarkable, that despite the very different velocity patterns per OP in $\langle PA \rangle$, nonetheless, the overall zero crossing in $\overline{TA}$ is stable. It can be stated, that the phase averaged flow fields give a significantly deeper insight into the flow situation in game compared to the simple time averaged approach. They reveal very complex flow patterns generated by the varying interaction between impeller and side channel according to the operating point.

7.3 Radial Profiles

At first glance, the phase averaged radial profiles shown in Figure 7.4 are quite similar to the time averaged ones in Figure 6.5.

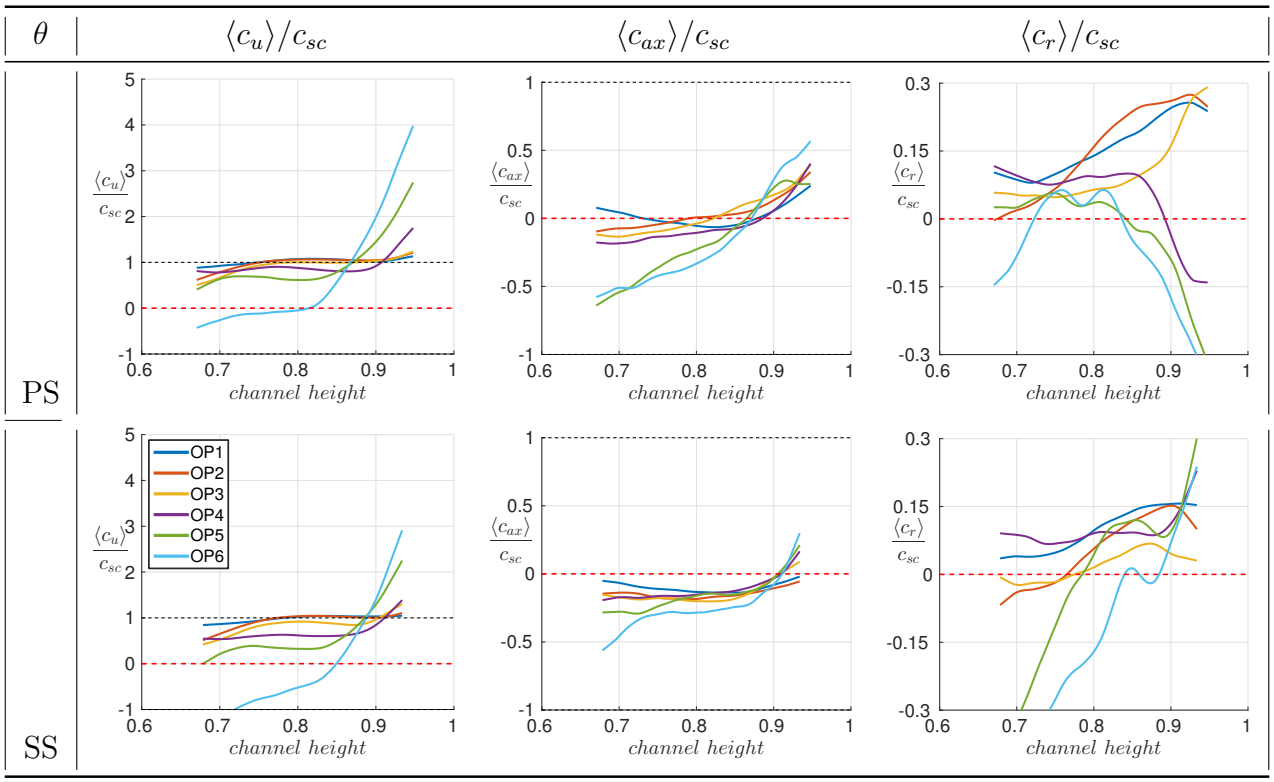

Figure 7.4: Phase averaged radial profiles for different velocity components for pressure (PS) and suction side (SS) of the same blade channel at $\theta = 225°$.

However, as due to phase averaging the impeller position is known, the radial profiles were extracted at two different characteristic θ above the same blade channel (keep in mind, that the measurement plane is $2mm$ *above* the impeller). The pressure side (PS) of the blade is represented by $\theta = 220°$, while $\theta = 230°$ is on the suction side (SS). Comparison is done to the $\overline{TA}$ case for $\theta = 225°(cl = 0.67)$. Regarding $\langle c_u \rangle$, both profiles are similar to the $\overline{TA}$ one regarding trends, order, magnitude and zero-crossing. $\langle c_{ax} \rangle$ still looks kind of similar to the $\overline{TA}$ one, however more noisy. This can be explained by the method of $\langle PA \rangle$ itself: While in the $\langle PA \rangle$ case only $N_{PA} = 271$ snapshots at the very same position are combined, in case of $\overline{TA}$ it's $N = 2771$ snapshots at arbitrary positions. However, as only in 10% of all $\overline{TA}$ cases a blade (and therefore its direct influence) is underneath the measurement plane, profiles should be similar within margins. $\langle c_r \rangle$ is even harder to interpret: Both profiles show only a minor

similarity to the $\overline{TA}$ case, while strong fluctuations are visible. However, velocities are now within the same order of magnitude as $\langle c_{ax} \rangle$, indicating that the impeller has also an influence in radial direction.

7.4 Circumferential Profiles

In contrast to the radial profiles, the circumferential $\langle PA \rangle$ profiles in Figure 7.5 differ strongly from the $\overline{TA}$ ones in Figure 6.6.

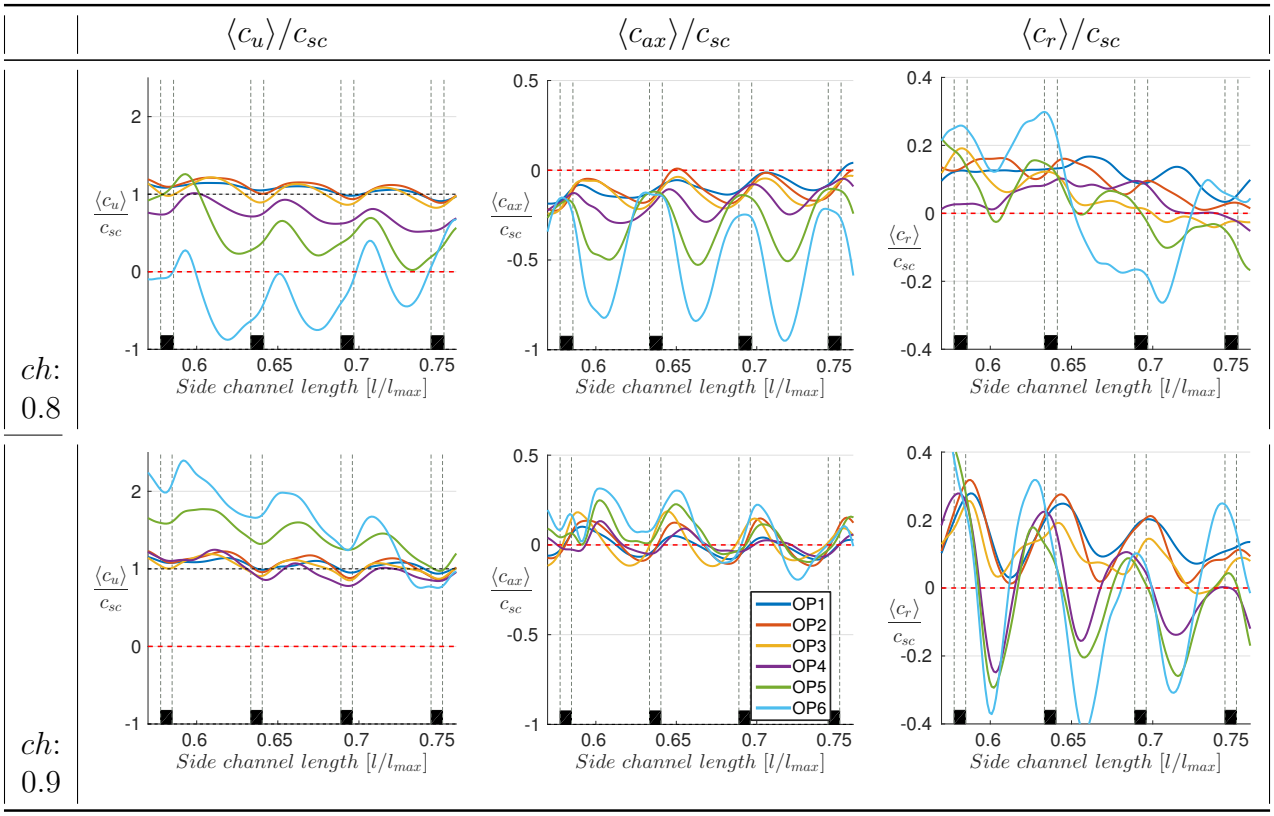

Figure 7.5: Phase averaged circumferential flow development along the side channel for different radii (side channel length). Blade positions indicated by black rectangles.

While the overall tendency are similar to those described for the $\overline{TA}$ case, now the benefit of phase averaged analyzes reveals: As in the $\langle PA \rangle$ case the blade position can be drawn (black rectangles), their influence on the flow can be clearly seen for all velocity components and all OPs. Distinct oscillations are visible, some even with a tendency to a blade harmonic behavior. Amplitudes are getting stronger while going from OL to PL. The influence of the OP to the flow field can be seen by comparing the position of local maxima: For $\langle c_{ax} \rangle$ at $ch = 0.8$ in OL (dark blue), the local maximum can be observed at the pressure side of the blade. In strong PL (cyan) this maxima shifts against the direction of rotation towards the suction side. The same is true for $\langle c_u \rangle$, having the same shift of about 4°. Oscillations for $\langle c_r \rangle$ are smeared, however showing blade related tendencies as well. Position of the local maxima seems to be in phase with $\langle c_u \rangle$. Regarding $ch = 0.9$ things change: $\langle c_{ax} \rangle$ and $\langle c_u \rangle$ still show a OP dependency, however the positions of the maxima changed. $\langle c_r \rangle$ now seems to be in anti-phase with $\langle c_{ax} \rangle$ when in PL, but in phase for OPs in OL.

In conclusion, blade dependencies in all three components are clearly visible as the period of nearly all oscillations fits to the blade spacing. The components seem to be connected to each other with distinct phase shifts (regarding the oscillation, not θ). However, clear identification is difficult, as oscillations are not explicit harmonic. Furthermore, due to strongly varying amplitudes, differences in between OPs are difficult to identify as well.

7.5 Plane-to-plane comparison

The extracted velocity component profiles are shown in Figure 7.6.

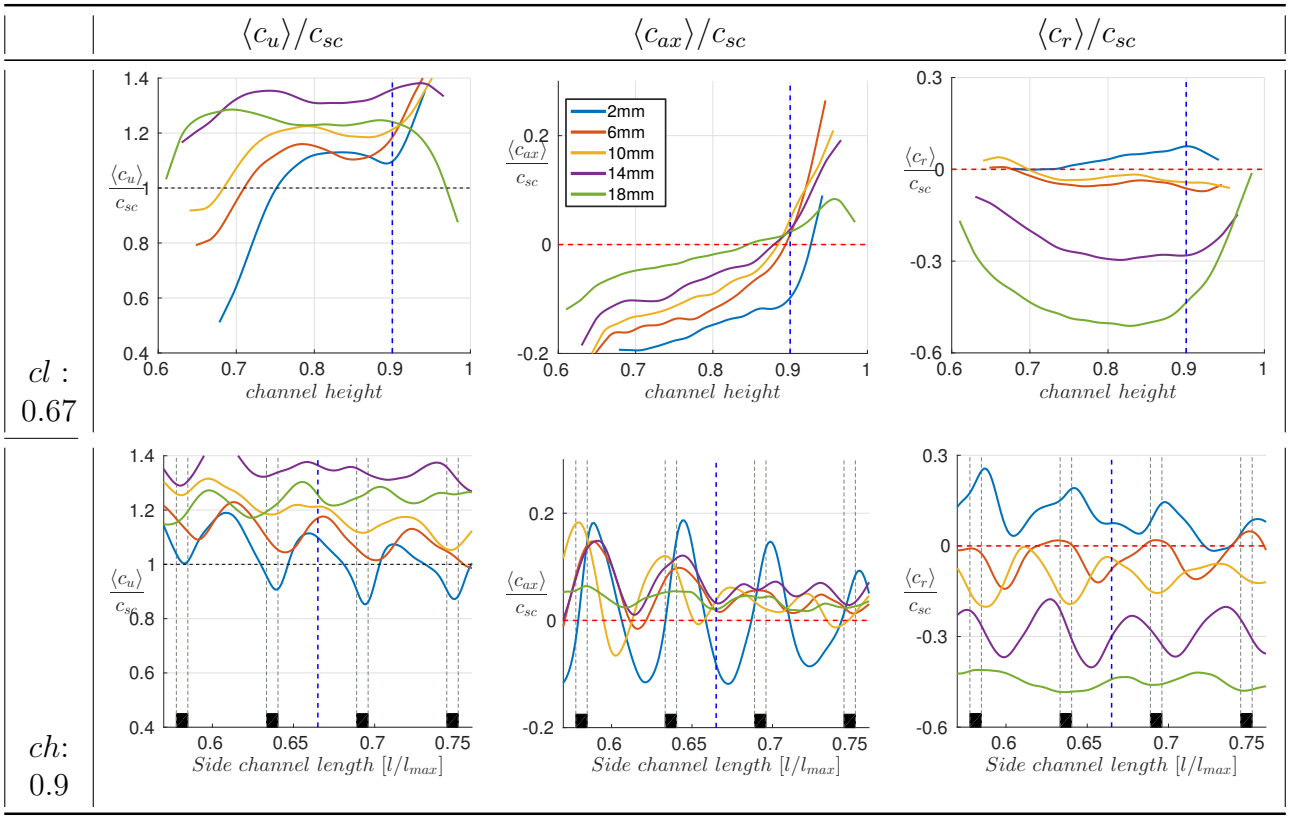

Figure 7.6: Profiles for all three velocity components along $cl = 0.67$ as well as $ch = 0.9$ for different planes. The common line of the profiles, as well as with Figures 7.7 & 7.8 is dashed in blue.

They show the same behavior as described before: The radial extent along $\theta = 225°(cl = 0.67)$ is similar to the $\overline{TA}$, but due to the smaller data pool a little more noisy. This is fortified by Figure 7.7, which shows the same tendency: it is also similar to the $\overline{TA}$ one, but more noisy as well. Circumferential flow development along θ follows the same trend as in the $\overline{TA}$ case, but with the above discussed clearly visible blade-related oscillations. This is especially remarkable when taking a look at $\langle c_{ax} \rangle$ at $ch = 0.9$: In the $\overline{TA}$ case, the $2mm$ plane seemed to have the lowest magnitude, while the $14mm$ plane had the strongest one. $\langle PA \rangle$ now reveals that there are considerable oscillations superimposing the mean value, with the $2mm$ plane now having the strongest magnitude. As it was already visible in the $\overline{TA}$ case, the magnitude of c_r increases with increasing distance to the impeller, being within the same order of magnitude as $\langle c_{ax} \rangle$.

Figure 7.8 is introduced to clarify this further: While the streamlines as a combination of c_u & c_{ax} do not obviously reveal strong differences compared to $\overline{TA}$, the radial component now shows significant blade related structures, giving a first impression of a complex flow behavior.

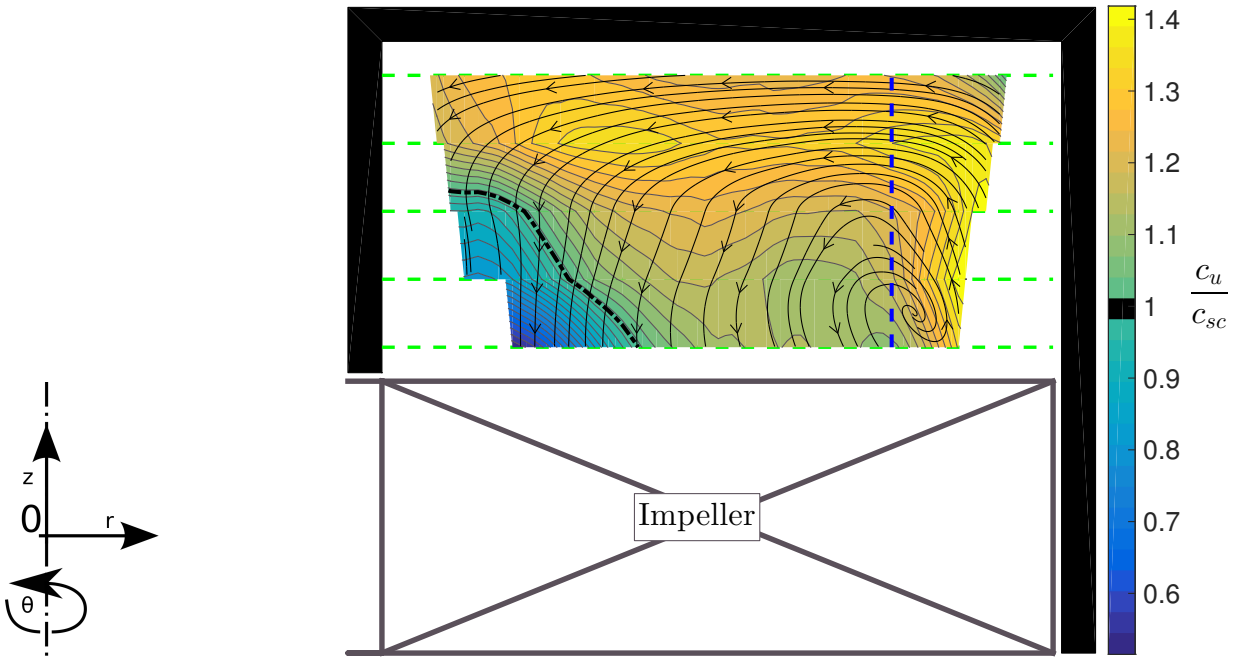

Figure 7.7: (r, ax)-plane for $cl = 0.67$. Position of the measurement planes indicated as dashed green lines. The common line with Figure 7.6 & Figure 7.8 is dashed in blue.

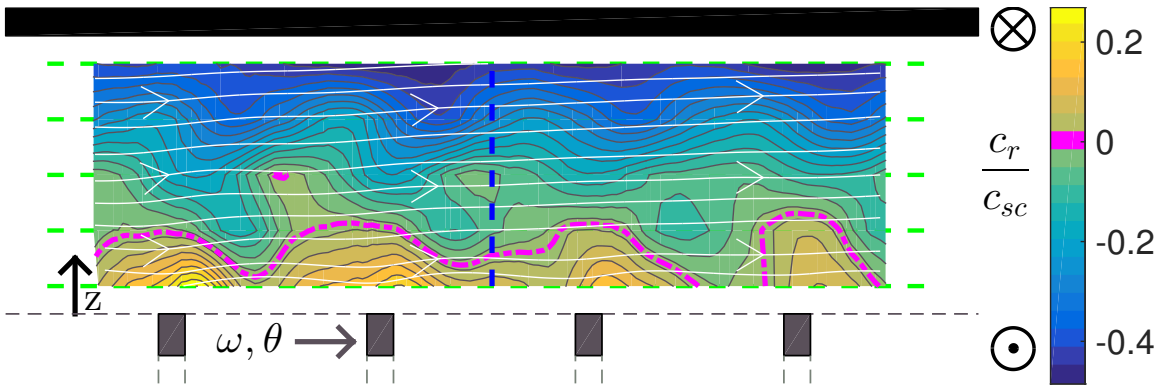

Figure 7.8: (θ, z)-plane for $ch = 0.9$. Position of the measurement planes indicated as dashed green lines. The common line with Figure 7.6 & Figure 7.7 is dashed in blue.

With Figure 7.9 the $\langle PA \rangle$ axial development of the flow is introduced. Compared to Figure 6.10, differences between the $\langle PA \rangle$ and $\overline{TA}$ flow fields are again quite minimal. However, impeller related structures of the axial component can be observed even up to the highest plane ($18mm$).

In conclusion, phase average flow field analyzes helps to further illustrate the complex interaction between impeller and side channel. The influence of the impeller on all three velocity components clearly reveals. When comparing the magnitude of the mean flow ($\overline{TA}$) with the magnitude of the blade (therefore impeller) related oscillations ($\langle PA \rangle$), it becomes obvious, that they are still an order of magnitude higher. This suggest to further decompose the flow field, to separate between impeller related and volume flow rate related components.

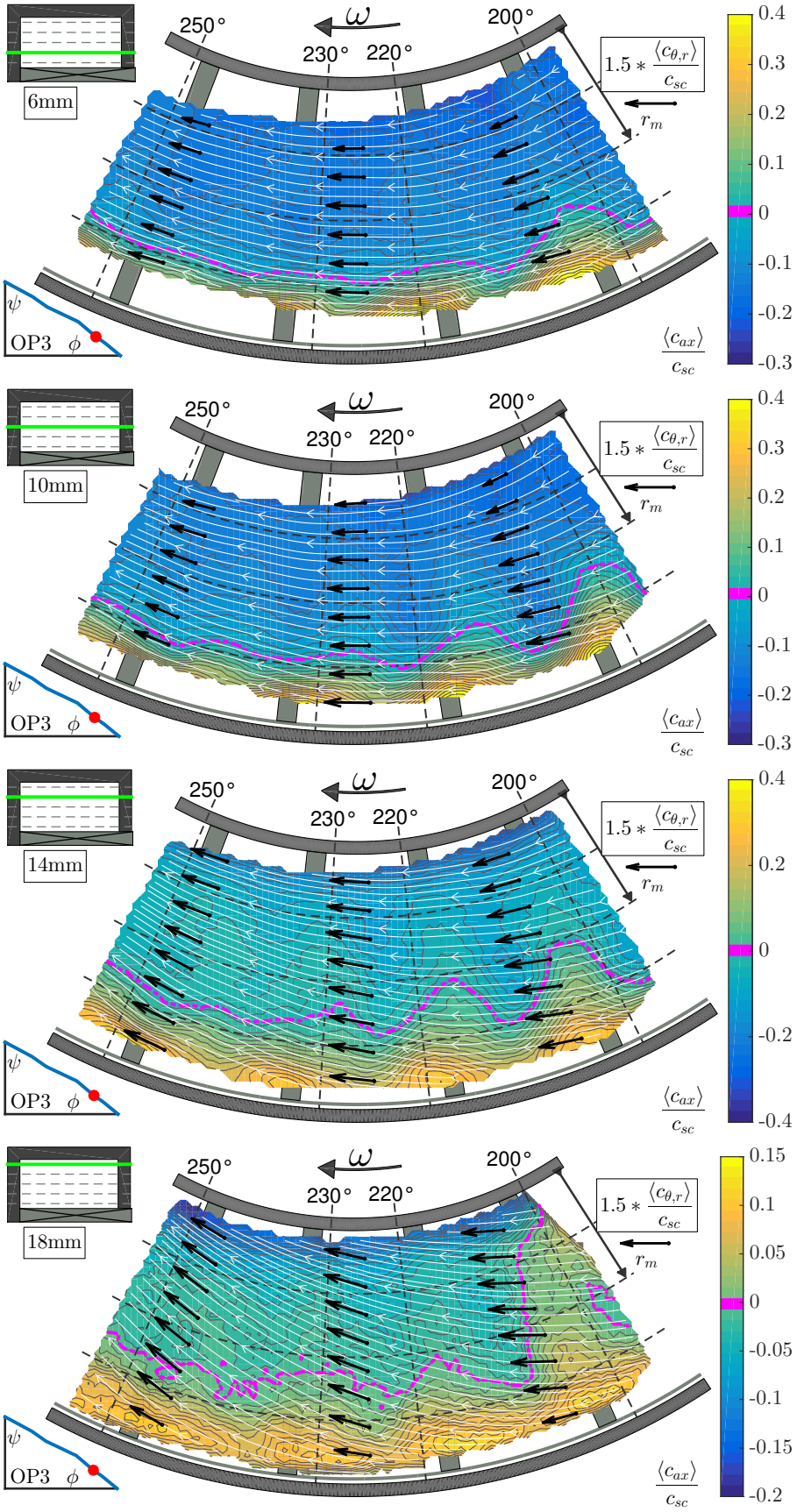

Figure 7.9: Phase averaged flow fields $\langle c_i \rangle(\theta, r, z, 4)$ for OP3 with $z = 6 - 18mm$.

Chapter 8

Results: PIV - Combined Approach: Periodic Dynamic $\widetilde{\text{PD}}$

The previous chapters helped to clarify the flow development within the side channel of the RFP. $\overline{TA}$ and $\langle PA \rangle$ already give a comprehensive insight and enable to compare quantitatively. However, due to its highly three-dimensional complexity, analytical flow description is not easy to be done. Especially the cause-effect relation between impeller and side channel flow is not yet identified in a convenient way. To overcome these shortcomings, this work proposes to make use of a further decomposition:

Hussain and Reynolds [63] and later on Laschka [64] decomposed all flow variables of an arbitrary instantaneous flow field (c_i) into three parts: a steady mean component ($\overline{c_i}$), a periodic perturbation ($\widetilde{c_i}$) and stochastic fluctuation (c_i'):

$$c_i(\theta, r, z, t) = \overline{c_i}(\theta, r, z) + \widetilde{c_i}(\theta, r, z, t) + c_i'(\theta, r, z, t) \tag{8.1}$$

In case of fluid machinery, this triple decomposition can be interpreted as follows:

The quasi steady mean flow ($\overline{c_i}$) is the primary flow. It is the $\overline{TA}$ results from Chapter 6. In case of a RFPs it is directly connected to the primary mass flow (transport) trough the machine.

The periodic dynamic component (periodic perturbation) ($\widetilde{c_i}$) is the "footprint" of the impeller in the fluid, therefore the driving force behind the momentum exchange, thus working principle of the machine. It is directly connected to the rotational frequency of the impeller (in case of geometrically periodic impellers, the blade passing frequency (BPF) is valid as well). It describes the influence of the impeller on the side channel flow. Therefore, it also includes all impeller related losses (friction, flow incidence, flow separation, etc.). In case of RFPs it is connected to the circulation mass flow, as this is the dominant mass flow regarding the interaction between impeller and side channel (compare Section 2.3).

The stochastic fluctuations (c_i') can be interpreted (in case of RFP) as "unwanted, randomly occurring but unavoidable flow phenomena" due to the turbulent flow. It also includes the measurement uncertainty of the system, as well as all fluctuations of the flow that are not directly connected to the impeller but induced from outside the system. This can be everything from a state-switching flow separation occurring at a choked valve, up to speed variation of the auxiliary pump, leading to slow pulsation of the flow.

This decomposition now enables to analyze the cause-effect relation between impeller and side channel flow in a more rigorous way by focusing on the periodic dynamic ($\widetilde{PD}$). $\widetilde{PD}$ can not be measured directly, however it is possible to calculate them from the gathered results of the $\overline{TA}$ and $\langle PA \rangle$ measurements. This was shown by Pechloff and Laschka [65] who stated, that when dividing an arbitrary flow field into a phase averaged ($\langle PA \rangle$) part and a time averaged ($\overline{TA}$) part, it "yields two distinct sets of equations, respectively, governing unsteady and steady mean flow. In both cases the existing turbulent fluctuations are exclusively composited into average correlation terms, the necessary mathematical identities for this process having been provided by Telionis [66]". In summary, it is explained how periodic dynamics can be expressed by a simple subtraction of $\overline{TA}$ from $\langle PA \rangle$, as the stochastic fluctuation terms are present in both expressions. This leads to equation (8.2):

$$\widetilde{c_i}(\theta, r, z, pa) = \langle c_i(\theta, r, z, pa) \rangle - \overline{c_i}(\theta, r, z) \tag{8.2}$$

It has to be mentioned, that in their work Pechloff and Laschka [65] used the precise physical definitions of $\overline{TA}$ and $\langle PA \rangle$ regarding continuity by using integral expressions. As the present work is experimental, only discretize sampled values are at hand. Therefore, common finite equations for $\overline{TA}$ and $\langle PA \rangle$ were used (equations 6.2 & 7.1). However, as both were shown to be statistical significant and even calculated from the same data pool, equation (8.2) is valid to use.

8.1 Periodic Dynamic Flow Fields $\widetilde{c_i}(\theta, r, z, t_{pa})$

Figures 8.1 & 8.2 show the resulting periodic dynamics $\widetilde{c_i}$ for all six measured OPs in the $2mm$ plane. Flow fields are still presented in the same quantifiable manner as in Chapter 6, showing velocities normalized by the mean side channel velocity c_{sc} for a distinct blade position (as the PDs are calculated from the $\langle PA \rangle$ results of Chapter 7, it is the same position).

The power of this combined approach is directly visible: The resulting in-plane, as well as out-of-plane velocity patterns seem very similar for all measured OPs along the characteristic curve. Up to $ch = 0.9$ the resulting flow fields show a periodic dynamic, directly connected to the geometry of each blade channel: Repeating radial bands of counter-directional axial velocity (from impeller to side channel on the pressure side (warm colors) and contrary for the suction side of the blade (cold colors)). They interact with each other in-plane via contrariwise circumferential streamlines to the center of the blade channel, where they merge towards the hub. Above each blade there is a flow in the opposite direction, pointing to the outer rim of the side channel. From OL to PL a circumferential shift of this pattern against the direction of rotation is observable. Starting at $ch = 0.9$, an additional shift is visible, strongly influenced by the current OP: For OP6 in strong PL, the pattern seems nearly shifted by half a side channel width. In this small part of the side channel, another phenomenon can be observed: A pair of counter-rotating axial vortices for $ch > 0.9$ become visible (best observable in OP4). (Recall that $ch = 0.9$ is also the position of the zero crossing of the axial component for the $\overline{TA}$ flow fields). To compare quantitatively, extracted velocity profiles are presented in the same manner as before.

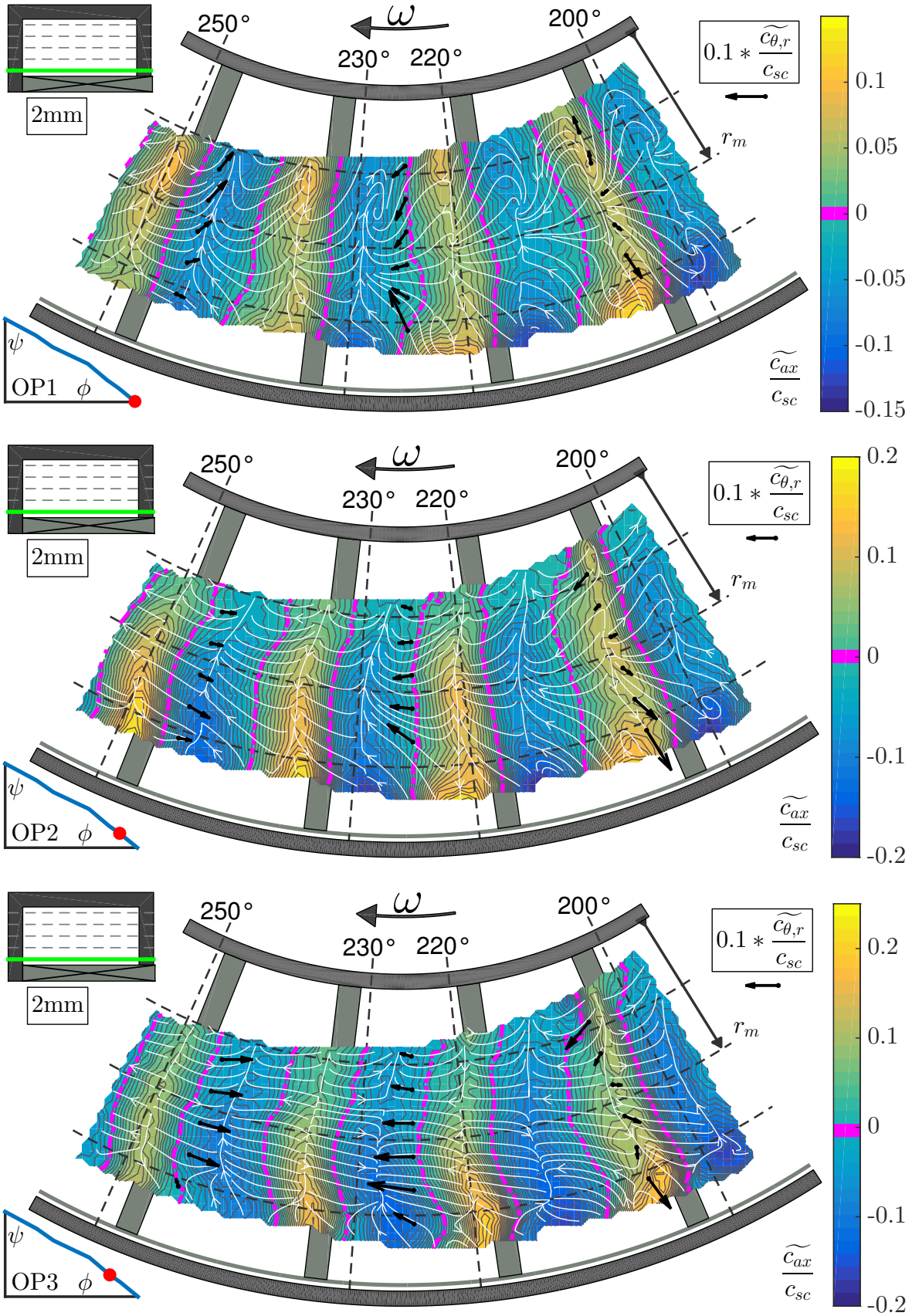

Figure 8.1: Periodic Dynamic Flow Fields $\widetilde{c_i}(\theta, r, 2mm, 4)$: OP1 to OP3.

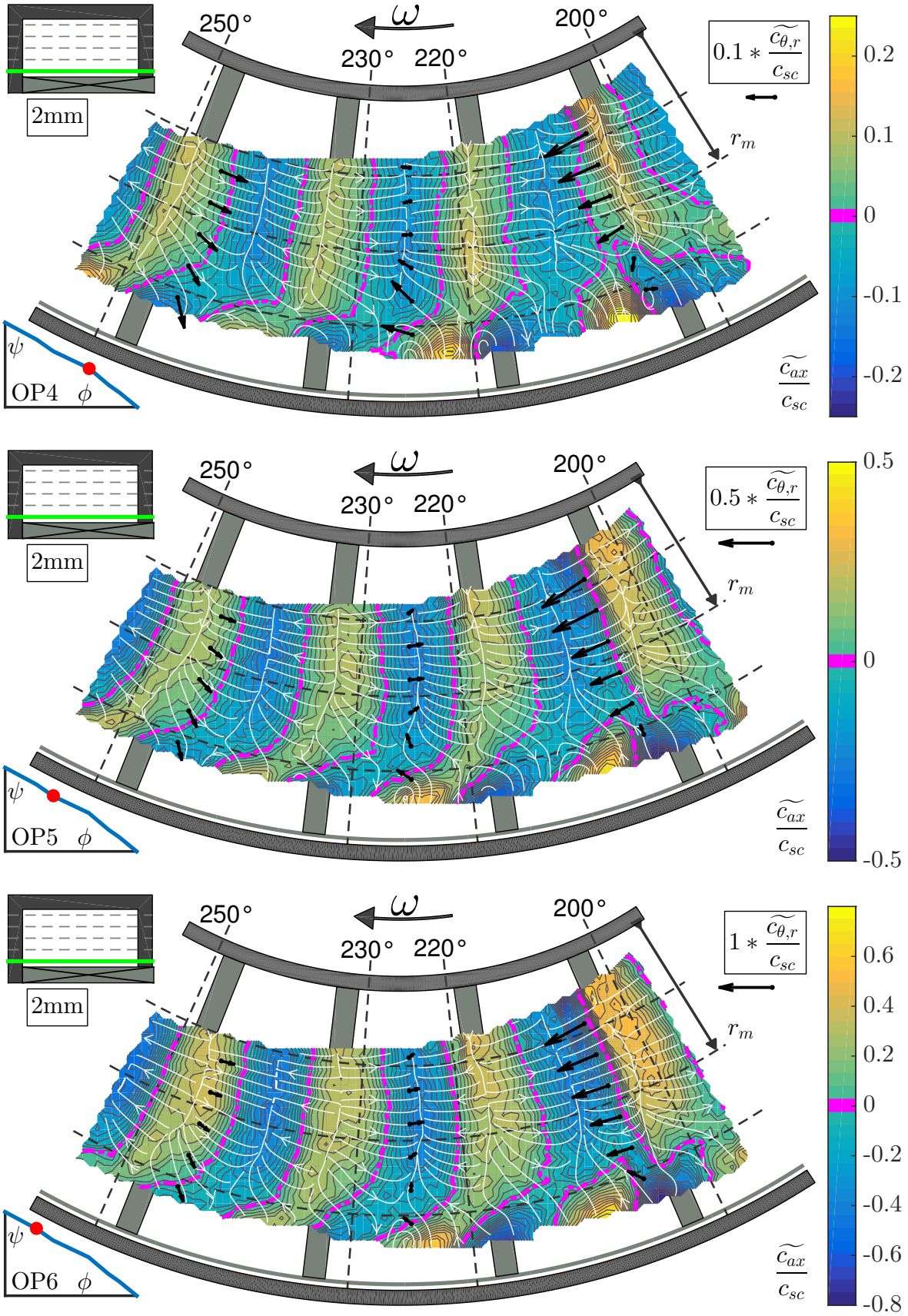

Figure 8.2: Periodic Dynamic Flow Fields $\widetilde{c_i}(\theta, r, 2mm, 4)$: OP4 to OP6.

8.2 Radial Profiles

Figure 8.3 shows the radial development of the $\widetilde{PD}$ of different velocity components at pressure (PS) and suction side (SS) of the same blade channel.

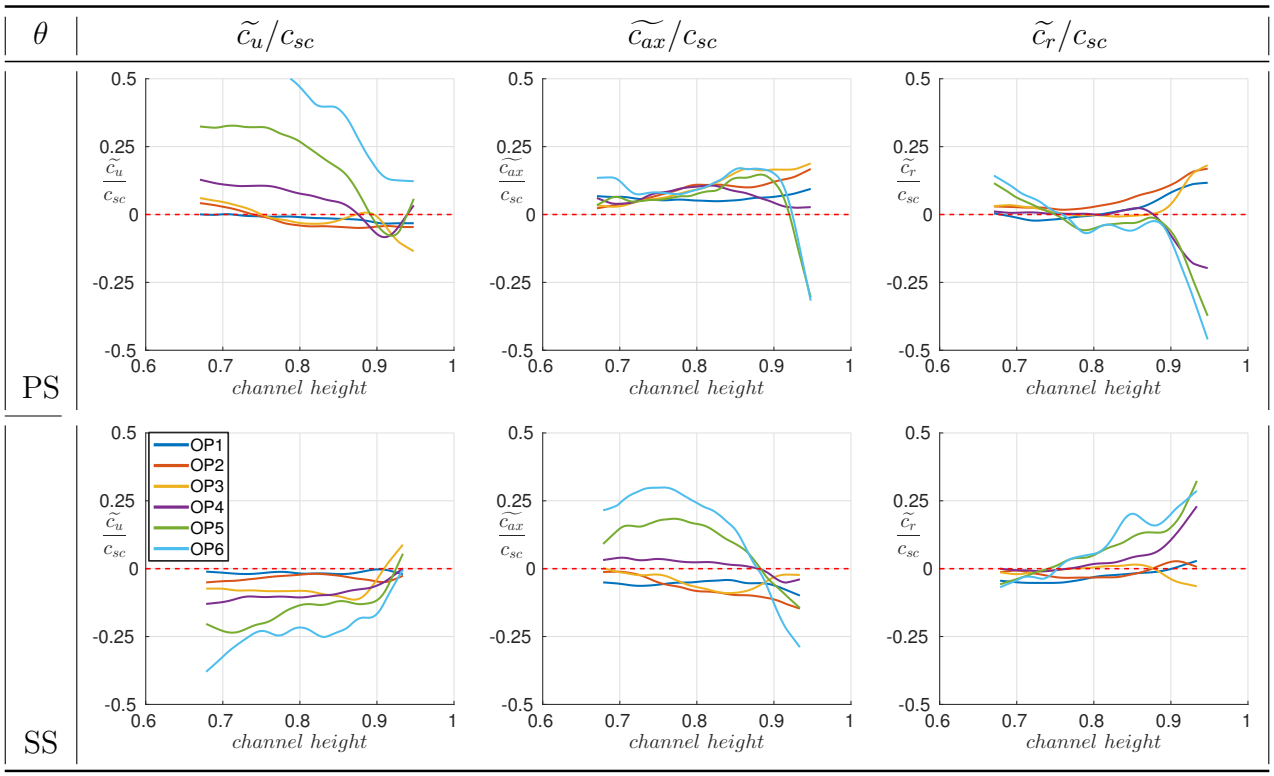

Figure 8.3: Radial profiles for the periodic dynamics of all three velocity components at the pressure (PS) and suction side (SS) of the same blade channel.

Quantifiable differences become visible, with all velocity components having the same order of magnitude. While the magnitude of $\widetilde{c_u}$ is only 10% of the $\overline{TA}$ one ($\overline{c_u}$),both other components $\widetilde{c_{ax}}$ & $\widetilde{c_r}$ are within the same range as their corresponding $\overline{TA}$ ones. $\widetilde{c_u}$ seems to be mirrored at the zero-crossing: while being positively monotonic sorted according to the OPs on the pressure side, it is opposite on the suction side. For the other components, no clear OP depending tendencies are visible for a wide spread of the side channel. Remarkable is again the $\overline{TA}$ zero-crossing point at around $ch = 0.9$: all three components start to change their behavior, especially in part load steep gradients are visible. In addition this is also the point where most components switch their signs.
Conclusively, it can be stated that, regarding the radial extend of the $\widetilde{PD}$, the outer part is of importance. Steep gradients, as well as sign switches imply a complex flow field in all three directions. This was shown by the in-plane flow fields as well (recall the counter-rotating axial vortices). However, as the impellers main working direction is along θ, the circumferential development is of greater interest.

8.3 Circumferential Velocity Profiles

As described at the beginning of this Chapter, the periodic dynamics can be interpreted as the "footprint" of the impeller in the flow field. Figure 8.4 is introduced to show its circumferential development. As the characteristic radius $ch = 0.8$ was chosen this time, representing a wide

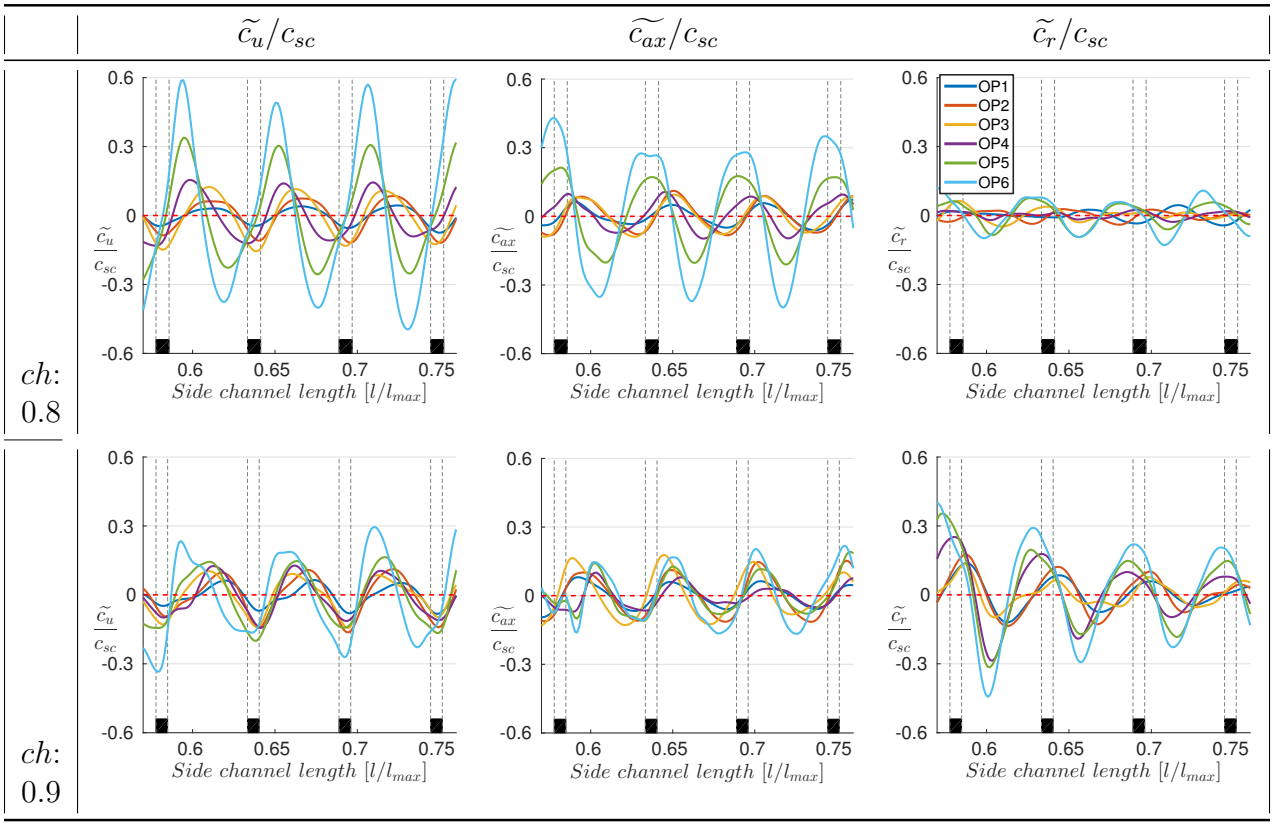

Figure 8.4: Development of the circumferential periodic dynamics along the side channel for different radii.

part of the flow field. $ch = 0.9$ is given as well, representing the already identified area of strong interplay of all components. With the influence of the average flow being subtracted, periodic velocity oscillation due to the interaction with the impeller now become clearly visible. As already shown by the $\widetilde{PD}$ in-plane flow fields, there are pattern-like structure visible, which now become obviously connected to the underlying impeller. In the stable region around $ch = 0.8$ the circumferential development is remarkable: Distinct oscillations around zero for all three components and all OPs show the periodic behavior clearly. Position of the maxima for each OP and all components are fixed in relation to the blades, therefore repetitive for each blade channel. Not only in position, but in magnitude as well. The connection between the circumferential shift and the according OP is monotonic: from OL to PL the local maxima are shifted against the direction of rotation. A direct monotonic connection between the amplitude of the oscillation and the current OP can be made as well: The higher the generated head, the higher the amplitude of the periodic dynamic. It is also remarkable to see that all three components seem to be directly connected to each other: for every OP, $\widetilde{c_u}$ and $\widetilde{c_{ax}}$ are shifted by nearly 90° (regarding the oscillation period, not θ). In case of $\widetilde{c_u}$ and $\widetilde{c_r}$ it is nearly 180° thus between $\widetilde{c_{ax}}$ and $\widetilde{c_r}$ being 90° again. Taking a closer look at $ch = 0.9$ the same dependencies can be observed: 90° for $\widetilde{c_u}$

and $\widetilde{c_{ax}}$, as well as $\widetilde{c_{ax}}$ and $\widetilde{c_r}$ and 180° for $\widetilde{c_u}$ and $\widetilde{c_r}$. Remarkably, $\widetilde{c_r}$ at $ch = 0.9$ is the only component with a visible decrease in magnitude.

8.4 Plane-to-plane comparison

As the last step in presenting the flow field development through the side channel, the axial development is shown. With Figure 8.5 the remaining planes are introduced. Similar patterns to the one described before can be seen in the higher planes as well. Additionally, due to the extended measurement regime closer to the outer rims, complicated interacting periodic vortex structures can be observed. These counter-rotating pairs of vortices now also show up near the hub for the middle planes ($10/14mm$), but are not that obvious near the ceiling of the side channel anymore ($18mm$). However, the in-plane flow structure now becomes similar to the $2mm$ one again. With increasing distance to the impeller, its influence decreases, visible by the increasing noise for higher planes. To be able to quantify this, Figure 8.6 is introduced.

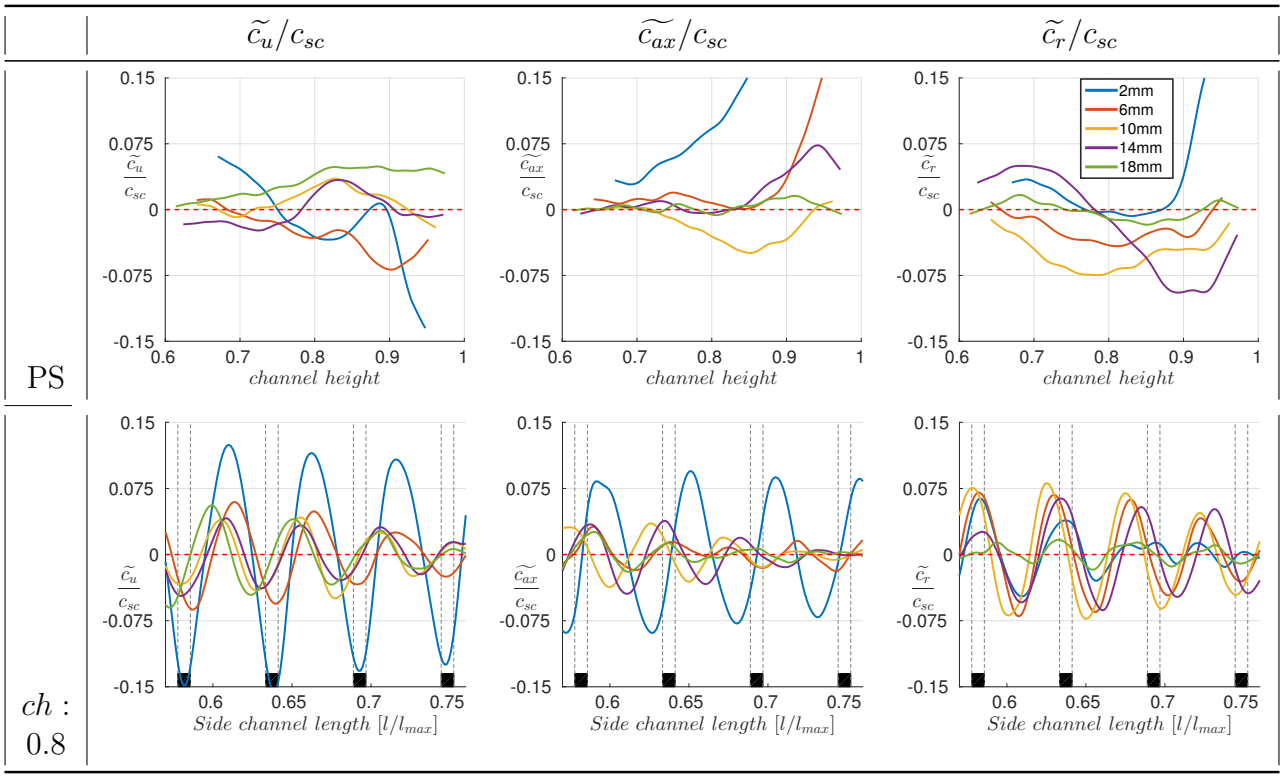

Figure 8.6: Velocity profiles for the pressure side (PS, $\theta = 220$), as well as $ch = 0.8$.

Regarding the radial development, flow structures between planes differ a lot and are obviously noisy. Besides being all in the same order of magnitude, interpretation is difficult. This is different for the circumferential case at $ch = 0.8$: The impeller-induced oscillation are visible for all planes. The $2mm$ plane amplitude is nearly as double as the rest in case of $\widetilde{c_u}$ and $\widetilde{c_{ax}}$ but within the same range for $\widetilde{c_r}$, even with a strong decrease in amplitude compared to the more distant planes.

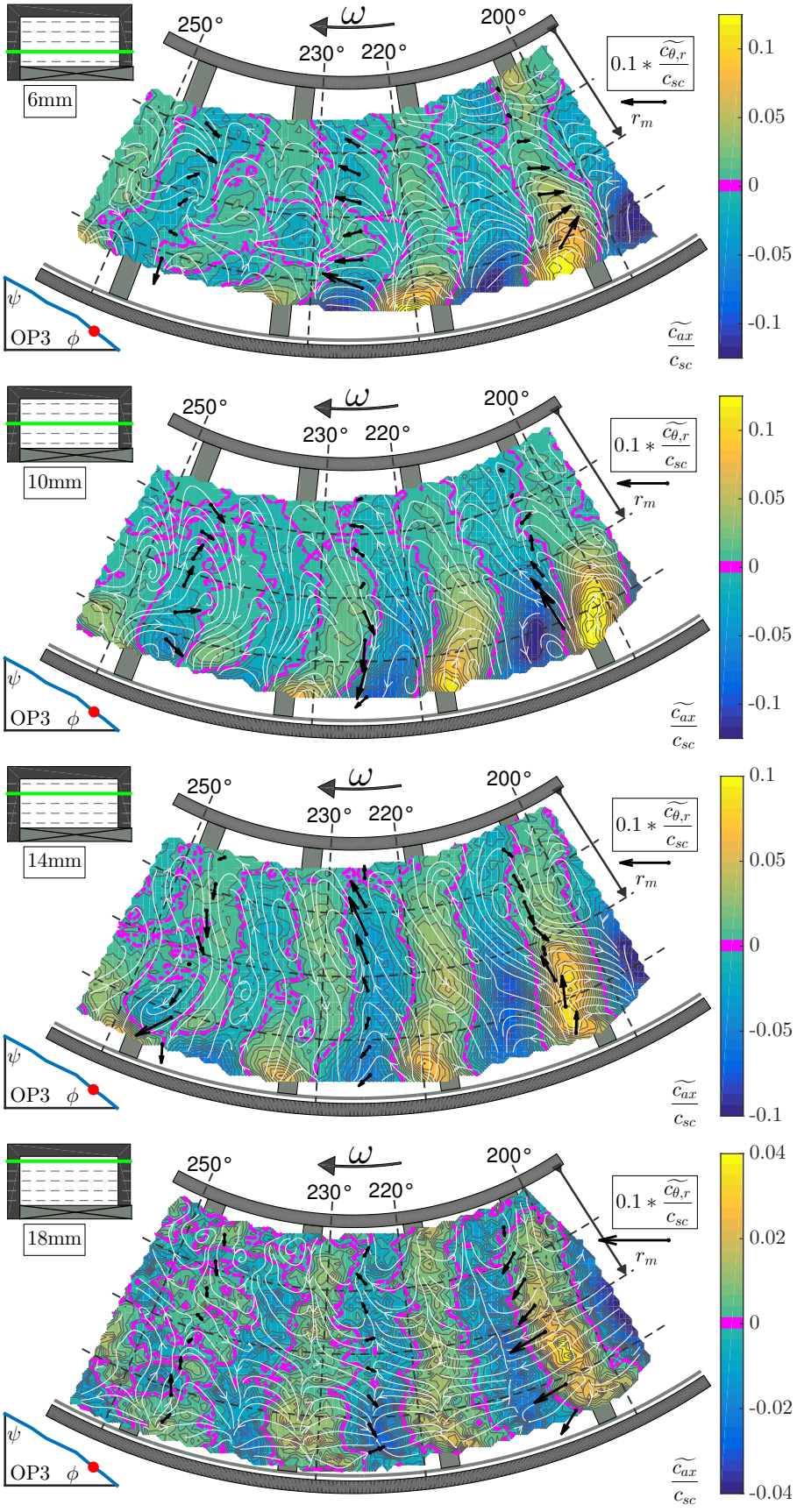

Figure 8.5: Periodic Dynamic Flow Fields $\widetilde{c}_i(\theta, r, z, 4)$ for OP3 with $z = 6 - 18mm$.

8.5 Frozen Periodic Dynamic Flow Field Interpretation

As the flow field analyzes in general showed plausible results, it is now possible to combine the $\widetilde{PD}$ results all together. Having subtracted the all dominating mean flow and being able to focus on a distinct phase angle position, the final result in form of the $\widetilde{PD}$ results can be interpreted as a "frozen" dynamic flow field around the impeller. It is best described as a snap-shot of the characteristic dynamic within the side channel that is induced by the impeller. The term "frozen" refers to the circumstance that the flow rotates synchronously with the impeller (therefore also the term (constant) "footprint"). This frozen periodic dynamic is shown exemplary for OP3 with Figure 8.7.

Radial cuts along the pressure (PS), as well as the suction side (SS) of the middle blade channel around $\theta = 225°(cl = 0.67)$ are shown in the upper part. Circumferential cuts along two distinct radial positions are given underneath: $ch = 0.8$ representing the rather "stable" OP independent part, while $ch = 0.9$ represents the radial position with clearer differences between OPs (keep in mind, that however only OP3 is shown). The individual planes of each measurement are are dashed green lines, while common profiles are indicted by blue dashed lines.

Now is is possible to interpret the cause-effect relation between the impeller and the flow through the side channel by describing the flow around one blade. On the pressure side of the blade, the fluid is being pushed in rotation direction and has to evade upwards in axial direction. When entering the side channel it parts in circumferential direction: One part flows via the side channel to the suction side of the previous blade. This can be assumed to be a stable vortex within two blades, with its center somewhere on the interface between impeller and side channel. The other part tips over the blade. With now being on the suction side of the blade, it interacts with fluid influenced by the following blade and merges downwards to the impeller and in direction of the hub. Along the axial extend, the flow structure is more complex and beyond the scope of observation abstraction. It has again to be mentioned that the axial recombination is very fragile to the true phase angle of each axial measurement plane. Despite the fact, that the reconstruction looks physically plausible, in theory, planes $10, 14, 18mm$ *could* have a circumferential shift of up to 5° (compare the measurement system coupling section in Chapter 4.2). However, due to the smooth axial development at $ch = 0.8$, it can be assumed that the recombined flow field is valid within margins.

It is visible that the impact of the impeller (therefore the Frozen Periodic Dynamic) is a very complex 3-dimensional structure beyond the point of a simple descriptive explanation. However, an obviously repeating, not only impeller, but blade related system of vortices in all three dimensions with a distinct pattern can be seen. Differences along θ are weak, but visible.

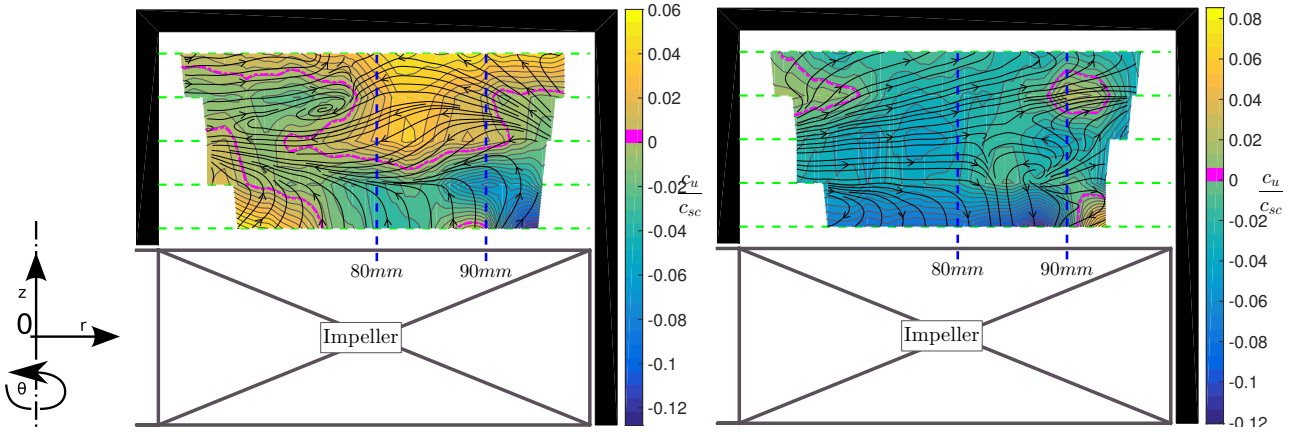

(a) Pressure side (b) Suction side

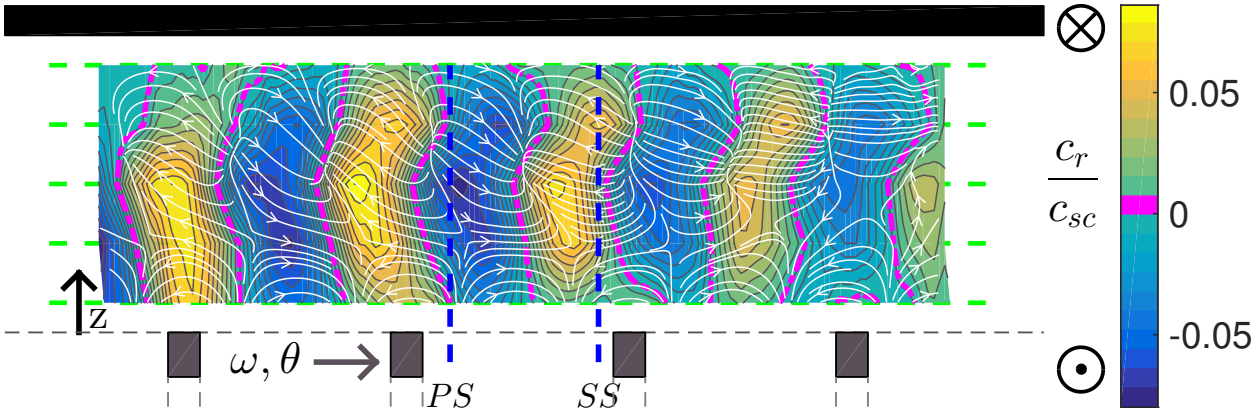

(c) $ch = 0.8$

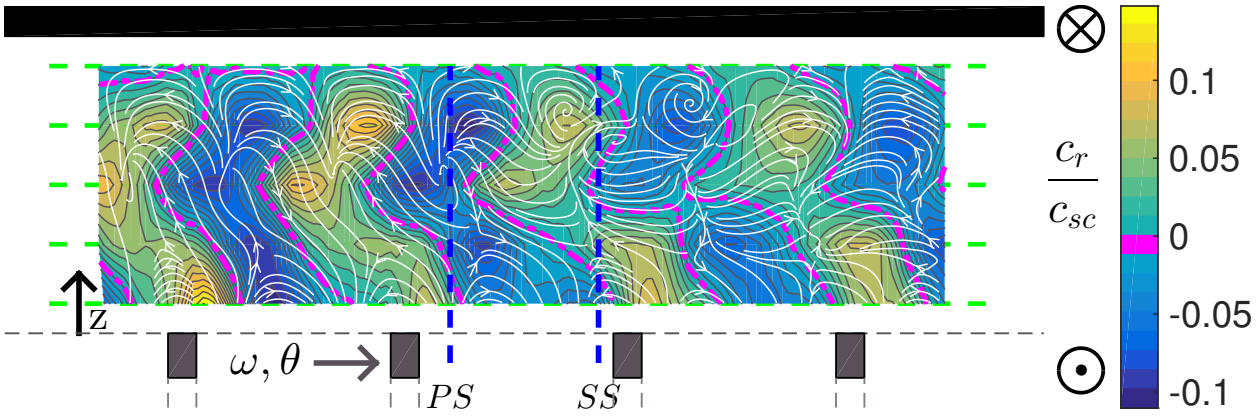

(d) $ch = 0.9$

Figure 8.7: Frozen flow distribution for the periodic dynamic: Radial cuts along pressure and suction side of the middle blade channel. Circumferential cuts along $ch = 0.8, 0.9$. Common Profiles indicated by dashed blue lines. Measurement planes indicated in dashed green.

Chapter 9

Concluding Remarks

The present work comprises an experimental investigation into the flow phenomena of a regenerative flow pump. A comprehensive documentation of the executed measurement campaign is given. A specific purpose-built regenerative flow pump has been designed and integrated into a common pump test rig. Modern methods of time resolved two-dimensional, three-component flow field measurement have been applied to provide a database for comparison with experiments as well as simulations on the same topic. Additional integral value measurements support the flow field information, allowing comparison to a wider field of present as well as future studies. As the flow field within the side channel is discussed in all three dimensions for a representative region of interest and various points along the characteristic curve of the machine, the former demand of a comprehensive insight into the flow mechanism behind the interaction between impeller and side channel is fulfilled. Theoretical fundamentals are presented in the necessary depth to understand the working principle of this rather unconventional type of fluid machinery. The experimental setup as well as the utilized methods are described in detail to be able to estimate comparability with similar work. An extensive validation has been carried out to ensure significance and reproducibility, thus robustness and reliability of the obtained data. Results are presented in visually convenient way to allow qualitative comprehension, as well as to enable comparison to present or future work on the same topic. In addition, quantitative comparison is possible as well, since the results are presented in terms of normalized (dimensionless) quantities. As a novel approach, the triple decomposition is proposed to serve as a more rigorous approach to uncover the impact of the impeller onto the fluid.

Frozen Periodic Dynamic

The common representation of the relative flow $\vec{w}$ (see eq.: 2.1) through a fluid machine by vectorial subtracting the local impeller speed $u(r)$ from the absolute velocity $\vec{c}$ fits its purpose well. Within or close to the blade channel this method enables to understand and interpret the flow through or influenced by the impeller. However, the common relative flow representation looses significance with increasing distance to the impeller, as more and more effects within the flow interact with each other, considerably weakening the (only one-dimensional considered) influence of the impeller. The common definition of $\vec{w}$ also enables to analytically describe the cause-effect relation between impeller (cause) and flow (effect) in case of pumps and fans (or vice versa if/in case that turbines are considered). The most common expression here is

"Euler's pump and turbine equation" for fluid machinery, where in case of blade congruent flow of the relative component $\vec{w}$, the interplay between impeller and flow can be reduced to a model, where only forces in circumferential direction of the impeller can exchange torsional momentum (cause) (therefore the common reduction to the term $g \cdot H_{tot} = \Delta\ uc_u$), while the primary flow through the machine (effect) is perpendicular to that.

In case of (but not limited to) RFP, this makes it extremely difficult to understand the cause-effect relation, as main flow direction and circumferential direction of the impeller are parallel to each other and an advanced model in form of a circulation flow is necessary to analytically create this perpendicularity of components again via a momentum balance within the side channel (compare 2.3). This is extremely convenient, as it "converts" RFPs through the "momentum theory" into the frame of reference of fluid machinery, therefore enabling the use of common approaches (such as dimensionless comparison or application of affinity laws). However, due to necessary assumptions and simplifications and the additional switching in the frame of reference, it is very difficult to understand the true impact of the impeller onto the fluid and therefore the general flow situation within the side channel. This makes it challenging to formulate the interaction between primary flow and circulation flow. However, this is essential to be able to understand the working principle completely. Only through that, advanced optimization strategies are possible.

The proposed method to use a triple decomposition to represent the relative impact of the impeller to the flow, clarifies the flow development. Although it is still extremely difficult to interpret the flow mechanism within the machine, the reduction to a "Frozen Periodic Dynamic" helps to assign distinct flow patterns (cause) to the primary flow (effect). This pattern-related point of view to understand cause-effect relations can also be taken a step further, by using more advanced mathematical operations to identify flow patterns more clearly. First promising results were already achieved by making use of a proper orthogonal decomposition (POD), which showed similar results for the same data pool ([67–70]). It has to be mentioned, that the "Frozen Periodic Dynamic" is not limited by a measurement frequency. As long as both data pools of $\overline{TA}$ and $\langle PA \rangle$ are independently statistical significant, the resulting "Frozen Periodic Dynamic" ($\widetilde{PD}$) still represents the "footprint" of the impeller, therefore covering all phenomenon which occur with the characteristic frequency. This also includes i.e. all rotational frequency related losses as well. Therefore, the benefit of a this relative approach is not limited to RFPs, but can also help in understanding more common types as well, since the periodic relative impact of the impeller can be analyzed at any position, as long as the influence is measurable.

Bibliography

[1] John Peter Oleson. *Greek and Roman mechanical water-lifting devices: the history of a technology*. Vol. 16. Springer Science & Business Media, 1984.

[2] THE EUROPEAN PARLIAMENT and THE COUNCIL OF THE EUROPEAN UNION. *DIRECTIVE 2009/125/EC OF THE EUROPEAN PARLIAMENT AND OF THE COUNCIL*. THE EUROPEAN PARLIAMENT and THE COUNCIL OF THE EUROPEAN UNION, 2009.

[3] E Crewdson. "Water-ring self-priming pumps". In: *Proceedings of the Institution of Mechanical Engineers* 170.1 (1956), pp. 407–425.

[4] Francis Quail, Thomas Scanlon, and Matthew Stickland. "Design optimisation of a regenerative pump using numerical and experimental techniques". In: *International Journal of Numerical Methods for Heat & Fluid Flow* 21.1 (2011), pp. 95–111.

[5] T Meakhail and S O Park. "An improved theory for regenerative pump performance". In: *Proceedings of the Institution of Mechanical Engineers, Part A: Journal of Power and Energy* 219.3 (Jan. 2005), pp. 213–222. ISSN: 2041-2967.

[6] Abraham Engeda. "Flow Analysis and Design Suggestions for Regenerative Flow Pumps (Keynote)". In: *ASME/JSME 2003 4th Joint Fluids Summer Engineering Conference*. American Society of Mechanical Engineers. 2003, pp. 1847–1857.

[7] WA Wilson, MA Santalo, and JA Oelrich. "A theory of the fluid-dynamic mechanism of regenerative pumps". In: *Trans. ASME* 77.8 (1955), p. 1303.

[8] Marco Badami. *Theoretical and experimental analysis of traditional and new periphery pumps*. Tech. rep. SAE Technical Paper, 1997.

[9] JW Song, Abraham Engeda, and MK Chung. "A modified theory for the flow mechanism in a regenerative flow pump". In: *Proceedings of the Institution of Mechanical Engineers, Part A: Journal of Power and Energy* 217.3 (2003), pp. 311–321.

[10] Mukarrum Raheel and Abraham Engeda. "Current status, design and performance trends for the regenerative flow compressors and pumps". In: *ASME 2002 International Mechanical Engineering Congress and Exposition*. American Society of Mechanical Engineers. 2002, pp. 99–110.

[11] Martin Böhle and Thorsten Müller. "Evaluation of the Flow Inside a Side Channel Pump by the Application of an Analytical Model and CFD". In: *ASME 2009 Fluids Engineering Division Summer Meeting*. American Society of Mechanical Engineers. 2009, pp. 11–18.

[12] JW Hollenberg and JH Potter. "An investigation of regenerative blowers and pumps". In: *Journal of Manufacturing Science and Engineering* 101.2 (1979), pp. 147–152.

[13] Francis Quail, TJ Scanlon, and MT Stickland. "Study of a regenerative pump using numerical and experimental techniques". In: *8th European Turbomachinery conference*. 2009.

[14] S. Muller. "Consider regenerative pumps for low-flow/low-NPSH applications". In: *Hydrocarbon Processing* (2004), pp. 55–57.

[15] G. Grabow. "Übersicht über die Theorien zur Klärung der Strömung in Seitenkanalmaschinen". In: *Verlag und Bildarchiv* (1992).

[16] C. Ritter. "About Self-Priming Centrifugal Pumps and Experiments on a New Pump of This Type". PhD thesis. Saxon Technical University of Dresden, 1930.

[17] Walter Schmiedchen. "Studies on Centrifugal Pumps With Side Ring Channel". PhD thesis. Saxon Technical University of Dresden, 1932.

[18] Heinrich Engels. *Untersuchungen an Ringpumpen (Seitenkanalpumpen)*. na, 1940.

[19] HW Iversen. "Performance of the periphery pump". In: *Trans. ASME* 53 (1955), pp. 19–28.

[20] F. Weinig. *Analysis of traction pumps*. Tech. rep. DTIC Document, 1955.

[21] C Pfleiderer. *Centrifugal Pump for Liquids and Gases*. Springer, Berlin, Germany, 1949.

[22] Yasutoshi Senoo. "Theoretical research on friction pump". In: *Institute of Fluid Engineering* 5.1 (1948), pp. 23–48.

[23] Yasutoshi Senoo. "Researches on peripheral pumps". In: *Rep. Res., Inst. Appl. Mech* 3.10 (1954), p. 53.

[24] J Bartels. "Performance of a peripheral pump". In: *Polytechnic Institute of Brooklyn* (1947).

[25] L Lazo and T Hopkins. "Theoretical and experimental analysis of a regenerative turbine pump". In: *Massachusetts Institute of Technology* (1953).

[26] GF Lutz. "Experimental Investigation of the pressure distribution in a regenerative turbine pump". In: *Massachusetts Institute of Technology* (1953).

[27] David P DeWitt. "Rational design and development of the regenerative pump". PhD thesis. Massachusetts Institute of Technology, 1957.

[28] Steven C Mason. "Influence of internal geometry upon regenerative pump performance". PhD thesis. Massachusetts Institute of Technology, 1957.

[29] H. Pfaff. "Comparative Investigations of Regenerative Pumps With and Without Diffusor". PhD thesis. Technical University of Hannover, 1961.

[30] G Grabow. "Influence of the number of vanes and vane angle on the suction behaviour of regenerative pumps". In: *Second Conference on Flow Machines*. 1966, pp. 147–166.

[31] Yasutoshi Senoo. "A comparison of regenerative-pump theories supported by new performance data". In: *Trans. ASME* 78 (1956), pp. 1091–1102.

[32] IS Yoo, MR Park, and MK Chung. "Improved momentum exchange theory for incompressible regenerative turbomachines". In: *Proceedings of the Institution of Mechanical Engineers, Part A: Journal of Power and Energy* 219.7 (2005), pp. 567–581.

[33] Shin-Hyoung Kang, Hyung-Soo Lim, and Su-Hyun Ryu. "Performance Evaluation of a Regenerative Pump of Small Size". In: *ASME 2004 Heat Transfer/Fluids Engineering Summer Conference*. American Society of Mechanical Engineers. 2004, pp. 1171–1178.

[34] Mukarrum Raheel and Abraham Engeda. "Systematic design approach for radial blade regenerative turbomachines". In: *Journal of propulsion and power* 21.5 (2005), pp. 884–892.

[35] Mukarrum Raheel and Abraham Engeda. "Performance characteristics of regenerative flow compressors for natural gas compression application". In: *Journal of energy resources technology* 127.1 (2005), pp. 7–14.

[36] Younes Elkacimi and Norbert Müller. "Regenerative Flow Pumps and Compressors (RFP/RFC) Applications for Water as Refrigerant". In: *ASME 2006 International Mechanical Engineering Congress and Exposition*. American Society of Mechanical Engineers. 2006, pp. 101–109.

[37] Francis J Quail, Matthew Stickland, and Armin Baumgartner. "A one-dimensional numerical model for the momentum exchange in regenerative pumps". In: *Journal of Engineering for Gas Turbines and Power* 133.9 (2011), p. 093001.

[38] Francis J Quail, Thomas Scanlon, and Armin Baumgartner. "Design study of a regenerative pump using one-dimensional and three-dimensional numerical techniques". In: *European Journal of Mechanics-B/Fluids* 31 (2012), pp. 181–187.

[39] Won Chul Choi et al. "Experimental study on the effect of blade angle on regenerative pump performance". In: *Proceedings of the Institution of Mechanical Engineers, Part A: Journal of Power and Energy* 227.5 (2013), pp. 585–592.

[40] Annika Fleder and Martin Böhle. "A Systematical Study of the Influence of Blade Length, Blade Width, and Side Channel Height on the Performance of a Side Channel Pump". In: *Journal of Fluids Engineering* 137.12 (2015), p. 121102.

[41] D. Surek. "Auslegung und Projektierung von Seitenkanal-und Peripheralpumpen". In: *Forsch Ing-Wes* 63.7-8 (Aug. 1997), pp. 235–253. ISSN: 1434-0860.

[42] G. Grabow. "Untersuchung an einer Lybyrinthpumpe". In: *Maschinenbautechnik 13, Heft 1* (1964).

[43] G. Grabow. "Einfluss des Schaufelwinkels auf die Druckzahlsteigerung bei Seitenkanalpumpen". In: *Vorträge zur 3. Konferenz für Strömungsmaschinen, Budapest*. 1969.

[44] G. Grabow. "Peripheral-Seitenkanalgeblaese zur Foerderung von Luft und technischen Gasen". In: *Maschinenbautechnik, 19. Jg., Heft 3* (1970).

[45] G. Grabow. "Ein neuartiges Seitenkanalgeblaese". In: *Hinweise in Technische Gemeinschaft, Heft 8* (1970).

[46] G. Grabow. "Einfluß der Schaufelform auf das Kennlinienverhalten von Peripheral-Seitenkanalpumpen und hydrodynamischen Stroemungskupplungen (Foettinger- Prinzip)". In: *Maschinenbau Technik* 21.3 (1972), p. 117.

[47] G. Grabow. "Einfluss der Schaufelform auf das Kennlinienverhalten von Peripheral-Seitenkanalpumpen". In: *Pumpen- und Verdichterinformationen, Heft 1* (1972).

[48] G. Grabow. "Foerdereffekt bei Peripheral-Seitenkanalpumpe und glatter Scheibe". In: *Maschinenbautechnik, 22. Jg., Heft 5* 5.22 (1973).

[49] G. Grabow. “Optimale Schaufelzahl und -winkel fuer Peripheral-Seitenkanalpumpen und -geblaese.” In: *Energietechnik* 24.11 (1974).

[50] G. Grabow. “Vergleich zwischen Seitenkanalgeblaesen in radialer und axialer Bauart”. In: *Energietechnik* 33.3 (1983).

[51] D. Surek. “Kennlinien von Seitenkanalmaschinen im Turbinenbetrieb”. In: *Forschung im Ingenieurwesen* 61.6 (1995), pp. 157–164.

[52] D. Surek. “Geometrische Dimensionierung von Seitenkanalmaschinen”. In: *Forschung im Ingenieurwesen* 62 (1996), pp. 229–238.

[53] D. Surek, H. Galinsky, and S. Stempin. *Theoretische und experimentelle Untersuchungen der Energieübertragung in Seitenkanalmaschinen: DFG-Abschlußbericht; [Abschlußbericht zum Forschungsvorhaben der DFG, Kennwort: Seitenkanalmaschinenströmung; Geschäftszeichen: II D5-Gr. 1164/1-1/Su 163/1-2; Forschungszeitraum: 1.1.1992 bis 30.6.1996]. Hauptbd.* Fachhochschule, Fachbereich Maschinenbau, 1996.

[54] D Surek. “Turbulente Wirbelströmung und dynamische Druckschwankungen in Seitenkanalmaschinen”. In: *Forschung im Ingenieurwesen* 63.4 (1997), pp. 85–101.

[55] D Surek. “Einfluß der Schaufelgeometrie auf den Kennliniengradienten von Seitenkanalmaschinen”. In: *Forschung im Ingenieurwesen* 64.8 (1998), pp. 173–182.

[56] Dominik Surek. “Druckschwingungsverteilung im Seitenkanal von Verdichtern”. In: *VIP* 12.5 (Oct. 2000), pp. 326–332. ISSN: 1522-2454.

[57] Dominik Surek. “Massestrom am Unterbrecher von Seitenkanalverdichtern”. In: *Forschung im Ingenieurwesen* 61 (1995), pp. 42–66.

[58] D Surek. “Anwendung theoretischer Grundlagen und Ähnlichkeitskennzahlen zur Auslegung von Seitenkanal-Strömungsmaschinen”. In: *Sulzbach: Verlag und Bildarchiv WH Faragallah* (1992).

[59] Johann Friedrich Guelich. *Centrifugal Pumps*. Springer Science + Business Media, 2014.

[60] Markus Raffel et al. *Particle image velocimetry: a practical guide*. Springer, 2013.

[61] LB Fore et al. “Nonlinear temporal filtering of time-resolved digital particle image velocimetry data”. In: *Experiments in fluids* 39.1 (2005), pp. 22–31.

[62] Christian Gerthsen. *Gerthsen Physik*. Springer-Verlag, 2013.

[63] A. K. M. F. Hussain and W. C. Reynolds. “The mechanics of an organized wave in turbulent shear flow”. In: *Journal of Fluid Mechanics* 41 (02 Apr. 1970), pp. 241–258. ISSN: 1469-7645.

[64] B Laschka. *Unsteady Flows. Fundamentals and Applications*. Tech. rep. DTIC Document, 1985.

[65] Alexander N Pechloff and Boris Laschka. “Small disturbance Navier-Stokes method: Efficient tool for predicting unsteady air loads”. In: *Journal of Aircraft* 43.1 (2006), pp. 17–29.

[66] PD Telionis. *Unsteady viscous flows, Spring Series in Computational Physics*. 1981.

[67] Philipp Mattern, Jochen Kriegseis, and Martin Gabi. “Flow Characteristics Beyond Time and Phase - A Modal Analysis of the Patterns in a Regenerative Pump”. In: *International Conference on Fan Noise, Technology and Numerical Methods*. 2015.

[68] Philipp Mattern et al. “Investigations in a Side Channel Pump using High Speed Stereo Particle Image Velocimetry”. In: *15th International Symposium on Transport Phenomena and Dynamics of Rotating Machinery, ISROMAC-15, February 24-28, 2014, Honolulu, HI, USA*. 2014.

[69] Philipp Mattern, Martin Gabi, and Jochen Kriegseis. “Pattern Identification In A Regenerative Pump A Combined PIV / POD Approach”. In: *The XXII Symposium on Measuring Techniques in Turbomachinery*. 2014.

[70] Philipp Mattern et al. “Analysis of flow phenomena within the side channel of a regenerative pump by means of HS- SPIV and POD”. In: *Proceedings der 22. GALA-Fachtagung ”Lasermethoden in der Stroemungsmesstechnik”*. 2014.

[71] W. H. Faragallah. *Seitenkanal-Strömungsmaschinen : [Seitenkanalpumpen, Vakuumpumpen, Verdichter, Turbinen]*. 1. Aufl. Sulzbach/Ts.: W. H. Faragallah, 1992.

[72] M. Gabi. “Theoretische und experimentelle Untersuchung der Strömung in Seitenkanalverdichtern”. PhD thesis. TH Karlsruhe, 1982.

Supervised related Student Projects

[73] Maximilian Elfner. “High-speed Stereo PIV Untersuchungen an einer Seitenkanalmaschine”. MA thesis. FSM/KIT, 2014.

[74] Jan Klodt. “Messgenauigkeitsanalyse des Versuchstandes einer Seitenkanalpumpe”. MA thesis. FSM/KIT, 2014.

[75] Till Noesselt. “Kopplung transienter Analogdaten mit laseroptischen Messungen”. MA thesis. FSM/KIT, 2014.

[76] Josep Palet. “Mass flow estimation around a blade of a regenerative pump using HS-SPIV data”. BA thesis. FSM/KIT, 2015.

Nomenclature

Latin letters

Upper case

Symbol	SI Unit	Description
A	m^2	Area
A_{sc}	m^2	Side channel cross section
D_{nom}	m	Nominal diameter
D_{imp}	m	Impeller diameter
H_{tot}	m	Total head
M	Nm	Torque
N	$-$	Total number of Snapshots
P_{eff}	W	Effective hydraulic power
P_{shaft}	W	shaft power
Q	$\frac{m^3}{s}$	Volume flow rate
Q_{tot}	$\frac{m^3}{s}$	Total volume flow rate
Q_{PIV}	$\frac{m^3}{s}$	Volume flow rate through the PIV side
Q_{POM}	$\frac{m^3}{s}$	Volume flow rate through the POM side
T_{amb}	$^\circ C$	Ambient Temperature
T_{PP}	$^\circ C$	Temperature of the pressure probe
U	$\frac{m}{s}$	Outer circumferential impeller velocity

Lower case

Symbol	SI Unit	Description
c	$\frac{m}{s}$	Absolute velocity
$\overline{c}$	$\frac{m}{s}$	Time averaged absolute velocity
$\langle c \rangle$	$\frac{m}{s}$	Phase averaged absolute velocity
$\widetilde{c}$	$\frac{m}{s}$	Periodic dynamic absolute velocity
c_{ax}	$\frac{m}{s}$	Axial absolute velocity component

c_r	$\frac{m}{s}$	Radial absolute velocity component
c_u	$\frac{m}{s}$	Circumferential absolute velocity component
$c_{1,u}$	$\frac{m}{s}$	Inner circumferential absolute velocity component
$c_{2,u}$	$\frac{m}{s}$	Outer circumferential absolute velocity component
c'	$\frac{m}{s}$	stochastic fluctuation absolute velocity component
$\dot{m}$	$\frac{kg}{s}$	Mass flow rate
g	$\frac{m}{s^2}$	Gravitational constant
n	$\frac{1}{s}$	Rotational speed
n	$-$	current Snapshot
p	Pa	Pressure
r	m	Local radius
rpm	$\frac{1}{min}$	Revolutions per minute
t	s	current time stamp
t_{pa}	s	phase average time stamp
u	$\frac{m}{s}$	local circumferential impeller velocity
u_{imp}	$\frac{m}{s}$	outer circumferential impeller velocity
w	$\frac{m}{s}$	Relative velocity
z	m	Local axial distance from impeller

Greek letters

Upper case

Symbol	**SI Unit**	**Description**
Δp	Pa	pressure rise
Δy_j	$-$	Absolute uncertainty
Φ	$-$	Head coefficient
Ψ	$-$	Flow coefficient

Lower case

Symbol	**SI Unit**	**Description**
η	$-$	Efficiency
μ	$-$	Arithmetic mean
ρ	$\frac{kg}{m^3}$	Density
θ	$^\circ$	Angular distance from stripper
τ	Pa	Averaged shear stresses
σ	$-$	Standard deviation

ω	$\frac{1}{s}$	Angular frequency

Abbreviations and Acronyms

Abbr.	**Description**
2D-3C	2-dimensional, 3 components
3D-3C	3-dimensional, 3 components
ax	axial
BEP	Best Efficiency Point
Calib.-error	Calibration error
CFD	Computational Fluid Dynamics
circ	circulation
CIV	Common Integral Value (measurements)
ch	side channel height
cl	side channel length
DAQ	Data Acquisition
DFG	Deutsche Forschungsgemeinschaft
f.s.	full scale
FSM	Institute for Fluid Machinery
GE	Given Error
HS-SPIV	High-Speed Stereo Particle Image Velocimetry
KIT	Karlsruhe Institute of Technology
M1...6	Measurement Number
nom	nominal
NPSH	Net Positive Suction Head
OL	Overload
OP(s)	Operating Point(s)
o.r.	of reading
PA	Phase Angle
$\langle PA \rangle$	Phase Averaged
PD	Pulse Distance
$\widetilde{PD}$	Periodic Dynamics
PL	Part load
POM	Polyoxymethylen
PS	Pressure Side
PP	Pressure Probe

RFC	Regenerative Flow Compressor
RFP	Regenerative Flow Pump
RP	Rapid Prototyping
ROI	Region Of Interest
$\overline{TA}$	Time Averaged
sc	side channel
SS	Suction Side
st	static
Temp.-dep.	Temperature dependency
theo	theoretical
tot	total
TTL	Transistor-Transistor Logic
VAR	Various
WCC	Water Column Cascade
ZPF	Zero Point Fluctuation

List of Figures

2.1 Main flow mechanics in a RFP. 8

2.2 "Velocity triangles": the relation between earth fixed and impeller fixed coordinate system (according to [59]). 8

2.3 Momentum balance for a control volume along the side channel with acting forces (adapted from [11]). 9

2.4 Assumed path-lines and velocity triangles for different operating points within the unrolled side channel. 11

3.1 Exploded view of the RFP draft. 13

3.2 Sectional View of the RFP. 13

3.3 Basis and hub of the RFP. 15

3.4 Detailed assembled views of the RFP. 16

3.5 Hydraulic scheme of the test rig. 17

3.6 Position of the pressure probes in [mm]. 18

3.7 Discharge side swirl flow due to missing straightener, visualized by trapped air. . 18

3.8 PIV Setup. 20

3.9 Measurement planes and calibration. 21

3.10 Exemplary Overlay of the dewarped calibration images for the measurement series of the $10mm$ plane. 22

3.11 Connection scheme of the measurement instrumentation. 25

4.1 Characteristic curve for 24 blades at 500 rpm. Total Head and volume flow rate histograms for the OPs marked with green circles shown below. 30

4.2 Rpm evolution and phase angle distribution for M6 (PL). 31

4.3 Rpm evolution and phase angle distribution for M1 (OL). 32

4.4 Mean phase average raw data for the 2mm plane with clearly visible reflections. Calculated suction side position of the blade indicated by a red line. 33

4.5 Mean phase average raw data for OP3 for different planes. Calculated suction side position of the blade indicated by a red line. 33

5.1 Dimensionless coefficient Impeller 20 blades. 35

5.2 Dimensionless coefficient Impeller 24 blades. 36
5.3 Dimensionless coefficient Impeller 28 blades. 36
5.4 Dimensionless characteristic curves (—) of all three impellers with their corresponding uncertainties (- - -). 37

6.1 Exemplary mean velocity components in the 2mm plane for OP4 (BEP). 38
6.2 $\overline{TA}$ flow fields $\overline{c}(\theta, r, 2mm)$: OP1 to OP3. 40
6.3 $\overline{TA}$ flow fields $\overline{c}(\theta, r, 2mm)$: OP4 to OP6. 41
6.4 Position of the extracted splines 42
6.5 Radial profiles for different velocity components at different θ. 43
6.6 Circumferential flow development along the side channel for different radii. . . . 44
6.7 Fluctuation level: $\frac{\sigma_c}{\mu}$ OP1 to OP6 for $z = 2mm$. 45
6.8 Convergence Plots for OP 1&6. Colorcoding as indicated above. 46
6.9 Convergence Plots for different OPs at distinct positions indicated in Figure 6.8. 47
6.10 Mean flow fields $\overline{c_i}(\theta, r, z)$ for OP3 with $z = 6 - 18mm$. 48
6.11 Velocity profiles along $cl = 0.67$ as well as $ch = 0.9$. The common line of the profiles, as well as with Figures 6.12 & 6.13 is dashed in blue. 49
6.12 (r, z)-plane for $cl = 0.67$; Position of the measurement planes indicated as dashed green lines; The common line with Figure 6.11 & Figure 6.13 is dashed in blue. . 49
6.13 (θ, z)-plane for $ch = 0.9$; Position of the measurement planes indicated as dashed green lines; The common line with Figure 6.11 & Figure 6.12 is dashed in blue. . 50

7.1 Phase Averaged Convergence Plots for different OPs at two destinct positions (compare Figures 6.8 & 6.9). 51
7.2 Phase averaged mean flow fields $\langle c_i \rangle(\theta, r, 2mm, 4)$: OP1 to OP3. 53
7.3 Phase averaged mean flow fields $\langle c_i \rangle(\theta, r, 2mm, 4)$: OP4 to OP6. 54
7.4 Phase averaged radial profiles for different velocity components for pressure (PS) and suction side (SS) of the same blade channel at $\theta = 225°$. 55
7.5 Phase averaged circumferential flow development along the side channel for different radii (side channel length). Blade positions indicated by black rectangles. 56
7.6 Profiles for all three velocity components along $cl = 0.67$ as well as $ch = 0.9$ for different planes. The common line of the profiles, as well as with Figures 7.7 & 7.8 is dashed in blue. 57
7.7 (r, ax)-plane for $cl = 0.67$. Position of the measurement planes indicated as dashed green lines. The common line with Figure 7.6 & Figure 7.8 is dashed in blue. 58
7.8 (θ, z)-plane for $ch = 0.9$. Position of the measurement planes indicated as dashed green lines. The common line with Figure 7.6 & Figure 7.7 is dashed in blue. . . 58
7.9 Phase averaged flow fields $\langle c_i \rangle(\theta, r, z, 4)$ for OP3 with $z = 6 - 18mm$. 59

8.1 Periodic Dynamic Flow Fields $\widetilde{c}_i(\theta, r, 2mm, 4)$: OP1 to OP3. 62
8.2 Periodic Dynamic Flow Fields $\widetilde{c}_i(\theta, r, 2mm, 4)$: OP4 to OP6. 63
8.3 Radial profiles for the periodic dynamics of all three velocity components at the pressure (PS) and suction side (SS) of the same blade channel. 64
8.4 Development of the circumferential periodic dynamics along the side channel for different radii. 65
8.6 Velocity profiles for the pressure side (PS, $\theta = 220$), as well as $ch = 0.8$. 66
8.5 Periodic Dynamic Flow Fields $\widetilde{c}_i(\theta, r, z, 4)$ for OP3 with $z = 6 - 18mm$. 67
8.7 Frozen flow distribution for the periodic dynamic: Radial cuts along pressure and suction side of the middle blade channel. Circumferential cuts along $ch = 0.8, 0.9$. Common Profiles indicated by dashed blue lines. Measurement planes indicated in dashed green. 69

List of Tables

2.1 Comparison of regenerative and centrifugal pumps (adapted from [10]). 5

3.1 Geometrical dimensions. 14
3.2 General specifications. 14
3.3 PIV Setup Summary 19
3.4 Measurement and operation instrumentation. 24

4.1 Estimated measurement uncertainties. 27